DOE/ER-0046/3 JCS 3-23-81

Damage Analysis and Fundamental Studies

Quarterly Progress Report
July - Sept 1980

November 1980

U.S. Department of Energy
Assistant Secretary for Energy Technology
Office of Fusion Energy
Washington, DC 20545

NOTICE

Printed in the United States of America
Available from
National Technical Information Service
U.S. Department of Commerce
5285 Port Royal Road
Springfield, VA 22161

NTIS price codes
Printed copy: A10
Microfiche copy: A01

DOE/ER-0046/3
UC-20,20c

Damage Analysis and Fundamental Studies

Quarterly Progress Report
July - Sept 1980

November 1980

U.S. Department of Energy
Assistant Secretary for Energy Technology
Office of Fusion Energy
Washington, DC 20545

FOREWORD

This report is the eleventh in a series of Quarterly Technical Progress Reports on "*Damage Analysis and Fundamental Studies*" (DAFS) which is one element of the Fusion Reactor Materials Program, conducted in support of the Magnetic Fusion Energy Program of the U. S. Department of Energy. The first eight reports in this series were numbered DOE/ET-0065/1 through 8. Other elements of the Materials Program are:

- Alloy Development for Irradiation Performance (ADIP)
- Plasma-Materials Interaction (PMI)
- Special Purpose Materials (SPM).

The DAFS program element is a national effort composed of contributions from a number of National Laboratories and other government laboratories, universities, and industrial laboratories. It was organized by the Materials and Radiation Effects Branch, Office of Fusion Energy, DOE, and a Task Group on *Damage Analysis and Fundamental Studies* which operates under the auspices of that Branch. The purpose of this series of reports is to provide a working technical record of that effort for the use of the program participants, for the fusion energy program in general, and for the Department of Energy.

This report is organized along topical lines in parallel to a Program Plan of the same title so that activities and accomplishments may be followed readily, relative to that Program Plan. Thus, the work of a given laboratory may appear throughout the report. The Table of Contents is annotated for the convenience of the reader.

This report has been compiled and edited under the guidance of the Chairman of the Task Group on *Damage Analysis and Fundamental Studies*, D. G. Doran, Hanford Engineering Development Laboratory. His efforts and those of the supporting staff of HEDL and the many persons who made technical contributions are gratefully acknowledged. M. M. Cohen, Materials and Radiation Effects Branch, is the Department of Energy counterpart to the Task Group Chairman and has responsibility for the DAFS Program within DOE.

Klaus M. Zwilsky, Chief
Materials and Radiation
Effects Branch
Office of Fusion Energy

CONTENTS

	Page
Foreword	iii
Figures	xi
Tables	xvii

CHAPTER 1. IRRADIATION TEST FACILITIES

1. Rotating Target Neutron Source (RTNS)-II Operations (LLNL) 3

Irradiations were done for a total of seven different experimenters. The HEDL two temperature zone furnace was installed and is operational. Unscheduled outages occurred due to major component failure.

2. Fusion Materials Irradiation Test (FMIT) Facility (HEDL) 6

Neutron and gamma ray spectra data have been obtained from analysis of measurements of the transmission of FMIT-like neutrons through thick iron.

The FMIT neutron activation file has been updated and documented.

CHAPTER 2. DOSIMETRY AND DAMAGE PARAMETERS

1. Fission Reactor Dosimetry (ANL) 17

Dosimetry results are presented for the ORR-TBCO7 tritium breeding experiment. Plans are being made to characterize the Omega West Reactor (LASL). The status of all other experiments in HFIR, ORR, OWR, and EBR II is summarized.

2. High-Energy Neutron Dosimetry: RTNS-II (ANL, RIES, LLNL) 20

Preliminary results are presented for the joint characterization of RTNS-II with RIES and LLNL. An isotropic thermal flux appears to fill the target room and intermediate energy room-return neutrons are easily seen beyond 1 meter from the source.

CONTENTS (Cont'd)

Page

3. Helium Generation in Fusion Reactor Materials (RIES) 24

Characterization of the RTNS-II Neutron Field 25

A joint Rockwell International-ANL-LLNL irradiation to characterize the RTNS-11 neutron field and to measure total helium generation cross sections of several separated isotopes and pure elements was completed. The experiment is described in some detail.

Helium Production Cross Sections for the Separated Isotopes of Iron 28

Helium production cross sections have been determined for iron and three of its separated isotopes for the 14.8-MeV neutron spectrum of RTNS-I.

4. Damage Parameter for Ceramics (BNL) 34

Damage parameters for a selected group of ceramics have been calculated. The relative importance of neutron, gamma-ray, and ionization-induced damage has been estimated, and directions for future investigations have been identified. The program terminated at the end of this reporting period.

5. The Correlation of Irradiation Effects Data Using Primary Recoil Spectra (HEDL) 41

Primary recoil damage functions for production of Frenkel pairs in copper, silver, molybdenum, and tungsten were deduced from changes in resistivity after irradiation with neutron or charged particles and from computer simulation data on displacement cascade production. In general a linear function of damage energy above approximately 1 keV gives a good correlation of Frenkel pair production in copper, silver, molybdenum, and tungsten for charged particle and neutron irradiations. The damage energy constant is inversely proportional to the square root of the target mass. A logarithmic recoil energy dependence at low energies is adequate for most applications.

CONTENTS (Cont'd)

Page

6. 14-MeV Neutron Irradiation of Copper Alloys at RTNS-II (HEDL) 81

The addition of 5% Ni, Mn, or Al does not significantly alter the fraction of defects surviving a cascade, although Al affects the visibility of clusters. A large part of the hardening is produced by clusters not resolved by TEM.

CHAPTER 3 FUNDAMENTAL MECHANICAL BEHAVIOR

1. Effects of Irradiation Pulsing on the SIPA Creep Mechanism (UCSB/HEDL) 95

For the temperatures and pulsing conditions anticipated in the Engineering Test Facility it has been found that both the stress-induced preferential absorption (SIPA) and climb-glide creep mechanisms are essentially unaffected by the pulsing of the irradiation.

2. Irradiation Creep of Ni-4%Si (ANL) 102

The stress dependence of the irradiation creep rate under deuteron bombardment showed a transition from linear to stronger than linear with increasing stress. A linear dependence of creep-rate on damage rate was observed in the linear stress dependence regime. The irradiation creep of this alloy appears to be controlled by the SIPA-driven climb and by the dislocation glide enabled by the SIPA-climb at low and high stresses, respectively.

3. Room Temperature Helium Embrittlement in 316 Type Stainless Steel (U. Va.) 113

Two helium irradiated samples of type 316 stainless steel irradiated to the same fluence, but aged at a different temperature to produce dissimilar microstructures, were tensile tested at room temperature in an HVEM. Embrittlement occurred in the sample with no visible cavities, in contrast to the more ductile failure of the sample with large cavities.

CONTENTS (Cont'd)

Page

CHAPTER 4 CORRELATION METHODOLOGY

1. Effects of Minor Elements on the RIS and Swelling in Type 316 SS Alloys (ANL) 125

When Fe20Cr12Ni containing controlled additions of Si and Mo is bombarded by 3 MeV Ni ions, Ni and Si are enriched at the irradiated surface while Cr and Mo are depleted. The temperature dependence of the radiation-induced segregation (RIS) of Si is more complex than that of Cr, Ni and Mo.

2. Microstructural Analysis of Simultaneously Bombarded Ti-Modified 316 SS (W-R&D) 143

Microstructural evaluation of dual-ion bombarded titanium-modified 316 SS from the same heat of material used in previous HFIR studies has been completed. The same helium trapping mechanism operates at He:dpa ratios of 0.2:1, 12:1 and 70:1 corresponding to EBR-11, Tokamak and HFIR conditions when MC carbide particles precipitate. When the MC particles do not form, swelling can be as great as that observed in unmodified 316 SS at identical He:dpa ratios, bombardment temperatures and dpa rates.

3. Development of a Swelling Equation for 20%-CW 316 in a Fusion Device (HEDL/ORNL/U. Wisc.) 159

A set of void and bubble-swelling correlations has been developed which incorporates the limited available data from EBR-11 and HFIR irradiations. It appears that helium may not play quite as large a role in the determination of total swelling as had been previously anticipated.

CONTENTS (Cont'd)

Page

4. The Dependence of Flow Stress on Microstructure for Nickel and Niobium Irradiated with High Energy Neutrons and 16 MeV Protons (PNL) 178

The flow stress increase of T(d,n) and Be(d,n) neutron and 16 MeV proton irradiated nickel and niobium is described using a hard barrier model. A hardening coefficient was determined which is consistent with fission neutron irradiated material.

5. Tensile Properties Data on 316 SS Irradiated at RTNS-II (HEDL) 182

The onset of irradiation hardening was observed between 10^{17} and 10^{18} n/cm^2 at room temperature.

6. Development of an Irradiation Creep Correlation for 20% Cold-Worked AISI 316 In Fusion Environments (HEDL) 190

Low temperature fast breeder and thermal reactor data was used to extend the existing breeder correlation to the temperature range of the proposed Fusion Energy Device. Also added was a dependence on displacement rate.

FIGURES

Page

CHAPTER 1

2. Fusion Materials Irradiation Test (FMIT) Facility (HEDL)

FIGURE 1. Neutron Spectrum Emerging From Fe Block at 0° From 35 MeV d on Li. 10

FIGURE 2. Neutron Spectrum Emerging From Fe Block at 90° From 35 MeV d on Li. 11

FIGURE 3. Gamma Spectrum Emerging From Fe Block at 0" From 35 MeV d on Li. 12

FIGURE 4. Gamma Spectrum Emerging From Fe Block at 90° From 35 MeV d on Li. 13

CHAPTER 2

3. Helium Generation in Fusion Reactor Materials (RIES)

Characterization of the RTNS-II Neutron Field

FIGURE 1. Irradiation Geometry for RTNS-II Characterization. 26

FIGURE 2. RTNS-II Irradiation Assembly in its Experimental Configuration. 27

FIGURE 3. RTNS-II High-Flux Irradiation Capsule. 29

5. The Correlation of Irradiation Effects Data Using Primary Recoil Spectra (HEDL)

FIGURE 1. Defect Production Trend by Computer Simulation in Copper. 51

FIGURE 2. Defect Production Curves for Copper. 54

FIGURE 3. Defect Production Curves for Silver. 59

FIGURE 4. Defect Production Curves for Molybdenum. 62

FIGURE 5. Defect Production Curves for Tungsten. 65

FIGURE 6. (n,γ) Recoil Data and Defect Production Curves Versus Normalized Recoil Energy. 72

FIGURES (Cont'd)

Page

FIGURE 7. Mass Dependence of B Coefficient in K-P Function. 74

FIGURE A-1. (n,γ) Recoil Data Versus Normalized Recoil Energy. 80

6. 14 MeV Neutron Irradiation of Copper Alloys at RTNS-II (HEDL)

FIGURE 1. Microhardness and Microstructure of Copper and Copper Alloys Irradiated in RTNS-II at 25°C with 14-MeV Neutrons. 90

FIGURE 2. The Size Distribution of Visible Defect Clusters Formed in the Copper and Copper Alloys. 91

FIGURE 3. Lattice Parameter of Copper Alloys. 92

CHAPTER 3

2. Irradiation Creep of Ni 4% Si (ANL)

FIGURE 1. Comparison of the Stress Dependence of the Thermal Creep Rate for Ni-4 at. % Si and Pure Ni. 108

FIGURE 2. Irradiation Creep Curves (Irradiation-+Enhanced Strain vs. Time) of Ni-4 at. % Si at 1.3 x 10^{-6} dpa · s^{-1} for Various Stresses. 109

FIGURE 3. Stress Dependence of the Irradiation Creep (Irradiation-Enhanced Component) for Ni-4 at. % Si. 110

FIGURE 4. Irradiation Creep Rate (Irradiation-Enhanced Component) as a Function of Damage Rate (Ion Flux) for Ni-4 at. % Si at 34.5 MPa. 111

FIGURE 5. Damaae Rate Deoendence of the Irradiation Creeo (Irradiation-Enhanced Component) for Ni-4 at. % Si at 23 MPa, 34.5 MPa and 103 MPa. 112

3. Room Temperature Helium Embrittlement in 316 Type Stainless Steel (U. Va.)

FIGURE 1. TEM Micrograph of an Intergranular Crack Propagating in Helium Irradiated to a Fluence of $\sim 10^{18}$ cm^{-2} Aged for 2 Minutes at 400°C and Tested at Room Temperature. 120

FIGURE 2. HVEM Micrograph of a Transgranular Crack Propagating in Helium Irradiated to a Fluence of $\sim 10^{18}$ cm^{-2} Aged for 10 Minutes at 900°C and Tested at Room Temperature. 121

FIGURES (Cont'd)

Page

CHAPTER 4

1. Effects of Minor Elements on the RIS and Swelling in Type 316 Alloys (ANL)

FIGURE 1. Composition Depth Profiles of the Solute Elements in the Fe-20Cr-12Ni Base Alloy. 136

FIGURE 2. Composition Depth Profiles of the Solute Elements in the Fe-20Cr-12Ni-1Si Alloy. 136

FIGURE 3. Composition Depth Profiles of the Solute Elements in the Fe-20Cr-12Ni-2Si Alloy. 137

FIGURE 4. Composition Depth Profiles of the Solute Elements in the Fe-20Cr-12Ni-1Mo Alloy. 137

FIGURE 5. Composition Depth Profiles of the Solute Elements in the Fe-20Cr-12Ni-2Mo Alloy. 138

FIGURE 6. Composition Depth Profiles of the Solute Elements in the Fe-20Cr-12Ni-1Mo-1Si Alloy. 138

FIGURE 7. Composition Depth Profiles of the Solute Elements in the Fe-20Cr-12Ni-2Mo-2Si Alloy. 139

FIGURE 8. Segregation of Ni and Cr in Fe-20Cr-12Ni Alloys as a Function of Minor Solute Concentration. 140

FIGURE 9. Temperature Dependence of the RIS of Alloying Elements in Fe-20Cr-12Ni Based Alloys. 140

FIGURE 10. Temperature Dependence of Void Swelling in Various Alloys Irradiated to ∿ 6dpa with 3 MeV ^{58}Ni ions. 141

FIGURE 11. The Void Diameter in 3 MeV $^{58}Ni^{+}$ Ion Irradiated Alloys as a Function of Temperature. 141

FIGURE 12. The Void Density in 3 MeV $^{58}Ni^{+}$ Ion Irradiated Alloys as a Function of Temperature. 142

FIGURE 13. The Void Swelling Data of Figure 10 Plotted as a Function of Minor Solute Concentration in Fe-20Cr-12Ni Base Alloy. 142

FIGURES (Cont'd)

Page

2. Microstructural Analysis of Simultaneously Bombarded Ti-Modified 316 SS (W-R&D)

FIGURE 1. TEM Micrographs of MC Carbide Particles Encrusted with Helium Bubbles in Ti-Modified 316 SS After Irradiation in HFIR at 610°C to 57 dpa and 3400 appm Helium. 151

FIGURE 2. TEM Micrographs Showing Copious MC Carbide Precipitation and Bubble Nucleation on Those Carbides in Ti-Modified 316 SS Dually Bombarded at 600°C to 3 dpa and 210 appm Helium. 152

FIGURE 3. Comparison of Cavity and Dislocation Structures in Ti-Modified 316 SS Irradiated to 3 dpa at 600°C. 153

FIGURE 4. Microstructures Developed in 316 SS + Ti after Dual Bombardment at 600°C. 154

FIGURE 5. Comparison of Cavity and Dislocation Structures in Ti-Modified 316 SS Irradiated to 3 dpa at 700°C. 155

FIGURE 6. Typical Microstructures Developed in Ti-Modified 316 SS at 550°C. Note that Swelling is comparable with SA 316 SS. 156

FIGURE 7. Absence of MC Precipitation ana High Swelling at 5 dpa Suggest an Initial Chemical Inhomogeneity of the Base Material. 157

FIGURE 8. HFIR Irradiated 316 SS + Ti; Micrograph Indicates the Effects of Heterogeneous MC Carbide Formation Prior to Irradiation. 158

3. Development of a Swelling Correlation for 20% CW 316 in a Fusion Device (HEDL/ORNL/U. Wisc.)

FIGURE 1. Swelling Predictions for Two Nominally Identical Steels Irradiated in the U.S. Breeder Reactor Program. 171

FIGURE 2. Swelling *of* 20% Cold-Worked and Annealed AISI 316 (DO-Heat) Irradiated in HFIR and EBR-II. 172

FIGURE 3. Swelling of 20% Cold-Worked AISI 316 (DO-Heat) Irradiated in HFIR. 173

FIGURE 4. Comparison of Swelling Data on DO-Heat at 600°C. 174

FIGURE 5. Comparison of Swelling Data on DO-Heat at ~500°C. 175

FIGURES (Cont'd)

Page

FIGURE 6. Schematic Illustration of Expected Form of Bubble and Void Swelling Equations. 176

FIGURE 7. Compressibility Factor for High Density Helium Reported by Wolfer. 177

5. Tensile Properties Data on 316 SS Irradiated at RTNS-II (HEDL)

FIGURE 1. Specimen Holder for the HEDL-4 Experiment. 184

FIGURE 2. Yield Stress and Ultimate Tensile Strength as a Function of Fluence for 20%-CW 316 SS. 187

FIGURE 3. Yield Stress and Ultimate Tensile Strength as a Function of Fiuence for Annealed 316 SS. 188

6. Development of an Irradiation Creep Correlation for 20% Cold-Worked AISI 316 In Fusion Environments (HEDL)

FIGURE 1. Predictions of Creep Correlations for Two Heats of Steel of Essentially Identical Composition Irradiated in the EBR-II Reactor. 196

FIGURE 2. Temperature Dependence Reported by Gilbert of the Coefficient Describing the Irradiation Creep Rate. 197

FIGURE 3. Schematic Representation of Procedure Used to Mate Low Temperature and High Temperature Correlations. 197

FIGURE 4. Dependence of Irradiation Creep on Displacement Rate Observed in the Dounreay Fast Reactor by Lewthwaite and Mosedale. 198

FIGURE 5. Predictions of Creep Correlation as a Function of Displacement Level. 199

FIGURE 6. Predictions of Creep Correlations as a Function of Displacement Rate. 200

TABLES

Page

CHAPTER 2

1. Fission Reactor Dosimetry (ANL)

TABLE 1. Status of Reactor Experiments 18

2. High-Energy Neutron Dosimetry: RTNS-II (ANL, RIES, LLNL)

TABLE 1. Preliminary Fluence Measurements at RTNS-II 22

3. Helium Generation in Fusion Reactor Materials (RIES)

Helium Production Cross Section for the Separated Isotopes of Iron

TABLE 1. Materials Irradiated at RTNS-II for Helium Studies 29

TABLE 2. Fe(n,Total Helium) Cross Sections for 14.8-MeV Neutrons 30

4. Damage Parameter for Ceramics (BNL)

TABLE 1. Spectrum Averaged Damage Cross Sections for Al_2O_3 38

TABLE 2. Spectrum Averaged Damage Cross Section for Si_3N_4 39

TABLE 3. Spectrum Averaged Damage Cross Sections for $MgAl_2O_4$ 40

5. The Correlation of Irradiation Effects Data Using Primary Recoil Spectra (HEDL)

TABLE 1. Radiation Sources and References for Data Used in This Analysis 44

TABLE 2. Comparison of Neutron Data For Copper for Three Functions 56

TABLE 3. Input Data, Deviation Between Calculated and Measured Data, and Damage Response Range for Copper 57

TABLE 4. Input Data, Deviation Between Calculated and Measured Data, and Damage Response Range for Silver. 61

TABLE 5. Input Data, Deviation Between Calculated and Measured Data and Damage Response Limits for Molybdenum 63

TABLES (Cont'd)

Page

TABLE 6. Input Data, Deviation Between Calculated and Measured Data and Damage Energy for Tungsten 66

TABLE 7. Coefficients for the Three Functions 68

TABLE 8. Error Analysis for K-P Function Fit to Silver Data 70

6. 14 MeV Neutron Irradiation of Copper Alloys at RTNS-II (HEDL)

TABLE 1. Alloy Composition and Irradiation Conditions 82

TABLE 2. Microscopy Data - RTNS-II Copper Binary Series 84

TABLE 3. Room Temperature Hardness of Unirradiated Alloys 87

CHAPTER 4

2. Microstructural Analysis of Simultaneously Bombarded Ti-Modified 316 SS (W-R&D)

TABLE 1. Composition of 316 SS Used in Dual Ion Bombardment Studies 145

TABLE 2. 316 SS + Ti - Microstructural Observations 149

3. Development of a Swelling Correlation for 20% CW 316 in a Fusion Device (HEDL/ORNL/U. Wisc.)

TABLE 1. Swelling and Cavity Statistics for HFIR-Irradiated 00 316 163

TABLE 2. Comparison of Swelling Predictions and DO-Heat Data From HFIR 164

TABLE 3. New Swelling Data From EBR-II Irradiations 164

4. The Dependence of Flow Stress on Microstructure for Nickel and Niobium Irradiated with High Energy Neutrons and 16 MeV Protons (PNL)

TABLE 1. Microstructure-Yield Strength Comparison for T (d,n), Be (d,n) and 16 MeV Proton Irradiated Material 181

TABLES (Cont'd)

Page

5. Tensile Properties Data on 316 SS Irradiated at RTNS-II (HEDL)

TABLE 1. Chemical Composition of 316 SS Specimens 183

TABLE 2. Summary of the Tensile Properties of T(d,n) Irradiated 316 SS 185

CHAPTER 1

IRRADIATION TEST FACILITIES

I. PROGRAM

Title: RTNS-II Operations (WZJ-16)
Principal Investigator: C. M. Logan
Affiliation: Lawrence Livermore National Laboratory

II. OBJECTIVE

The objectives of this work are operation of OFE's RTNS-II (a 14-MeV neutron source facility), machine development, and support of the experimental program that utilizes this facility. Experimenter services include dosimetry, handling, scheduling, coordination, and reporting.

RTNS-II is dedicated to materials research for the fusion power program. Its primary use is to aid in the development of models of high-energy neutron effects. Such models are needed in interpreting and projecting to the fusion environment engineering data obtained in other neutron spectra.

III. RELEVANT DAFS PROGRAM TASK/SUBTASK

TASK II.A.2,3,4.
TASK II.B.3,4.
TASK II.C.1,2,6,11,18.

IV. SUMMARY

Irradiations were done for a total of seven different experimenters. The HEDL two temperature zone furnace was installed and is operational. Unscheduled outages occurred due to major component failure.

V. ACCOMPLISHMENTS AND STATUS

A. Irradiations - N. E. Ragaini, M. W. Guinan and C. M. Logan (LLNL)

The neutron field characterization experiment of D. Kneff et al. (RI) was completed. An irradiation was done for in-situ creep of Nb for W. Barmore (LLNL). An experiment using the HEDL two temperature zone furnace was begun for N. Panayotou (HEDL). Further irradiations of Nb, V, and Ti were done for R. Jones (PNL). In addition the following "piggy back" experiments were carried out:

1. Tritium detector development for R. Jalbert (LANSL).

2. Irradiation of optical samples for M. Summers (LLNL).

3. Irradiation of electronic components for D. Hoyniak (PPPL)

B. RTNS-II STATUS - C. M. Logan and D. W. Heikkinen (LLNL)

The HEDL two temperature zone furnace was installed and debugged. This furnace permits simultaneous irradiation of samples at temperatures of 80°C and 290°C in a vacuum. A new fiber optics control system was installed on both neutron sources. This has eliminated the frequent problems encountered with the original control system. A shielded cart for sample disassembly has been completed.

Major unscheduled outages occurred during this period due to turbo pump failure and failure of diode strings in the Haefely high voltage power supply.

VII. FUTURE WORK

During the quarter irradiations are scheduled for Barmore (LLNL), Guinan (LLNL), Panayotou (HEDL), and Jones (PNL). Further "piggy back" irradiations are scheduled for Jalbert (LANSL) and Murray (PPPL).

VIII. PUBLICATIONS

RTNS-II: Present Status, D. W. Heikkinen and C. M. Logan (UCRL 84554) to be presented at the Sixth Conference on the Application of Accelerators in Research & Industry, November 3, 4, 5, 1980, Denton, Texas.

RTNS-II: A Fusion Materials Research Tool, C. M. Logan and D. W. Heikkinen (UCRL 84897) to be presented at the 1980 World Conference, International Nuclear Target Development Society, October 12-16, 1980 Gatlinburg Tennessee.

I. PROGRAM

Title: Nuclear Data for Damage Studies and FMIT (WH025/EDK)
Principal Investigators: D.L.Johnson/F.M.Mann
Affiliation: Hanford Engineering Development Laboratory (HEDL)

II. OBJECTIVE

The objective of this work is to supply nuclear data needed for damage studies and in the design and operation of the Fusion Material Irradiation Testing (FMIT) facility.

III. RELEVANT OAFS PROGRAM PLAN TASK/SUBTASK

All tasks that are relevant to FMIT use, with emphasis upon:

SUBTASK	II.A.2.3	Flux spectra definition in FMIT
TASK	II.A.4	Gas Generation Rates
SUBTASK	II.A.5.1	Helium Accumulation Monitor Development
SUBTASK	II.B.1.2	Acquisition of Nuclear Data

IV. SUMMARY

Neutron and gama ray spectra data have been obtained from analysis of measurements of the transmission of FMIT-like neutrons through thick iron. These data will be used to confirm neutron transport calculations used for predictions of radiation heating in FMIT test cell walls but will also shed light on neutron transport calculations within an experimental test assembly.

The FMIT neutron activation file has been updated and documented.

V. ACCOMPLISHMENTS AND STATUS

A. Neutron Transport and Radiation Heating Measurements --

D.L.Johnson and F.M.Mann (HEOL), G.L.Woodruff (Univ. of Wash.), F.P.Brady, J.L.Romero, J.L.Ullmann, M.L.Johnson and C.M.Castaneda (Univ. of Calif. at Davis)

Measurements of the transmission of FMIT-like neutrons through thick iron and the radiation heating within the iron were outlined in the last OAFS quarterly report. The objective was to provide data to confirm neutron transport calculations which are used for predictions of radiation heating in the FMIT test cell walls. Furthermore, data were obtained for a situation that is nearly identical to that which will be experienced in the test assemblies within the FMIT test cell. The comparison of measurements and calculations of the same quantities will shed light primarily on the adequacy of our knowledge of (1) nuclear data for neutrons up to 50 MeV on iron and, (2) characteristics of the bare neutron source. The largest uncertainties might be expected in the nuclear data which have been extended far beyond the 20 MeV limit in ENDF/B evaluations and may have significant errors at lower energies.

The neutrons were produced by a beam of 35 MeV deuterons (from the cyclotron at the University of California at Davis) which was stopped in a solid lithium target that was $\sim$ 2.5 cm in diameter by 2 cm thick. This target was placed close to the center of a nearly cubical block of solid iron which was about 60 cm (2 feet) on each side. Neutrons from the source had to penetrate at least 30 cm (1 foot) of iron in any direction in order to escape the iron block.

Measurements of the neutron spectra were made with detectors placed 10 cm (4 inches) outside the block at 0° and 90° with respect to the beam direction. Proton recoil proportional counters were used to measure the portion of the spectrum from about 10 KeV to about 1.5 MeV where most of the transmitted neutrons are found. An NE213 liquid scintillator was used to measure the spectrum from about 1 MeV

up to the maximum that might be observable (about 50 MeV).

Preliminary results of analysis of the low energy portion of neutron spectral measurements (from proton recoil proportional counters) were shown in the last quarterly report, however, only the shapes were known. Since that time, analysis of the high energy portion (from the NE213 detector) has been completed. The two parts of each spectrum were then combined by normalizing the low energy part to the overlapping high energy part at a neutron energy of 1.2 MeV. Figures 1 and 2 show the results of these measurements for 0" and 90° respectively.

The shapes of the two neutron spectra are quite similar below about 6 MeV, with most of the leakage neutrons below about 0.6 MeV. The structure at low energies is similar to that seen in previous measurements that were made with different bare source spectra. Between about 0.6 and 6 MeV the spectra drop by three orders of magnitude with a dependence of approximately $1/E^3$. Above 6 MeV there are differences in the two spectra which are suggestive of the bare source spectrum in each direction that has been attenuated by the iron. Reliable spectra were obtained only up to about 20 MeV although higher energies are possible (up to 49.8 MeV at 0° and 36.5 MeV at 90"). However very few neutrons are expected above 20 MeV.

Gamma ray events can be distinguished from neutron events in the NE213 detector via pulse shape discrimination. Therefore gamma pulse height spectra were collected simultaneously with each NE213 neutron spectral measurement. It was possible to unfold those data also and Figures 3 and 4 show the gamma spectrum obtained at 0" and 90° respectively, for gamma rays above 0.9 MeV. These spectra show characteristic gamma ray lines at low energy that correspond to inelastic neutron scattering from ^{56}Fe. The higher energy gamma rays are due to radiative capture of low energy neutrons in iron and some gamma rays that follow other neutron induced reactions.

Both the neutron and gamma spectral results will be directly compared to coupled neutron-gamma transport calculations.

B. FMIT Neutron Activation Library --
F.M.Mann (HEOL)

The NEUACT computer code system which is used to predict reaction rates, decay rates, and dose rates in the FMIT facility has been modified to output group gamma spectra. The system has been modified to use the very large data libraries now available in the system. The cross section library has been updated to include 88 target isotopes, while the decay library has 424 isotopes. Documentation on the code system and on the FMIT activation library, on which the NEUACT cross sections are based, has been completed.

VI. REFERENCES

None

VII. FUTURE WORK

Analysis of deuteron activation measurements, described in previous DAFS quarterly reports, will be resumed.

VIII. PUBLICATIONS

D.W.Kneff, H. Farrar IV, F.M.Mann, and R.E.Schenter, "Experimental and Theoretical Determination of Helium Production in Copper and Aluminum by 14.8 MeV Neutrons." Nucl. Tech. 49 (1980) 498-503.

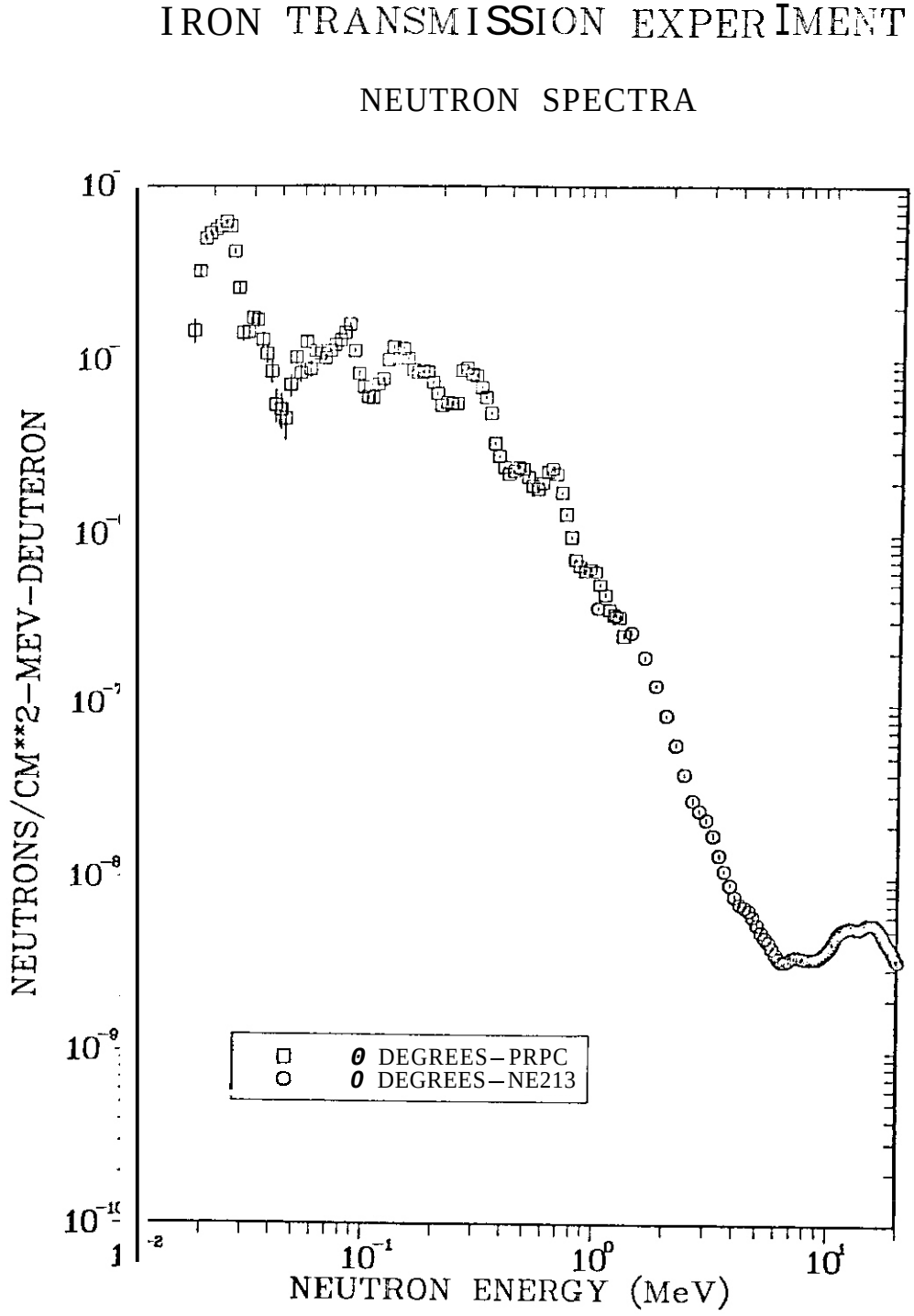

FIGURE 1. **Neutron Spectrum Emerging From Fe Block at 0° From 35** MeV **d on** Li.

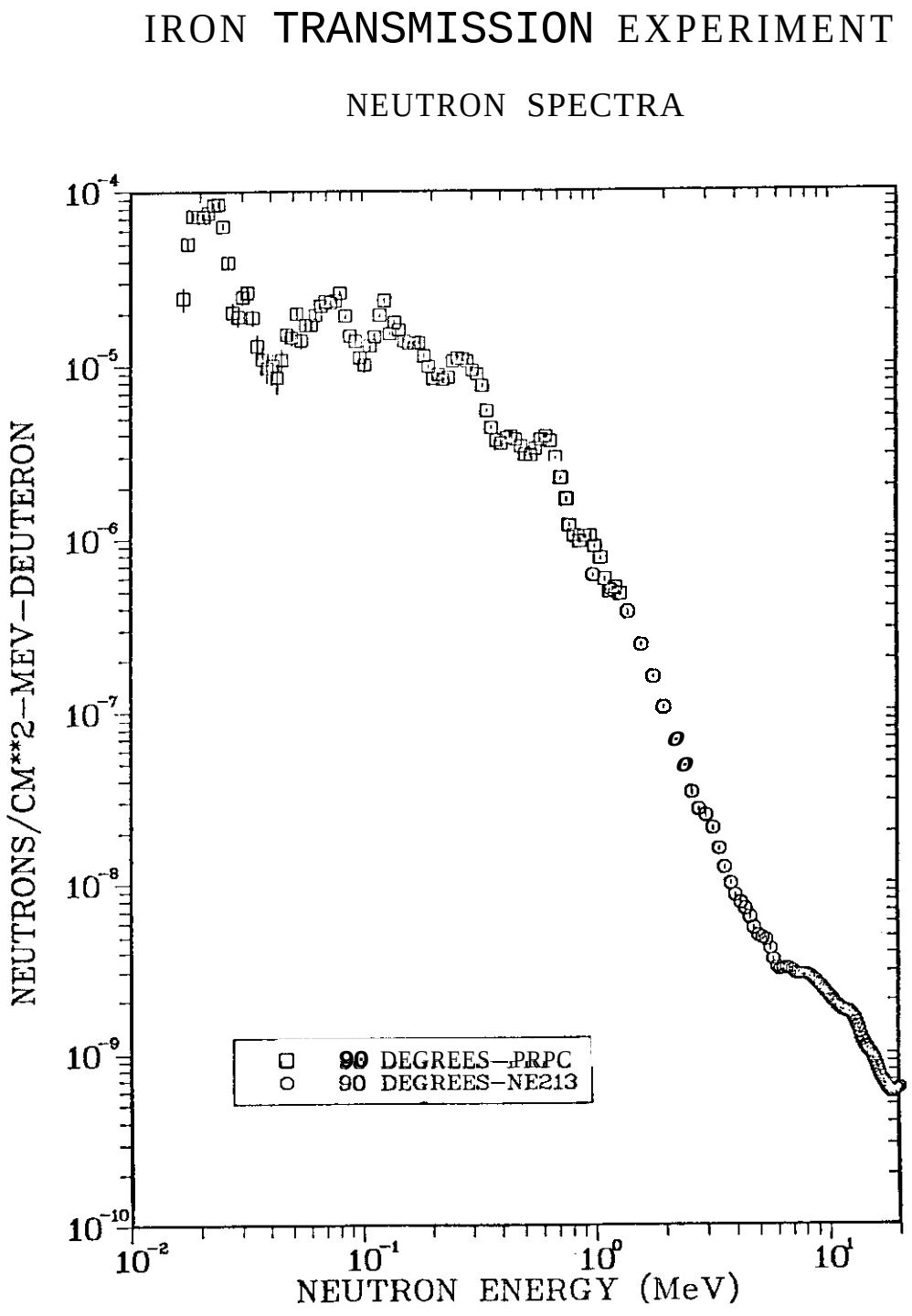

FIGURE 2. Neutron Spectrum Emerging From Fe Block at 90° From 35 MeV d on Li.

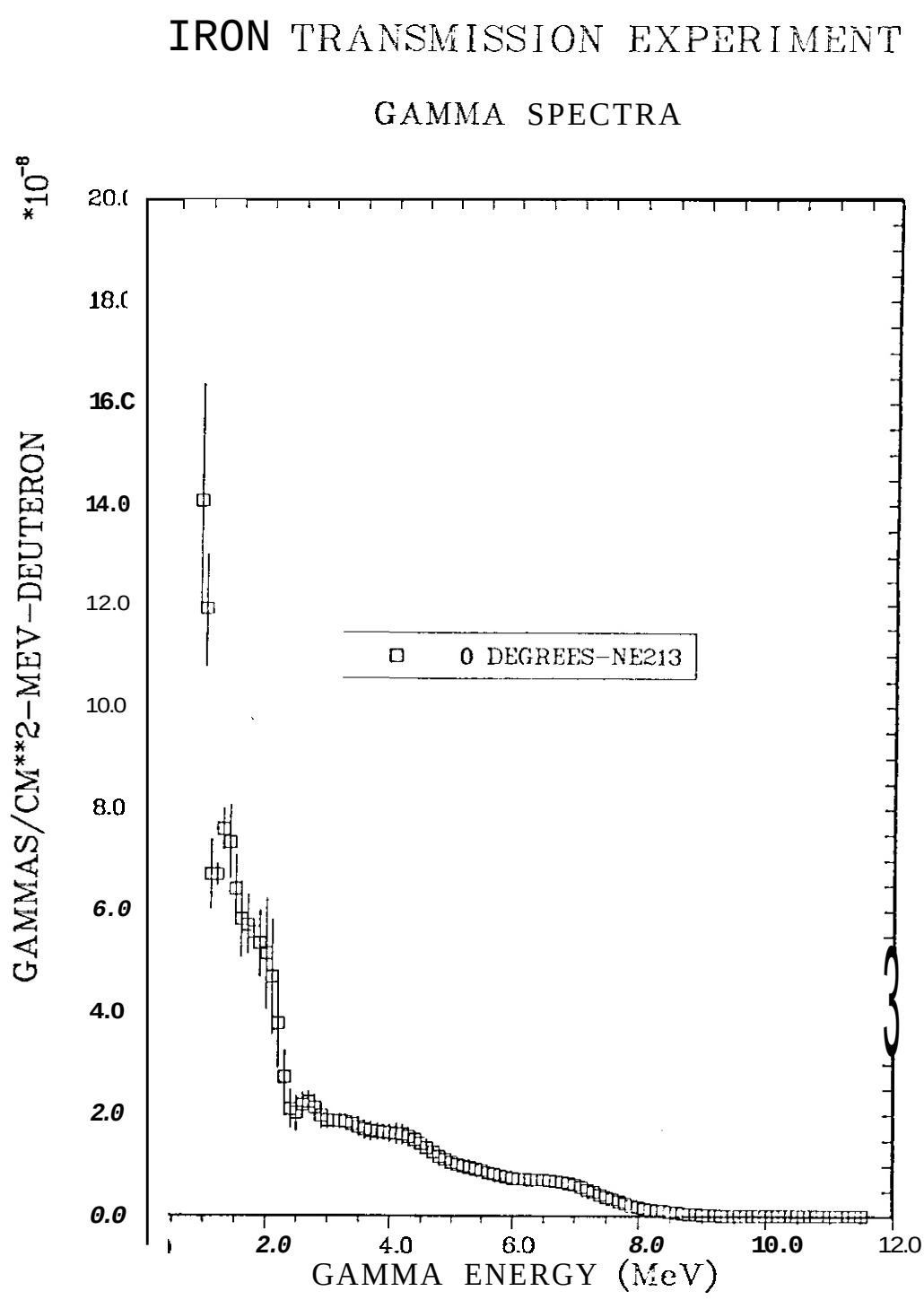

Figure 3.

FIGURE 3. Gama Spectrum Emerging From Fe Block at 0" From 35 MeV d on Li

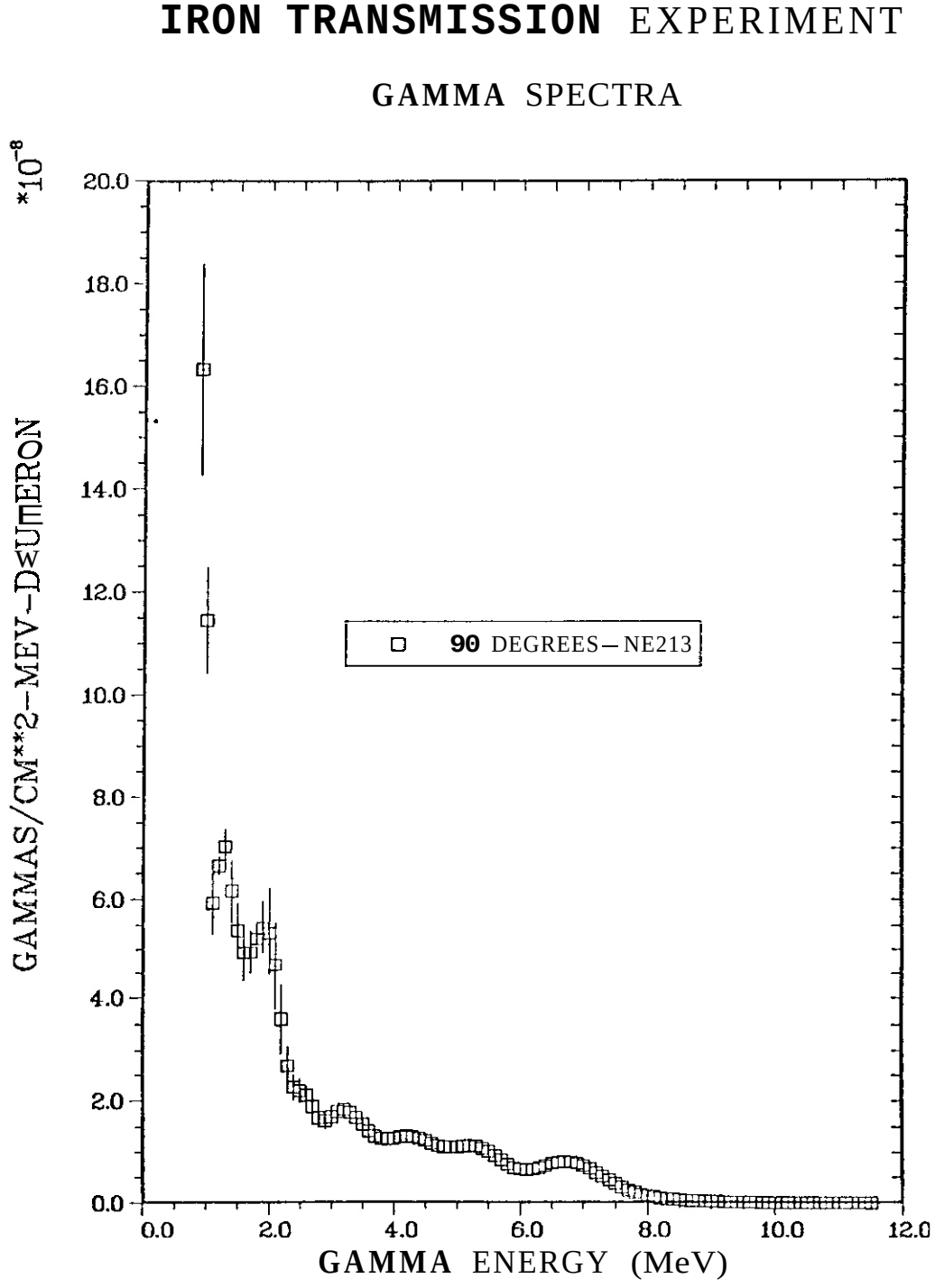

FIGURE 4. Gamma Spectrum Emerging From Fe Block at 90" From 35 MeV d on Li

CHAPTER 2

DOSIMETRY AND DAMAGE PARAMETERS

I. PROGRAM

Title: Dosimetry and Damage Analysis
Principal Investigator: L. R. Greenwood
Affiliation: Argonne National Laboratory

II. OBJECTIVE

To establish the best practicable dosimetry for mixed-spectrum reactors and to provide dosimetry and damage analysis for OFE experiments.

III. RELEVANTS DAFS PROGRAM TASK/SUBTASK

SUBTASK II.A.1.1 Flux-spectral definition in a tailored fission reactor.

SUBTASK II.A.1.3 Applications.

IV. SUMMARY

Dosimeters have been completed for the ORR-TBC07 tritium breeding experiment. Plans are being made for the ORR-MFE3 experiment as well as irradiations in the Omega West Reactor. The status of all reactor irradiations is summarized.

V. ACCOMPLISHMENTS AND STATUS

L. R. Greenwood (ANL)

The status of all current MFE reactor irradiations is summarized in Table I. The spectral measurement in Omega West (Los Alamos Scientific Laboratory) is now scheduled for October 1980. Plans are also being formulated to monitor the first experiments (Hanford-Livermore) in Omega West. The ORR-MFE3 irradiation is now being planned with the Naval Research Laboratory. The ORR-MFE2 dosimeters should be returned to ANL during October.

Table I. Status of Reactor Experiments

Facility/Experiment		Status and Comments
ORR	- MFE1	Analysis complete.
	- MFE2	Samples en route to ANL.
	- MFE3	Planning in progress.
	- MFE4A,B	Irradiation in progress.
	- TBC07	Analysis complete.
HFIR	- CTR 30,31,32	Irradiation in progress.
	- T1,T2	Irradiation in progress.
	- RB1	Planning in progress.
Omega West	- Spectral Run	Irradiation planned 10/80.
	- HEDL 1	Planning in progress.
EBR II	- 287	Analysis in progress.

Dosimetry has been completed for the ORR-TBC07 experiment at the pool-side facility. A small capsule of Li_7Pb_2 was irradiated for 698 hours in order to simulate tritium breeding for a fusion reactor blanket. Gamma analysis of thermocouple wires showed a total fluence of 9.6 x 10^{20} n/cm^2 with a thermal component of 4.35 x 10^{20} n/cm^2 and a value of 3.17 x 10^{19} n/cm^2 above 1 MeV. The gradients along the capsule appeared to be less than 10%. Tritium production was estimated to be 1.43 x 10^{-7} atoms per lithium atom per second. However, time-dependent self-shileding should be included and we estimate that 14-20% of the lithium was burned-up and converted to tritium. More precise calculations may be done pending tritium analysis of the capsule.

VI. REFERENCES

None.

VII. FUTURE WORK

Some of the irradiations listed in Table I will continue for several years and many more will be added. Helium measurements (Rockwell International) are also included in most of the irradiations.

VIII. PUBLICATIONS

A paper entitled "The Use of Uncertainty Data in Neutron Dosimetry" was presented at the Workshop on Evaluation Methods and Procedures at Brookhaven National Laboratory, September 22-25, 1980, and the text will be published in the proceedings.

I. PROGRAM

Title: Dosimetry and Damage Analysis
Principal Investigator: L. R. Greenwood
Affiliation: Argonne National Laboratory

II. OBJECTIVE

To establish the best practicable dosimetry for high-energy neutron facilities.

III. RELEVANTS DAFS PROGRAM PLAN TASK/SUBTASK

SUBTASK II.A.2.2 Flux-spectral definition in RTNS II.

IV. SUMMARY

Preliminary results are presented for the joint characterization with RIES and LLL. Thermal and room-return neutrons are clearly evident.

V. ACCOMPLISHMENTS AND STATUS

L. R. Greenwood (ANL), D. Kneff (RIES), M. Guinan (LLL)

Preliminary dosimetry results are available from the characterization experiment performed at RTNS II during June 23 - July 3, 1980. A more complete description of the experimental arrangement can be found in our previous report (DOE/ER-0046/2) and in the contribution by RIES in this report. Analysis of the Au, Co, Ag, Ti, Mn, Cu, and Zr radiometric dosimeters has now been completed at ANL. The remaining foils are being counted at LLL and He samples at RIES. Most of the He specimens were also gamma counted.

Selected counting results are presented in Table I. Several important conclusions can be drawn from the data, as follows:

1. The fast (14.8 MeV) flux follows a $1/R^2$ dependence beyond 5 cm from the source. Closer in, finite size effects reduce the flux as expected.

2. The thermal flux appears to be nearly isotropic with remarkably little variation throughout the target room.

3. Beyond 1 meter from the source the thermal flux becomes comparable to the fast flux and it equals the fast flux at the back wall of the target room. If epithermal neutrons are considered, then the flux below 1 MeV is much larger than indicated by the thermal values.

4. The $^{59}Co(n,p)/(n,2n)$ activity ratio clearly shows an increase beyond 1 meter from the source, indicating the presence of room-return neutrons in the 2-10 MeV energy range. These lower energy neutrons account for about 20-40% of the 14 MeV flux. Close to the target the ratio is higher since the foils subtend a larger angular range and the extended source (~1 cm diameter) increases the average angle well beyond 0° where the $^{59}Co(n,2n)$ cross section declines due to decreasing neutron energy.

The above analysis is only preliminary since more data will be included later from RIES and LLL. More reactions and neutronic calculations will be used to define the room-return flux in the 2-10 MeV energy region. The analysis of the thermal flux is especially difficult since only three reactions are available and the epithermal flux is unknown. In fact, the present data strongly indicates the presence of a significant epithermal flux. However, more measurements may be needed to unfold the low-energy neutron spectrum.

Table I. Preliminary Fluence Measurements at RTNS II

June 23 - July 3, 1980

Irradiation Time = 251.62 h (115.85 h Live)

0° Position[a] (cm from source)	Fluence (n/cm^2) 14.8 MeV[b]	Thermal' ($\times 10^{12}$)	Ratio Thermal / Fast	Ratio[d] $^{59}Co(n,p)/(n,2n)$ ($\times 10^{-2}$)
0.26[a]	8.30 x ▮	-▮- ~ ~	---	6.09
0.93	1.91 x ▮	--▮ ~ ~	---	5.79
5.	1.55×10^{16}	2.9	1.9×10^{-4}	5.70
15.	1.57×10^{15}	3.1	2.0×10^{-3}	5.77
30.	4.02×10^{14}	3.1	7.7×10^{-3}	5.75
120.	2.50×10^{13}	2.9	0.12	6.09
380.[a]	2.44×10^{12}	3.0	1.2	7.09

[a] Approximate positions. The first entry is immediately behind the target. The last entry corresponds to the back wall of the target room.

[b] 14.8 MeV values deduced from the $^{197}Au(n,2n)$ reaction assuming a cross section of 2.12 b.

'Thermal values deduced from $^{59}Co(n,\gamma)$ reaction assuming a pure Maxwellian spectrum, the thermal cobalt cross section (37.3 b) and neutron self-shielding corrections. Values have large errors (see text).

[d] This ratio clearly indicates room-return neutrons at the far positions. Angular effects explain the large ratios close to the target (see text).

VI. REFERENCES

None.

VII. FUTURE WORK

More detailed flux mapping will be performed as more data becomes available. In order to elucidate the low energy flux, plans are being made to measure cadmium ratios for several reactions.

VIII. PUBLICATIONS

None.

I. PROGRAM

Title: Helium Generation in Fusion Reactor Materials
Principal Investigators: D. W. Kneff and Harry Farrar IV
Affiliation: Rockwell International, Energy Systems Group

II. OBJECTIVE

The objectives of this program are to measure helium generation rates of materials for Magnetic Fusion Reactor applications in the various neutron environments used for fusion reactor materials testing, to characterize these neutron test environments, and to develop helium accumulation neutron dosimeters for neutron fluence and energy spectrum dosimetry in these test environments.

III. RELEVANT DAFS PROGRAM PLAN TASK/SUBTASK

SUBTASK II.A.2.2 Flux-Spectral Definition in RTNS-II
SUBTASK II.A.4.2 T(d,n) Helium Gas Production Data

IV. SUMMARY

A two-week irradiation to characterize the RTNS-II neutron field was completed during the report period. The objectives of this irradiation, which was conducted jointly with L. R. Greenwood (ANL) and M. W. Guinan (LLNL), were to characterize in detail the high-flux region of the RTNS-II neutron field, further develop neutron dosimetry for long-term T(d,n) experiments, and measure total helium generation cross sections of numerous fusion reactor materials, pure elements, and isotopes. Helium analyses and cross section determinations have been completed for the separated isotopes of iron previously irradiated in RTNS-I. Rockwell personnel participated in the September 1980 Fusion Materials Irradiation Test Facility (FMIT) Dosimetry Workshop at HEDL.

V. ACCOMPLISHMENTS AND STATUS

A. Characterization of the RTNS-II Neutron Field -- D. W. Kneff, B. M. Oliver, M. M. Nakata, and Harry Farrar IV (Rockwell International, Energy Systems Group)

A joint Rockwell International-Argonne National Laboratory (ANL)-Lawrence Livermore National Laboratory (LLNL) neutron characterization irradiation was completed at the Rotating Target Neutron Source-I1 (RTNS-II) during the current reporting period. The objectives of this experiment were to (1) characterize in detail the primary irradiation volume of the RTNS-II neutron field for small target experiments; (2) further develop neutron dosimetry for long-term irradiation experiments at this facility; (3) measure the total helium generation cross sections of several materials of direct interest to the magnetic fusion reactor development program; and (4) cross-calibrate RTNS-II active neutron detectors and measure RTNS-II target room return neutrons. The irradiation accumulated a total integrated beam current of 929,000 nC and a maximum neutron fluence of ~9 x 10^{17} n/cm^2.

The experimental geometry for this irradiation is shown schematically in Figure 1, and the irradiation assembly is shown in its experimental configuration in Figure 2. The assembly consisted of a set of three stainless steel arcs mounted concentrically with the RTNS-II neutron source at source distances of 5, 15, and 30 cm, and a small stainless steel capsule mounted in the high-flux region adjacent to the front of the rotating target assembly. Sets of radiometric dosimetry foils were mounted at source angles of 0^o, 15^o, 30^o, 45^o, and 60^o on the three arcs. Additional foil sets were mounted along the source axis 1.2 m from the rotating target face, on the back wall of the target vault, and on the faces of the proton recoil and ionization chamber neutron monitors. Single crystals of ^{10}B were also mounted at some of these locations to determine the low-energy neutron fluence by helium accumulation neutron dosimetry.

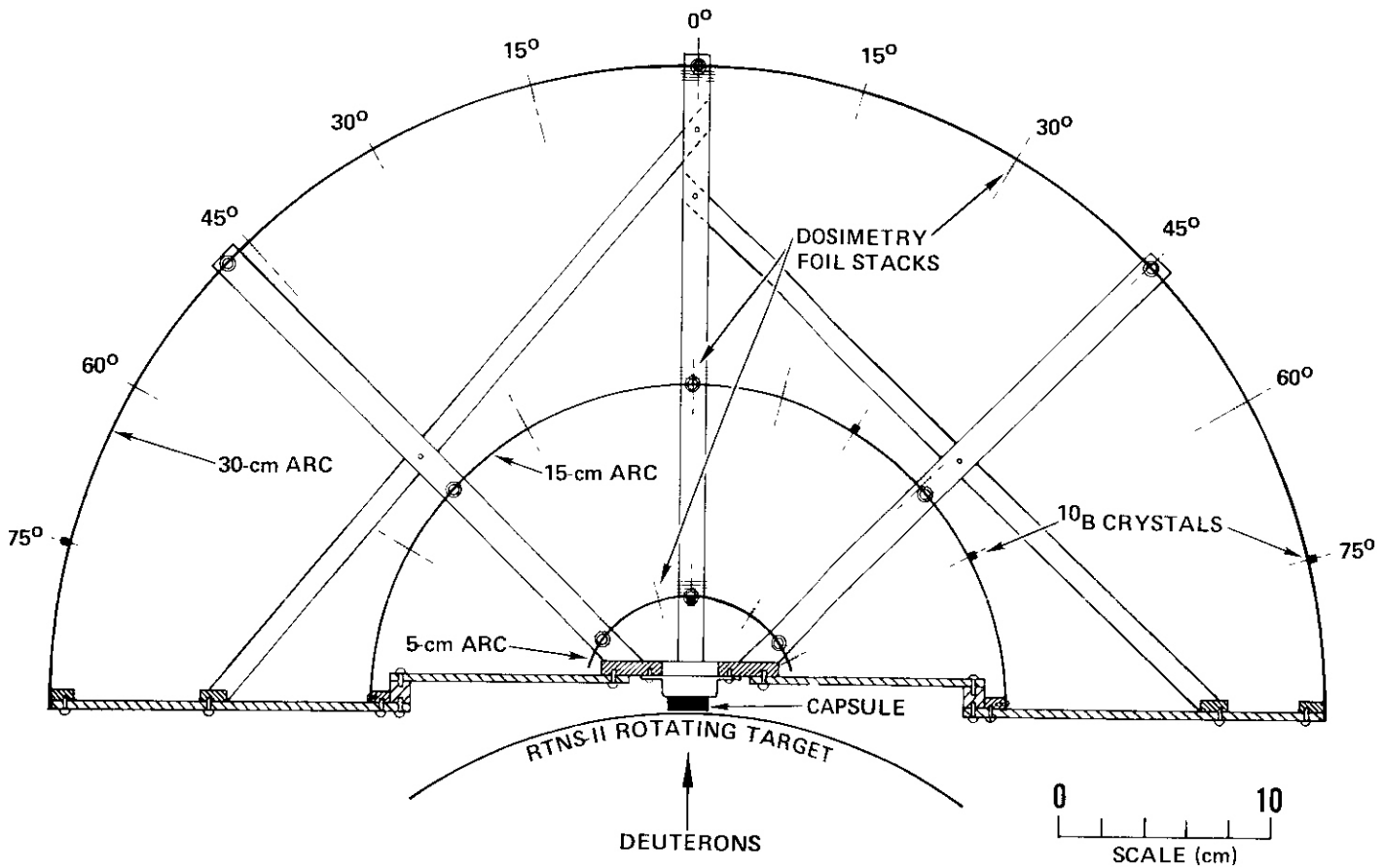

FIGURE 4 Irradiation Geometry for RTNS-II Characterization

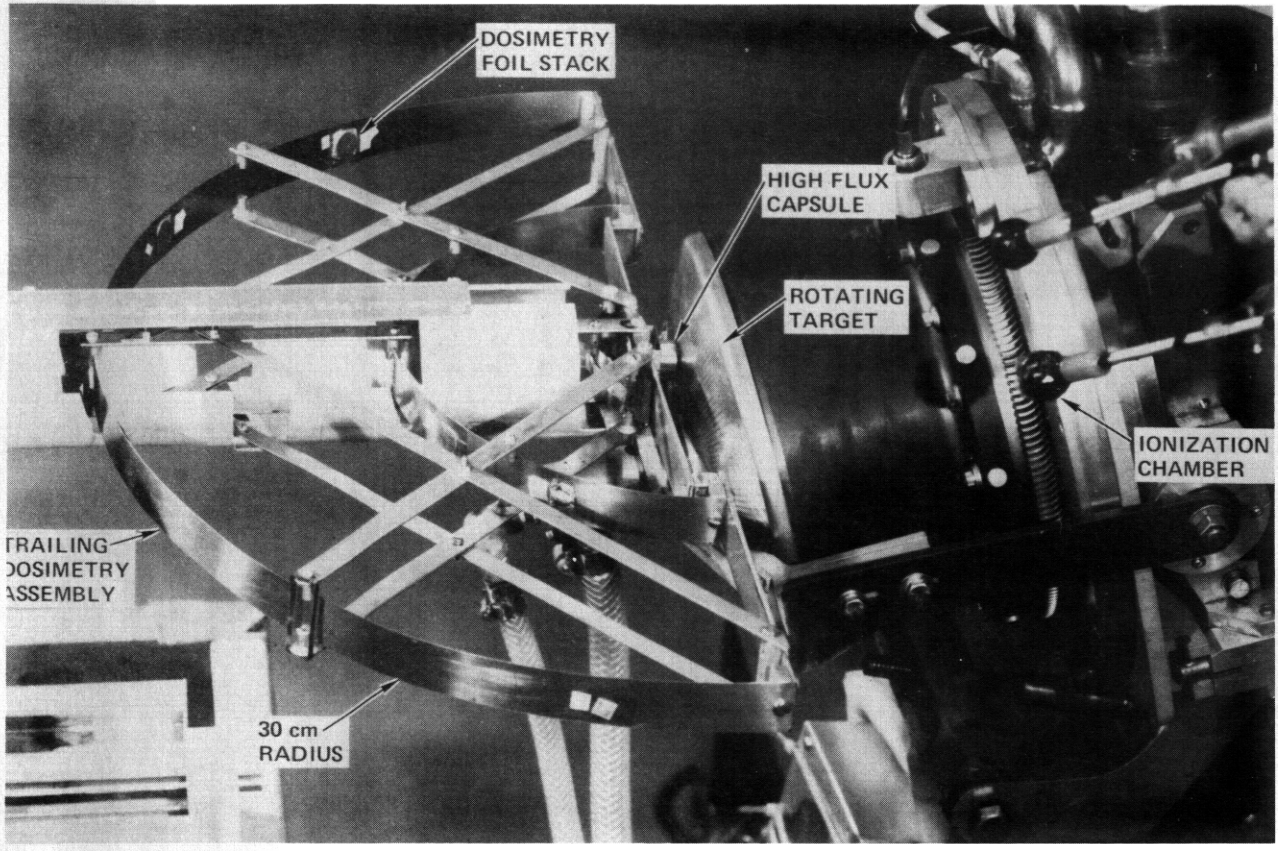

FIGURE 2. RTNS-II Irradiation Assembly in its Experimental Configuration.

The high-flux irradiation capsule is shown schematically in Figure 3. It contained a total of 90 pure elements, separated isotopes, alloys, compounds, and helium accumulation neutron dosimeters, sandwiched between layers of radiometric dosimetry foils. Most of these materials were included as multiple specimens for total helium production cross section measurements and are listed in Table 1. Several of the materials, including powdered compounds and other materials that could potentially lose helium, were vacuum-sealed in miniature platinum capsules. Measurement of the helium in the compounds will provide total helium production cross sections for the elements Li, N, O, F, and S, and the two separated isotopes of lithium.

Analyses of the materials irradiated in this experiment have been initiated. The radiometric foils were segmented after the irradiation for counting at ANL and LLNL. Several of the separated isotope helium specimens were also counted to determine other cross sections of interest in these materials. The materials will be shipped to Rockwell in October, at which time the helium accumulation neutron dosimetry wire rings will be segmented, and the analyses of the helium generation specimens by high-sensitivity gas mass spectrometry will begin. The analyses of these materials will be supported jointly by the Department of Energy's Offices of Magnetic Fusion Energy and Basic Energy Sciences.

B. Helium Production Cross Sections for the Separated Isotopes of Iron -- D. W. Kneff, B. M. Oliver, and Harry Farrar IV (Rockwell International, Energy Systems Group)

The helium analyses have been completed for the three separated isotopes of iron which were incorporated in the second Rockwell International RTNS-I irradiation. Cross section values have been derived by combining the helium results with the fluence map constructed for this irradiation.[1] The results are presented in Table 2. They correspond to an average incident neutron energy of 14.8 ± 0.1 MeV.

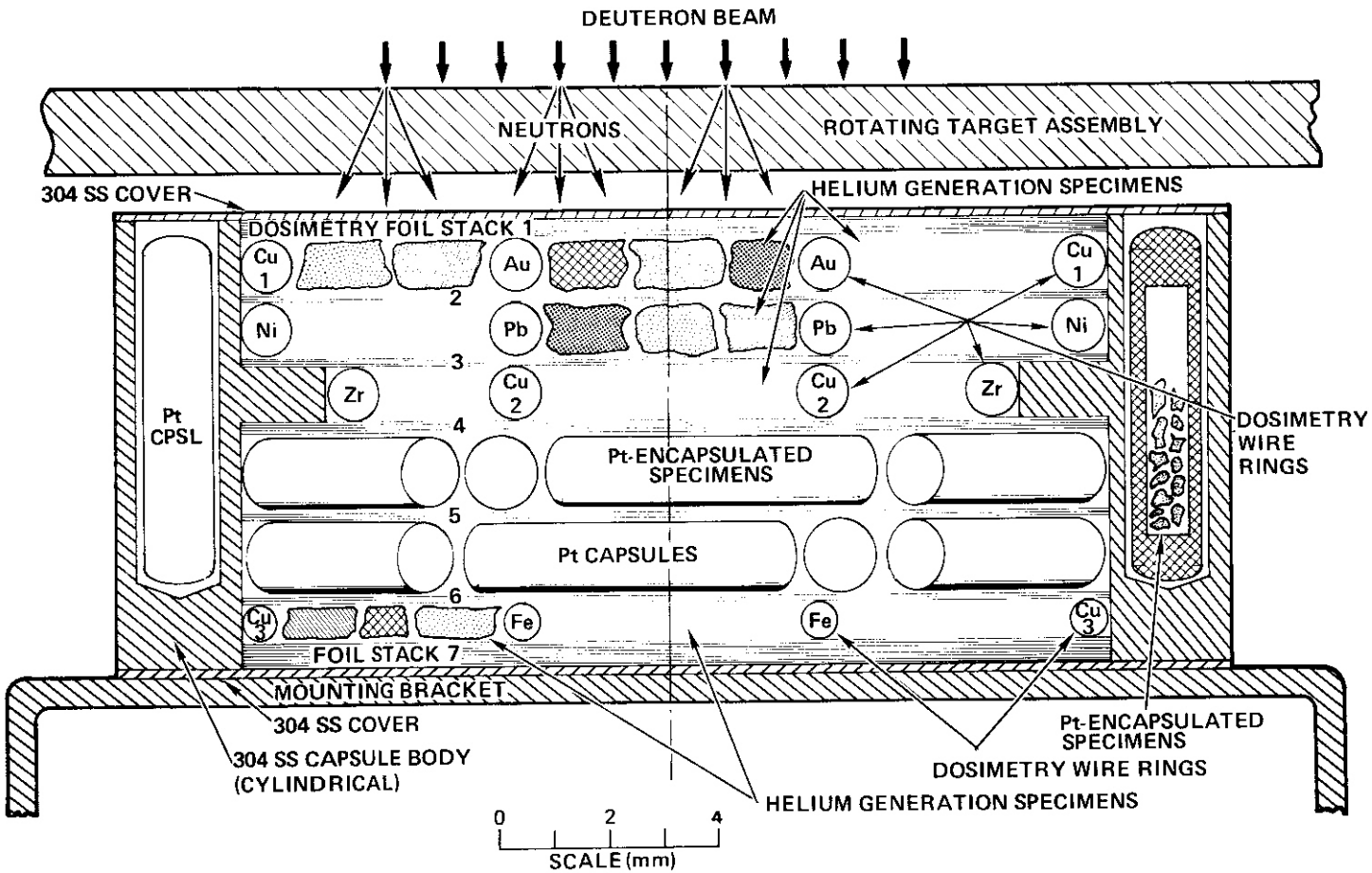

FIGURE 3 RTNS-II High-Flux Irradi Capsule.

Be	Ta
B, B-10,11	W, W-182,183,184,186
C (diamond, graphite)	Pt
Al	Au
Si	Pb, Pb-204,206,207,208
Ti, Ti-46,48,49,50	
V	
Cr, Cr-50,52,53,54	ZrN (for N)
Mn	Nb_2O_5 (for O)
Fe, Fe-54,56,57,58	PbO (for O)
co	PbF_2 (for F)
Ni, Ni-58,60,61,62,64	PbS (for S)
Cu, Cu-63,65	LiF, ^{6}LiF, ^{7}LiF (for Li,Li-6,7)
Y	
Zr	
Nb	
Mo, Mo-92,94,95,96,97,98,100	316 stainless steel
Ag	HT-9
Sn, Sn-116,117,118,119,120,122,124	9 Cr-1 Mo

TABLE 2

Fe(n,total helium) CROSS SECTIONS FOR 14.8-MeV NEUTRONS

Material	Cross Section (mb)		
	Present Work	Charged-Particle Measurements[b]	Evaluation[c]
	88 ± 6	79 ± 13	73
	45 ± 4	41 ± 7	38
^{57}Fe		-	-
	20 ± 2	-	-
	48 ± 3[a]	43 ± 7	39

[a]Kneff, et al., Reference 1

[b]Grimes, et al., Reference 2

'Arthur and Young, Reference 3

These cross sections were evaluated by first determining the cross sections for the isotopically enriched helium specimens. The individual isotopic cross sections were then derived by solving a matrix of equations to correct the specimen cross sections for the contribution from the other iron isotopes present. The isotope ^{57}Fe was not included in this irradiation, so the matrix was completed by using the previously measured cross section of natural iron.(1) Although the subsequent matrix gave an estimated (n,total helium) cross section for ^{57}Fe, it is not reported because of the relatively large uncertainties resulting from the very small abundance of this isotope in the analyzed samples. This isotope has since been included in the RTNS-II irradiation described above, and its cross section will be measured directly as part of the analysis of that experiment.

Table 2 also compares the present results with previously reported charged-particle measurements of Grimes, et al.,[2] and a recent cross section evaluation by Arthur and Young.[3] The agreement is within the quoted uncertainties, although there appears to be a small systematic difference. It is also of interest to compare the present $^{54}Fe(n,total\ helium)$ cross section (88 mb) with radiometric measurements of the $^{54}Fe(n,\alpha)^{51}Cr$ cross section. This is possible because the (n,α) reaction channel is expected to account for about 98% of the (n,total helium) cross section at this energy.[3] The radiometric measurements[4] generally group around ~100 mb, which is not inconsistent with the present value.

VI. REFERENCES

1. D. W. Kneff, B. M. Oliver, M. M. Nakata, and H. Farrar IV, "Helium Generation Cross Sections for Fast Neutrons," Symposium on Neutron Cross Sections from 10 to 50 MeV, Brookhaven National Laboratory, N.Y., May 1980 (to be published).

2. S. M. Grimes, R. C. Haight, K. R. Alvar, H. H. Barschall, and R. R. Borchers, "Charged-Particle Emission in Reactions of 15-MeV Neutrons with Isotopes of Chromium, Iron, Nickel, and Copper," Phys. Rev. C 19, 2127 (1979).

3. E. D. Arthur and P. G. Young, "Evaluation of Neutron Cross Sections to 40 MeV for $^{54,56}Fe$," Symposium on Neutron Cross Sections from 10 to 50 MeV, Brookhaven National Laboratory, N.Y., May 1980 (to be published).

4. See, for example, O. I. Garber and R. R. Kinsey, Neutron Cross Sections, Volume II, Curves, BNL 325, Third Edition, National Neutron Cross Section Center, Brookhaven National Laboratory, January 1976.

VII. FUTURE WORK

Analyses of the helium accumulation dosimetry materials and separated isotopes from the RTNS-II characterization irradiation will begin during the next quarter. The helium analyses of the RTNS-I and Be(d,n)-irradiated

separated isotopes of molybdenum, which require special analysis procedures, have been initiated. Work on obtaining helium production cross sections for the Be(d,n) neutron environment will continue.

I. PROGRAM

Title: Damage Analysis and Dosimetry Radiation Damage Analysis
Principal Investigators: A. N. Goland and D. F. Dell
Affiliation: Brookhaven National Laboratory

II. OBJECTIVE

Radiation damage analysis studies associated with the use of electrical insulators in fusion reactors.

111. RELEVANT DAFS PROGRAM PLAN TASK/SUBTASK

SUBTASK II.A.2.4 Flux Spectral Definition in FMIT

SUBTASK II.B.1 Calculation of Displacement Cross Sections

IV. SUMMARY

Damage parameters for a selected group of ceramics have been calculated. The relative importance of neutron, gamma-ray, and ionization-induced damage has been estimated, and directions for future investigations have been identified. The program terminated at the end of this reporting period.

V. ACCOMPLISHMENTS AND STATUS

The long-term objective of this program has been to provide a theoretical framework for evaluating the effects of energetic neutrons and gamma rays on the properties of nonmetals, especially ceramics. To ensure its immediate relevance to fusion materials research, and to the goals of the DAFS program plan, the prcgram has focussed upon radiation effects in the FMIT environment and in other sources of current interest to the Materials and Radiation Effects Branch of the OFE.

The first step in this study was to evaluate the numerous processes by which permanent damage can be produced in insulators by radiation. Insulators of interest are multicomponent solids, and the existing calculational methods for evaluating radiation-damage parameters in metals had to be adapted to this new class of materials.

Damage functions analogous to those for metals had to be generated, and therefore, the research effort has been closely coupled to that of Parkin and Coulter at LASL who have been developing this formalism. These two program essentially have constituted the DAFS-supported theoretical effort on insulators. The Brookhaven portion of the program has reached a natural endpoint inasmuch as it has produced a comparison of the relative importance of various displacement cross sections, and has identified areas of basic research that require further attention if better estimates of the displacement processes are to be made. Therefore, the BNL program will be terminated at the close of FY 80.

In brief the accomplishments of the research effort have been:

1. Characterization of the spectral and spatial dependence of the FMIT neutron and gamma-ray environment.

2. Calculation of damage parameters for a selected group of ceramics.

3. Comparison of the relative importance of neutron-induced, gamma-ray induced and ionization-assisted recoil damage in some ceramics.

Emphasis has been placed on multicomponent nonmetals that are candidate materials for use as insulators in fusion reactors. Therefore, damage parameters have been evaluated for C, Al_2O_3, Si_3N_4 and $MgAl_2O_4$ exposed to neutron spectra from the EBRII, ORR, or LPTR reactors, to a hypothetical first-wall fusion spectrum, to a 14-MeV neutron spectrum or to a neutron spectrum from the Fusion Materials Irradiation Test Facility (FMIT) now being built at the Hanford Engineering Development Laboratory (HEDL).

The damage analysis program DON[1] has been used in conjunction with Coulter and Parkin[2] damage energy and displacement functions for multi-component systems to evaluate damage parameters. In addition to the displacements produced by neutrons, those caused by ionization-assisted processes have been investigated. The latter investigation was hampered by the paucity of experimental ionization cross-section data, and the resultant displacement cross sections should be regarded as tentative. The spectrumaveraged cross sections for Al_2O_3, Si_3N_4 and $MgAl_2O_4$ are listed in Tables I, II and III, respectively. Evaluations were made for the six neutron spectra mentioned earlier. The results for Al_2O_3 and Si_3N_4 exposed to a first-wall fusion spectrum and to a preliminary FMIT spectrum were published previously;[3] they are included here for completeness. It should be noted that these calculations were carried out using the total displacement functions n_{ij} rather than the more recently available net displacement functions g_{ij} deduced by Coulter and Parkin.

VI. REFERENCES

1. D. M. Parkin and A. N. Goland, Radiation Effects 28, 31 (1976).

2. C. A. Coulter and D. M. Parkin, J. Nucl. Mater. 88, 249 (1980)

3. G. F. Dell, H. C. Berry, A. N. Goland and O. W. Lazareth, J. Nucl. Mater. 85/86, 373 (1979).

VII. FUTURE WORK

In the course of these investigations a number of areas requiring further research were identified:

1. High energy neutron cross sections (>20 MeV) need to be calculated for a number of elements, and compared with a few experimental results. Experimental work in this area needs to be encouraged.

2. Very few cross sections for K- and L-shell ionization are known so that it is difficult to assess ionization-assisted damage processes. Here again as in the neutron case, further attention to experiments and theory is required.

3. The relationships between defect production and physical properties are difficult to establish. This field has hardly been explored for imperfect solids, especially nonmetals. Some progress has been made with respect to mechanical properties. In general, however, emphasis should be placed upon changes induced in all properties of significance to fusion reactor operation - electrical, mechanical and thermal.

VIII. PUBLICATIONS

Some results of these investigations are summarized in:

1. Calculation of Radiation Damage in Insulators for Fusion Reactors, G. F. Dell, H. C. Berry, A. N. Goland and O. W. Lazareth, J. Nucl. Mat. 85/86, 373 (1979).

2. Damage Parameters for Nonmetals in a High-Energy Neutron Environment, G. F. Dell, H. C. Berry, O. W. Lazareth and A. N. Goland. Proc. Symp. Neutron *Cross* Sections from 10-50 MeV, BNL, May 12-14, 1980. (To be published)

3. A manuscript in preparation will summarize all the results of the research program.

TABLE I. SPECTRUM AVERAGED DAMAGE CROSS SECTIONS FOR Al_2O_3

Neutron Spectra	FMIT	First Wall	14 MeV	EBR II	ORR	LPTR
E_n MeV)	10 ∃∇	∃ ∃≤	14 2	0 4∃2	0 ≤31	0 5∃5
Displacement Cross Sections						
P.C. Displacement Fcns.						
$\bar{\sigma}_{dis}$(Al) (b/atom)	1081.0	723.6	1193.0	580.0	383.7	461.6
$\bar{\sigma}_{dis}$(O) (b/atom)	416.4	280.7	458.0	227.0	149.4	180.1
P.C. Damage Energy Fcns.						
$\bar{\sigma}_{dis}$(Al) (b/atom)	889.0	590.8	985.6	468.4	311.4	373.6
$\bar{\sigma}_{dis}$(O) (b/atom)	333.6	223.6	367.9	179.6	118.7	142.9
Robinson Damage Energy Fcns.						
$\bar{\sigma}_{dis}$(Al) (b/atom)	927.0	613.0	1033.0	482.0	321.4	385.0
$\bar{\sigma}_{dis}$(O) (b/atom)	346.0	213.2	383.4	184.7	122.3	147.0
Ionization Assisted Fcns.						
$\bar{\sigma}_{dis}$(Al) (b/atom)	71.0	35.8	83.6	16.6	16.7	17.4
$\bar{\sigma}_{dis}$(O) (b/atom)	180.0	90.5	213.2	41.4	41.6	43.3
Damage Energy Cross Sections						
P.C. Damage Energy Fcns.						
$\bar{\sigma}_{dam}$(nuclear) (b-eV/atom)	$1.05 \cdot 10^5$	$6.91 \cdot 10^4$	$1.15 \cdot 10^5$	$5.51 \cdot 10^4$	$3.66 \cdot 10^4$	$4.39 \cdot 10^4$
$\bar{\sigma}_{dam}$(electronic) (b-eV/atom)	$8.03 \cdot 10^5$	$3.50 \cdot 10^5$	$1.08 \cdot 10^6$	$8.84 \cdot 10^4$	$9.36 \cdot 10^4$	$9.17 \cdot 10^4$

TABLE II. SPECTRUM AVERAGED DAMAGE CROSS SECTION FOR Si_3N_4

Neutron Spectra	FMIT	First Wall	14 MeV	EBRII	ORR	LPTR
E_n (MeV)	10 ≤	3 ≤	14	0.4≤	0.≤31	0.5≤5
Displacement Cross Sections						
P.C. Displacement Fcns.						
$\bar{\sigma}_{dis}$(Si) (b/atom)	352.8	209.4	407.0	138.7	103.6	116.1
$\bar{\sigma}_{dis}$(N) (b/atom)	395.7	239.1	454.3	163.0	119.1	134.8
P.C. Damage Energy Fcns						
$\bar{F}_{dis}$(Si) (b/atom)	262.≤	155.1	3°3.4	1°Z.0	▽5.4	85.4
$\bar{F}_{dis}$(N) (b/atom)	341.z	204.1	3≤3.4	1≤▽.1	100.2	113.8
Robinson Damage Energy Fcns.						
$\bar{\sigma}_{dis}$(Si) (b/atom)	287.8	152.8	333.9	111.2	81.9	92.8
$\bar{\sigma}_{dis}$(N) (b/atom)	341.0	201.1	395.7	131.8	97.1	110.0
Ionization Assisted Fcns						
$\bar{\sigma}_{dis}$(Si) (b/atom)	≤5.8	≤2.1	81.▽	1z.≤	13.4	13.1
$\bar{F}_{dis}$(N) (b/atom)	1≤5.1	≤5.6	z45.0	3≤.≤	39.6	39.0
Damage Energy Cross Sections						
P.C. Damage Energy Fcns.						
$\bar{\sigma}_{dam}$(nuclear) (b-eV/atom)	$9.81\cdot10^{4}$	$5.6\leq\cdot10^{4}$	$1.0\leq\cdot10^{5}$	$\leq.78\cdot10^{4}$	$z.76\cdot10^{4}$	$3.14\cdot10^{4}$
$\bar{\sigma}_{dam}$(electronic) (b-eV/atom)	$8.66\cdot10^{5}$	$3.6°\cdot10^{5}$	$1.1\leq\cdot10^{6}$	$\leq.81\cdot10^{4}$	$\leq.41\cdot10^{4}$	$7.44\cdot10^{4}$

TABLE III. SPECTRUM AVERAGED DAMAGE CROSS SECTIONS FOR $MgAl_2O_4$

Neutron Spectra	FMIT	First Wall	14 MeV	EBRII	ORR	LPTR
$\bar{E}_n$(MeV)	10 ∃7	∃ ∃≤	1⓪ Z	0 4∃2	0 ≤∃1	0 5∃5
			Displacement Cross Sections			
P.C. Displacement Fcns.						
$\bar{\sigma}_{dis}$(Mg) (b/atom)	77.7	53.3	8≤.2	4∃.8	28.2	∃4.0
$\bar{\sigma}_{dis}$(Al) (b/atom)	⁻77.1	121.2	19≤.3	9∃.5	64.6	⁻7.4
$\bar{\sigma}_{dis}$(O) (b/atom)	Ω84.7	217.9	20∃.2	10≤.7	68.8	∃2.8
Ionization Assisted Fcns.						
$\bar{\sigma}_{dis}$(Mg) (b/atom)	25.ד	12.9	30.∃	5.9	6.○	6.1
$\bar{\sigma}_{dis}$(Al) (b/atom)	48.Z	24.3	57.○	⁻1.2	11.∃	11.7
$\bar{\sigma}_{dis}$(O) (b/atom)	167.0	84.1	198.○	∃8.4	38.∃	40.2
			Damage Energy Cross Sections			
.C. Damage Energy Fcns.						
$\bar{\sigma}_{dam}$(nuclear) (b-eV/atom)	$1.0∃\cdot10^5$	$7.0○\cdot10^4$	$1.1^{○}\cdot10^5$	$5.7^{-}\cdot10^4$	$∃.7○\cdot10^4$	$4.46\cdot10^4$
$\bar{\sigma}_{dam}$(electronic) (b-eV/atom)	$8.0○\cdot10^5$	$3.4∃\cdot10^5$	$1.0∃\cdot10^6$	$8.8∃\cdot10^4$	$∃.2∃\cdot10^4$	$9.09\cdot10^4$

I. PROGRAM

Title: Irradiation Effects Analysis (AKJ)
Principal Investigator: D. G. Doran
Affiliation: Hanford Engineering Development Laboratory (HEDL)

II. OBJECTIVE

The objective of this work is to extend our knowledge of the energy dependence of damage by making use of available charged particle data. This is done by applying the damage function analysis method to deduce the primary recoil energy dependence of charged particle and neutron irradiation effects data.

III. RELEVANT DAFS PROGRAM TASK/SUBTASK

SUBTASK II.B.2.3 Cascade Production Methodology

IV. SUMMARY

Primary recoil damage functions for production of Frenkel pairs in copper, silver, molybdenum, and tungsten were deduced from changes in resistivity after irradiation with neutron or charged particles and from computer simulation data on displacement cascade production. In general a linear function of damage energy above approximately 1 keV gives a good correlation of Frenkel pair production in copper, silver, molybdenum, and tungsten for charged particle and neutron irradiations. The damage energy constant is inversely proportional to the square root of the target mass. A logarithmic recoil energy dependence at low energies is adequate for most applications.

V. ACCOMPLISHMENTS AND STATUS

The Correlation of Irradiation Effects Data Using Primary Recoil Spectra - R. L. Simons (HEDL)

1. INTRODUCTION

The low flux and small test volumes of neutron irradiation facilities other than fission reactors make it imperative that efficient utilization be made of available charged particle irradiation effects data. Whether the objective of a charged particle irradiation is to study a damage mechanism or to simulate directly some aspect of a neutron irradiation, the problem of relating charged particle and neutron irradiation is present. Consequently, it would be desirable to have a simple function which correlates the macroscopic property changes of a material due to charged particle and neutron irradiation. In order to determine this function we need a common characteristic of each type of radiation that accounts for differences between the deposition of the energy of the radiation particles. One common characteristic which depends on the energy of the radiation particles is the primary recoil spectrum. One possible means of deducing the dependence of a particular radiation effect on the primary recoil spectrum is by a method analogous to the damage function analysis (DFA). The damage function, i.e., the neutron energy dependence of irradiation induced property change, has successfully correlated macroscopic property changes due to the differences between the neutron spectra in which the material was irradiated [1,2]. The damage function is deduced by least square fitting or some other comparable method.

The objective of this work is to use the method of DFA to deduce the primary recoil energy dependence of the production of Frenkel pairs from measurements of change in resistivity induced by charged particles and neutron irradiations.

Odette et al [3] first applied DFA to try to deduce the recoil energy dependence, as well as the neutron energy dependence, of sputtering yields in potential neutron irradiation environments. From simulated experiments they concluded that, even with relatively large data errors, it should be possible to detect the existence of and deduce the form of the energy dependence of sputtering yields. They did not consider the use of charged particle data.

Averback, Benedek and Merkle [4,5] measured the change in residual electrical resistivity in thin film specimens of Cu and Ag after irradiation by charged particles with energies below 1 MeV at temperatures below 10K. They found that the apparent efficiency of Frenkel pair production, defined as the ratio of measured to theoretical values, decreased from near 1.0 to about 0.3 as the recoil spectrum was shifted to higher energies (by increasing the projectile mass or energy or both). Their efficiencies compared favorable with values deduced from neutron irradiations in moderated fission spectra, and Be(d,n) and T(d,n) spectra [6].

Merkle et al [7], who included the resistivity data from high energy proton and deuteron irradiations of Anderson and Sorenson [8] in their analysis, suggested that the decrease in damage efficiency occurs in the primary recoil energy region of 1-3 keV. Their modification to the displacement model (K-P) was a rather sharp deviation from the linear form between 1 and 3 keV.

The materials analyzed in this work include copper, silver, molybdenum, and tungsten. The references and types of irradiation sources are summarized in Table I. The radiation sources include electrons, charged particles ranging from protons to bismuth, and neutrons; in some cases, computer simulation data were used also.

TABLE I

RADIATION SOURCES AND REFERENCES FOR DATA USED IN THIS ANALYSIS

Material	Radiation Sources	References
Copper	Charged particles (0.7 keV < T_{max} < 900 keV)	4,5
	Fission and fusion neutrons*	9
	Thermal neutron (n,γ) recoil	11
	Computer simulation	12
Silver	Charged particles (0.7ev < T_{max} < 800 eV)	4,5,7,8
	Electrons (T_{max} < 60eV)	10
	Fission neutrons*	9
	Thermal neutron (n,γ) recoil	11
Molybdenum	Electrons (T_{max} < 0.3 keV)	13
	Thermal neutron (n,γ) recoil	14
	Fission and fusion neutrons*	9
Tungsten	Electrons (T_{max} < 77 keV)	15,16
	Thermal neutron (n,γ) recoil	11
	Computer simulation	17

*Fission neutron sources include:

- Pure U^{235} fission spectrum
- CP5 reactor at Argonne National Lab.
- Livermore pool Type Reactor (LPTR)

Fusion neutron sources include:

- Be(d,n) source
- T(d,n) source

2. METHOD OF ANALYSIS

The damage analysis method involves solving a set of integral equations of the form

$$\int P_i(T)\,\nu(T)\,dT, \quad i = 1,2,3,\ldots N \tag{1}$$

where N_i is the number of Frenkel pairs in the i^{th} recoil spectrum divided by the particle fluence, $P_i(T)$ is the primary recoil spectrum for an incident particle of type i, and $\nu(T)$, the function to be deduced, is the number of Frenkel pairs per primary knock-on atom (PKA). $\nu(T)$ goes to zero at the minimum energy, T_0, required to displace an atom from its normal lattice site. The primary recoil spectra $P(T)$ are zero above T_m, the maximum energy that the bombarding particle can impart to a lattice atom. Thus, the limits of integration are bounded by T_0 and T_m for all radiation particles. The analysis requires the measurement of N_i in a variety of primary recoil spectra produced by neutrons or charged particles with different incident energy or mass or both. The form of the energy dependence of recoil damage, $\nu(T)$, is then deduced by least square fitting or some other comparable analysis. In this work both linear and nonlinear least square fitting codes were used to deduce $\nu(T)$ from the set of integral equations.

2.1 PKA SPECTRA

2.1.1 Charged particles

The primary recoil spectra for the charged particle data are based on Lindhard's formulation of electronic and nuclear stopping of atoms in solids. There were two types of charged particle experiments: (1) particle stopped in the target, and (2) charged particle passed through the target after making one collision.

When the incident particle is stopped in the target, the number of defects produced per incident ion is given by the expression

$$N = \int_0^{E_o} dE \int_{T_o}^{\gamma E} \frac{d\sigma}{dT}(E,T)\, S^{-1}(E)\nu(T)\, dT \qquad (2)$$

where $\frac{d\sigma}{dT}(E,T)$ is the collision cross section for the incident particle, $S(E)$ is the sum of the electronic and nuclear stopping powers, and $\nu(T)$ is the number of defects per primary knock-on atom. The integration limits on T run from the minimum energy required to create a displaced atom T_o to the maximum energy γE an ion of energy E can transfer to a lattice atom in an elastic collision $\left[\gamma = 4\, M_1 M_2/(M_1 + M_2)^2\right]$. Since the incident charged particle is stopped in the target, the integration limits on E run from zero to the initial charged particle energy E_o.

If we change the order of integration, and consequently the limits of integration, Equation (2) is reduced to a single integration as in Equation (1). Thus,

$$N = \int_{T_o}^{\gamma E_o} P(T)\, \nu(T)\, dT \qquad (3)$$

The effective primary recoil spectrum, defined independently of where in the specimen a primary is produced, is then

$$P(T) = \int d\sigma(E,T)\, S^{-1}(E)\, dE \qquad (4)$$

The Lindhard collision cross section was used for $\frac{d\sigma}{dT}(E,T)$ [18,19]. The stopping power function $S(E)$ is the sum of Lindhard's electronic stopping

power function and nuclear stopping power function based on the Thomas-Fermi model of the atom [20].

For the data [7,8] based on the passage of a light charged particle through the target the primary recoil spectrum was defined as

$$P(T) = \frac{d\sigma}{dT}(E,T) \tag{5}$$

where $\frac{d\sigma}{dT}(E,T)$ is determined for the average energy of the particle in the target. The average energy was determined from the incident energy, total stopping power data, and the thickness of the thin film target [7]. In this work it was assumed that nonelastic nuclear reactions were negligible for the high energy deuteron and proton data ($E < 10$ MeV).

2.1.2 (n,γ) Recoil

Several methods of characterizing (n,γ) recoil damage by recoil energy were tried. The primary recoil spectra due to (n,γ) recoils were calculated with the gamma spectra of Orphan et al. [21]. The gamma spectra were tabulated in 30 to 38 energy groups with gamma yields for each group. In the most elaborate procedure, recoil spectra were determined by the relationship

$$P(T) = \sum_i P_i(T)\, Y_i \tag{6}$$

where Y_i is the gamma yield for the i^{th} gamma energy group, and $P_i(T)$ is the recoil spectrum for the i^{th} gamma energy group. $P_i(T)$ was determined from equation (4) with the incident ion energy E given by

$$E = (\bar{E}_\gamma)^2/2\, mc^2. \tag{7}$$

E_γ is the average gama energy for the i^{th} group. However, this method did not produce a successful correlation of the (n,γ) recoil data. The (n,γ) recoil data deviated from the rest of the data by amounts ranging from +35% for Cu to several orders of magnitude (low) for W. It was apparent from this analysis that gamma-gamma correlations and decay schemes for the activated nucleus are needed to correctly determine the recoil spectrum. In the interim the maximum recoil energies calculated by Coltman et al.[11] were used as monoenergetic spectra. With the exception of the silver (n,γ) datum point, the measured and calculated number of Frenkel pairs agreed within 20% or less. An alternate method of determining mean recoil energies was devised which provided an improved correlation of the data but it was not used in this work (see Appendix A).

2.1.3 Electrons

It was necessary to use electron irradiation data near the displacement threshold in order to establish accurately the threshold energy. Electron irradiation data for recoil energies above the threshold were included in the analysis of the Ag, Mo, and W data. The PKA spectra were calculated from the Mott scattering cross section for electrons which was determined from the work of Oen [22]. The electron data were plotted as pointwise measurements at the average damage energy. The average recoil energy was defined as

$$\bar{T} = \frac{\int_{T_o}^{T_{max}} T\sigma_m(T, E_e)\, dT}{\int_{T_o}^{T_{max}} \sigma_m(T, E_e)\, dT} \qquad (8)$$

where $\sigma_m(T,E_e)$ is the Mott scattering cross section for an electron of energy E_e, T_{max} is the maximum energy that the electron can impart to the target atom. T_{max} is given by

$$T_{max} = \left(\frac{560.8}{A}\right) \varepsilon \, (\varepsilon + 2) \tag{9}$$

where A is the atomic mass and $\varepsilon = E_e/m_e c^2$. The appropriate electronic loss correction was applied to the recoil energy to convert it to damage energy.

2.1.4 Computer Simulation Data

Fully dynamical computer simulation data were used with the irradiation data for copper and tungsten. In fact, the tungsten analysis was based almost entirely on simulation data. The justification for using the simulation data is that the interatomic potentials, on which they are based, were calibrated with a number of macroscopic integral quantities such as the elastic constants. The determination of $\nu(T)$ was done with and without the simulation data for copper in order to test how the simulation data might bias the solution.

2.2 $\nu(T)$ FUNCTION

In this work the recoil damage function $\nu(T)$ was determined by linear or nonlinear least squares analysis. Consequently a functional form for $\nu(T)$ was needed. The recoil damage function $\nu(T)$ for production of secondary displaced atoms by the primary recoil atom is generally expressed in a modified Kinchin and Pease form

$$\begin{aligned} \nu(T) &= 0 && T < E_d \\ \nu(T) &= 1 && E_d \leqq T \leqq 2E_d \\ \nu(T) &= \frac{\beta T_{DAM}}{2E_d} && T > 2E_d \\ T_{DAM} &= T[1-kg(\varepsilon)]^{-1} \end{aligned} \tag{10}$$

where E_d is the effective displacement energy, β (generally taken to be 0.8) is a correction factor to account for the softness of real potentials and T_{DAM} is the recoil damage energy. The constant k is a function of the charge and mass of the target atom and ε is a dimensionless relative energy. Robinson [8] determined an empirical representation, $g(\varepsilon)$, of Lindhard's energy loss correction due to electron excitation. Merkle's comparison of measured and calculated Frenkel pair production due to high energy recoils (>10 keV) shows an efficiency (<1) that is independent of energy[7]. Thus, at high recoil energies the damage function should be proportional to the damage energy.

As the energy is decreased, the efficiency rises to unity. A very low energy behavior was found by examining the simulation data on copper. These data are shown in a semi-logarithmic plot in Figure 1.

The form adopted for the composite recoil damage function combines the high and low energy behavior:

$$\nu(T) = (A \ln T + BT + C)\, T_{DAM}/T. \qquad (11)$$

Equation (11) corresponds to the modified Kinchin-Pease model with $\beta/2E_d$ replaced by an energy dependent efficiency function of the form

$$\beta/2E_d = (A \ln T + BT + C)/T \qquad (12)$$

Both Robinson [23] and Beeler [24] devised nonlinear functions of T_{DAM} to describe the departure of their two-body collision theory data from Equation 10. The nonlinearity arises from recombination of defects in overlapping branches of the evolving cascade. Robinson's function, analogous to a rate theory of recombination of defects, is in terms of the damage energy.

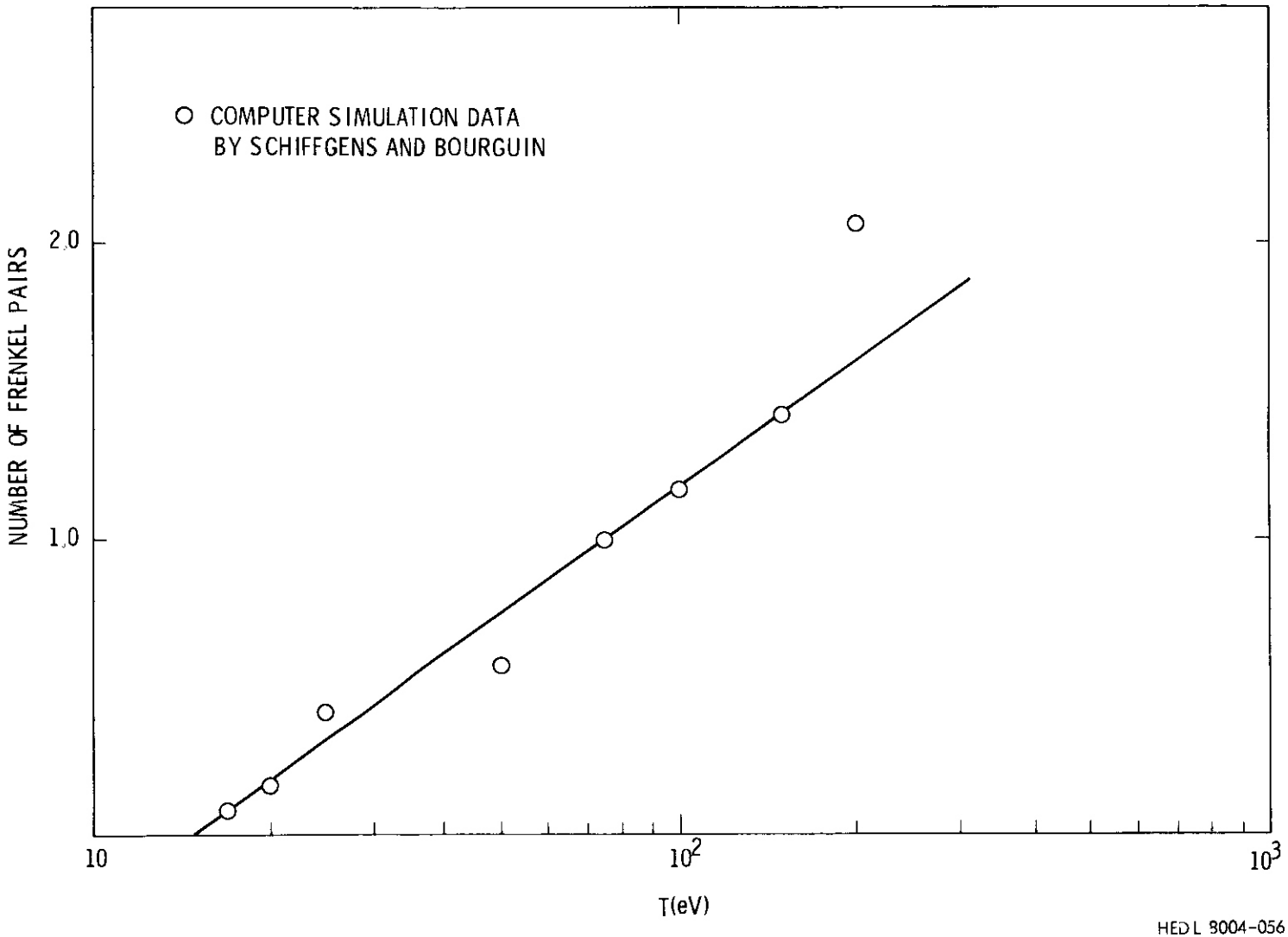

FIGURE 1. Defect Production Trend by Computer Simulation in Copper. No electronic loss included.

$$\nu(T_{DAM}) = \frac{T_{DAM}}{\alpha T_{DAM} + \beta} \quad , \quad 0.5 \leq T_{DAM} \leq 10 \text{ keV} \tag{13}$$

where a and β are fitted constants.

Beeler's function was entirely empirical in form and was a function of recoil energy

$$\nu(T) = \gamma_0 T - \gamma_1 T \ln T, \quad 0.5 \leq T \leq 20 \text{ keV} \tag{14}$$

where γ_0 and γ_1 are fitted constants. These functions are applicable to the damage energy region $0.5 \leq T \leq 20$ keV. However extrapolation to the >100 keV energy range shows that these functions deviate from one another by a factor of four or more.

In order to account for the potential departure of the high energy damage function from the T_{DAM} proportionality as predicted by the work of Robinson and Beeler, the BT term in equation (11) was replaced by functions similar to Equations (13) and (14). Thus two additional functions fit to the data are

$$\nu_R(T) = \left[A \ln T + \frac{}{\alpha T +} + C \right] T_{DAM} \tag{15}$$

and

$$\nu_B(T) = \left[A \ln T + \gamma_0 T + \gamma_1 T \ln T + C \right] \frac{T_{DAM}}{T} \tag{16}$$

It is noted that as long as $|\alpha T| << |\beta|$ Equations (15) and (16) reduce to the same form.

In this work the constants of Equations (11), (15), and (16) were fit to the data using either linear or nonlinear least squares methods [25,26]. The number of Frenkel pairs ranged from less than 1 to over 1000. Under

these circumstances the large values of the dependent variable control the fitting of the parameters. To bypass this problem the nonlinear code was run in a lognormal mode, that is, the residuals were in terms of the difference between logarithms. For the linear least squares application the fitted function was divided by the dependent variable. The residual then became the difference between 1.0 and the ratio of calculated to measured integral damage. Both methods were found to give nearly the same results in comparable cases.

3. RESULTS AND DISCUSSIONS

3.1 Copper

Figure 2 shows the three functions deduced for copper. Equation (11) (K-P function) and Equation (16) (B function) are nearly identical. At T_{DAM} = 1 MeV, the B function differs from the K-P function by less than 3%. Below T_{DAM} = 200 keV, Equation (15) (R function) follows the other two functions vary closely. Above 200 keV the R function curves down fairly abruptly. Sharp curvature from the K-P functions is not expected. The behavior of the R function around 1 MeV is probably due to a lack of damage response by the PKA spectra in that energy range. For example, the hardest PKA spectrum, Be(d,n), has only 5% of its damage response above 220 keV.

The lowest energy datum point of Shiffgen's (Figure 2) was used in this analysis to establish the threshold for the fitted functions. The remaining computer simulation data of Shiffgen's (although not used in this analysis) are in good agreement with the fitted curves. The agreement occurs inspite of the large uncertainty in his data due to the anisotropic nature of the production of Frenkel pairs near the threshold energy T_0 (i.e., $< 10T_0$). Both the (n,γ) and copper self ion data shown in Figure 2 were used as monoenergetic data in this analysis.

From a engineering point of view the most important applications are for neutron irradiations. A comparison of the deviations for the neutron

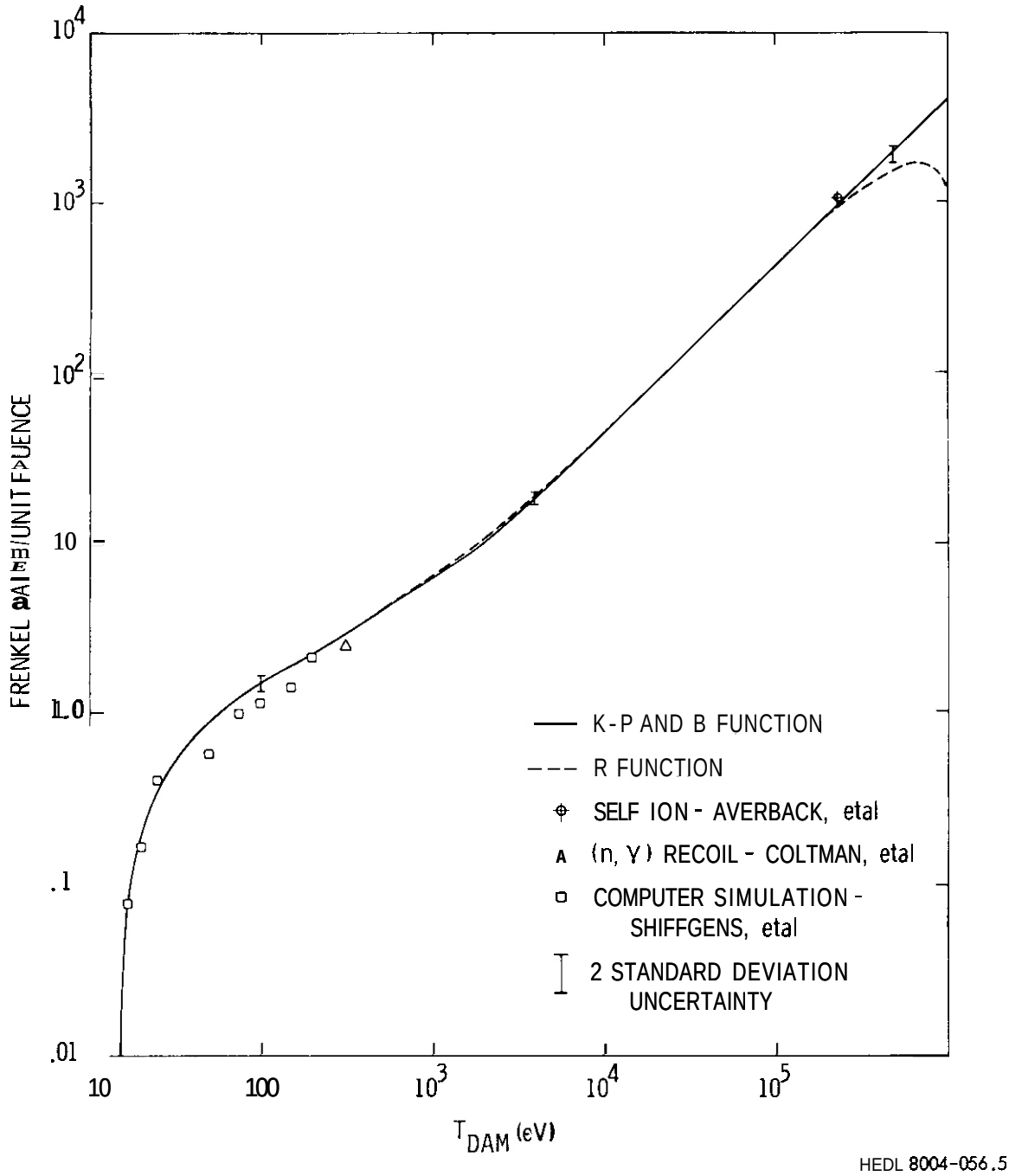

FIGURE 2. Defect Production Curves for Copper.

spectra used in the analysis is shown in Table 11. The overall standard deviations show little difference among the three functions. The R function shows the smallest deviations for individual neutron sources. However, the individual deviations for each neutron source show systematic trends which depend on the hardness of the neutron spectrum. For example, using the K-P function and the hardest neutron spectrum, Be(d,n), the calculated value is 22% high; for the next hardest spectrum, fission, measured and calculated values agree; and for the softest spectrum, CP5, the calculated value is 17% low. This systematic trend may be due to uncertainty in the PKA spectra or damage energy, but it also supports the deviation of the R function below the linear K-P function at high PKA energies.

Table III shows the measured data for copper for each radiation source, the percent deviation, and the 5% (T_L) and 95% (T_U) damage response limits for the K-P function. For the charged particles T_L changes very slowly with particle energy and mass. This occurs because most of the charged particle damage response is in the very low energy end of the 90% response range. In the neutron spectra, on the other hand, 95% of the damage response occurs above 1 keV. Thus neutron and charged particle data provide complementary coverage in the damage energy range between the threshold energy and about 500 keV.

The data from the self-ion bombardment of the copper target can be treated in two ways: as a single mono-energetic point or by integrating over the PKA spectrum. Both methods were used simultaneously in this analysis by entering the data as two pieces of information. As a mono-energetic point the measured number of Frenkel pairs was entered at a damage energy of 240 keV. As an integral over the PKA spectrum 90% of the damage response was between 86 eV and 199 keV. In the former case the calculated value is 13% low and in the latter case the calculated value is 8% high. The total difference of 21% could be due in part to the functional form of $\nu(T)$ and it could also reflect the uncertainty in the Lindhard scattering cross section used in calculating the PKA spectrum. A 20% uncertainty in

TABLE II

COMPARISON OF NEUTRON DATA FOR COPPER FOR THREE FUNCTIONS

Spectrum	Calculated Relative to Measured Integral Values (%)*		
	K-P	R	B
(n,γ)	18	18	15
Moderated Fission (CP5 reactor ANL)	-17	**-14**	-20
Pure Fission	-1	**1**	**-3**
Be(d,n)	22	14	17
All data	12	12	**13**

*table entry = $(\frac{C}{M} - 1) \times 100$

TABLE III

Input Data (Frenkel pairs/PKA), Deviation Between Calculated (K-P function) and Measured Data, and Damage Response Range for Copper

Radiation Source	N_f	%Dev.*	90% Damage Response Limits T_l (eV)	T_U(eV)
Self Ion (500 eV)	1059.	-13.	240000	-
(n,γ)	2.5	18.	315	-
30 keV H	7.1	-15.	23	405
15 keV H	5.6	-13.	23	331
20 keV D	15.4	-0.6	26	603
40 keV 3He	37.8	-3.7	29	1340
40 keV 4He	48.5	-1.9	29	2000
60 keV ^{4}Ne	47.5	16.	29	2450
225 keV Ne	389.	5.1	47	49200
500 keV Cu	1059.	7.6	86	199000
560 keV Kr	1399.	-4.5	105	243000
560 keV Ag	1419.	-0.9	122	243000
850 keV Bi	2276.	-3.3	149	297000
Be(d,n)	1050.	22.	40200	220000
CP5	212.	-17.	1100	163000
^{235}U Fission	369.	-1.2	9920	199000

* entry = $(\frac{F}{M} - 1) \times 100$

the PKA spectrum based on Lindhard's scattering cross section would not be unreasonable. No attempt has yet been made to study the sensitivity of the solution $\nu(T)$ to uncertainties in the PKA spectra.

3.2 Silver

The curves deduced from the silver data are shown in Figure 3. The spread in the three functions is obviously greater than that for copper. The R function curves upward at high energies. On physical grounds, this curvature is not expected and it probably is due to a lack of high energy neutron data, such as from a Be(d,n) irradiation. The B function also curves upward from the K-P function. This is not consistent with that found in Beeler's computer simulation work in copper, iron and tungsten [24]. The simulation work implies that the recombination models should show that damage falls below the linear trend of the K-P model as the damage energy increases. The trend shown by the R and B functions is probably a result of a lack of data at high energies.

There were two types of charged particle data for silver: (1) ions stopped in the target and (2) ions passed through the target with little loss of energy. In the latter case, the data were corrected by the experimenters for multiple scattering. This data set was found to disagree with the ion stopping data by as much as 40% at low particle energies ($T <$ 0.1 MeV). The low particle energy data were left out of the least square fitting calculation with little effect on the resulting solution. This was due to the redundancy in damage response and the large number of data points for silver (30 degrees of freedom).

The (n,γ) recoil and CP5 irradiation experiments provide the only neutron data available. The deviation for the CP5 spectrum was 1% with the K-P function, and 7 and 11% for the R and B functions, respectively. The (n,γ) recoil was a factor of two lower than the fitted curve. However, it is noted that in 1968 Coltman et al reported 0.61 Frenkel pairs by (n,γ) recoil in Mo, but more recent measurements reported in a 1975 paper gave

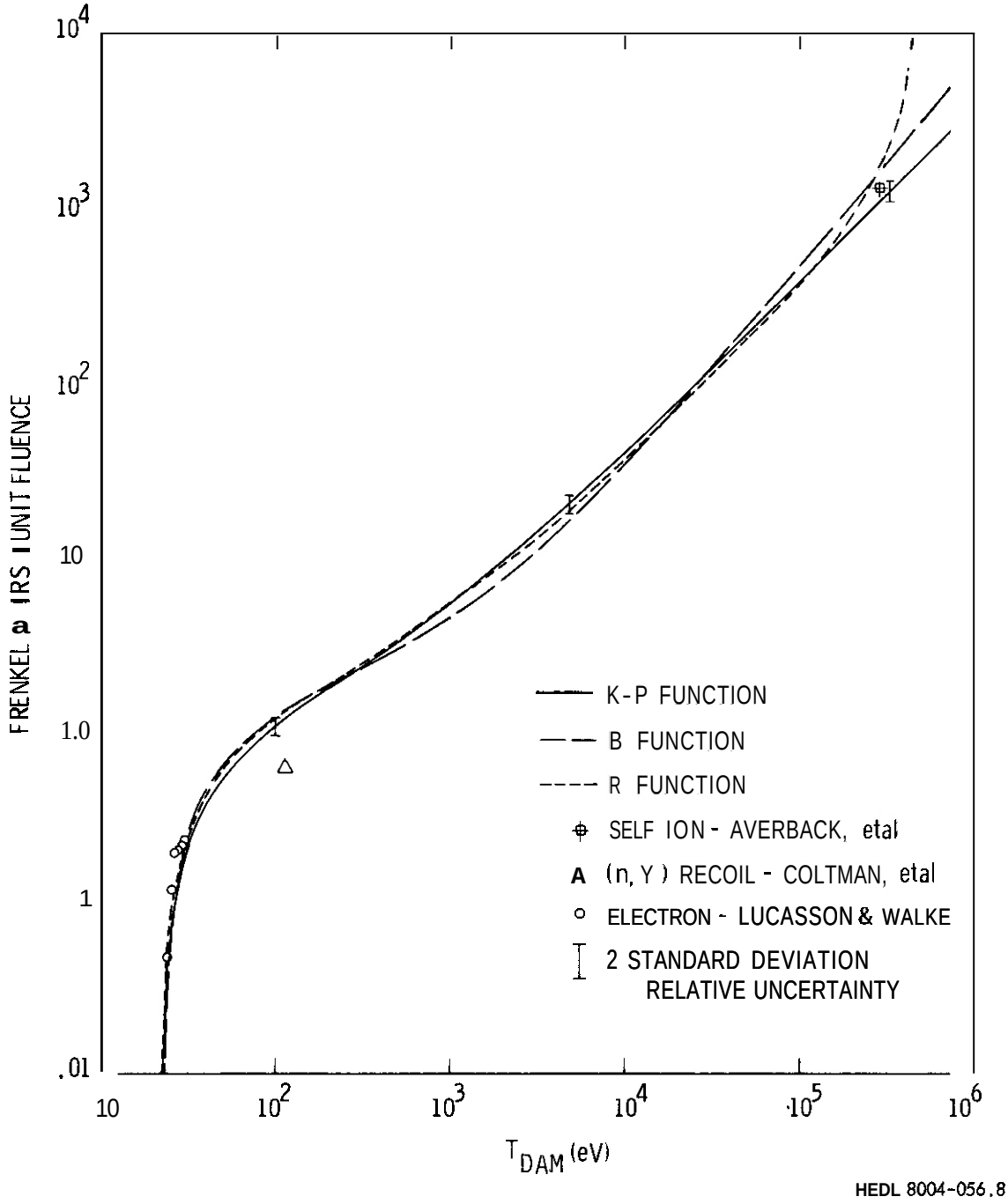

FIGURE **3.** Defect Production Curves for Silver.

nearly 1.2 Frenkel pairs. In light of the generally good agreement among the rest of the data, the silver (n,γ) recoil datum point is suspected to be in error.

The electron data near the threshold are seen to fit the curve fairly well even though only the lowest energy point was used in the analysis to establish the threshold. Without this point the solutions were highly variable in the threshold region.

Table IV shows the measured data for each radiation source, the percent deviation, and the 5% and 95% damage response limits for the K-P function for silver. One point of interest is that all the data from experiments allowing the charged particle to pass through the target have negative deviations on the order of 2-13%. This systematic difference is probably related to the primary recoil spectra used. However, Merkle [7] found that the Lindhard cross section gave better agreement than the Rutherford scattering cross section for this set of particle irradition data.

3.3 Molybdenum

The curves fit to the molybdenum data are shown in Figure 4. The K-P and B functions are essentially the same. The R function shows a physically unrealistic upward turn. Both the electron data and the (n,γ) recoil points correlate well with these functions. The electron data were not treated as pointwise data as shown in Figure 4. PKA spectra were calculated using the McKinley-Feshbach theory corrected by the work of Oen [22]. The calculated number of Frenkel pairs was then determined by integrating $\nu(T)$ with the PKA spectrum.

Table V shows the measured data for each radiation source, the percent deviation, and the 5% and 95% damage response limits for the K-P function for Mo. The electron data shown in Figure 4 are plotted at the mean damage energy. The data in Table V for the electron irradiation were converted to Frenkel pairs per unit fluence by dividing by the Mott scattering cross

TABLE IV

Input Data (Frenkel pairs/Unit fluence), Deviation Between Calculated (K-P function) and Measured Data, and Damage Response Range for Silver

Radiation Source	N_f	%Dev.*	90% Damage Response Limits T_I (eV)	T_{II}(eV)
3.9 MeV H	1.80	-7.7	43	60000
4.5 "	1.82	-7.3	43	73300
5.6 "	1.85	-7.8	43	89500
7.5 "	1.84	-7.7	43	10900
7.6 "	1.90	-10.0	43	10900
8.6 "	1.86	-8.2	43	134000
9.5 "	1.88	-9.8	43	135000
10.0 "	1.84	-10.0	43	163000
11.0 "	1.87	-13.0	43	163000
3.4 MeV D	1.92	-8.1	43	109000
4.3 "	1.87	-6.4	43	134000
5.4 "	1.93	-7.8	43	163000
6.4 "	1.93	-8.6	43	163000
7.5 "	1.92	-8.2	43	199000
8.9 "	1.95	-9.0	43	199000
9.3 "	1.95	-8.3	43	243000
10.0 "	1.87	-9.7	43	243000
11.0 "	1.85	-7.4	43	297000
20 keV H	3.38	29.	35	330
20 keV D	9.22	-8.2	35	600
40 keV ^{3}He	22.4	2.4	39	1340
40 keV ^{4}He	29.9	7.8	43	1640
30 keV 4He	28.0	2.6	43	1340
50 keV ^{4}He	28.0	21.	43	2000
70 keV Li	59.0	22.	47	4460
90 keV B	116.0	9.8	52	9920
150 keV O	182.0	19.	64	22000
180 keV Ne	236	19.	70	329000
290 keV Ar	498	11.	105	109000
540 keV Ag	1253	-6.4	220	297000
720 keV Bi	1533	7.5	270	363000
CP5	140	-1.5	1100	109000

* entry = $(\frac{P}{M} - 1) \times 100$

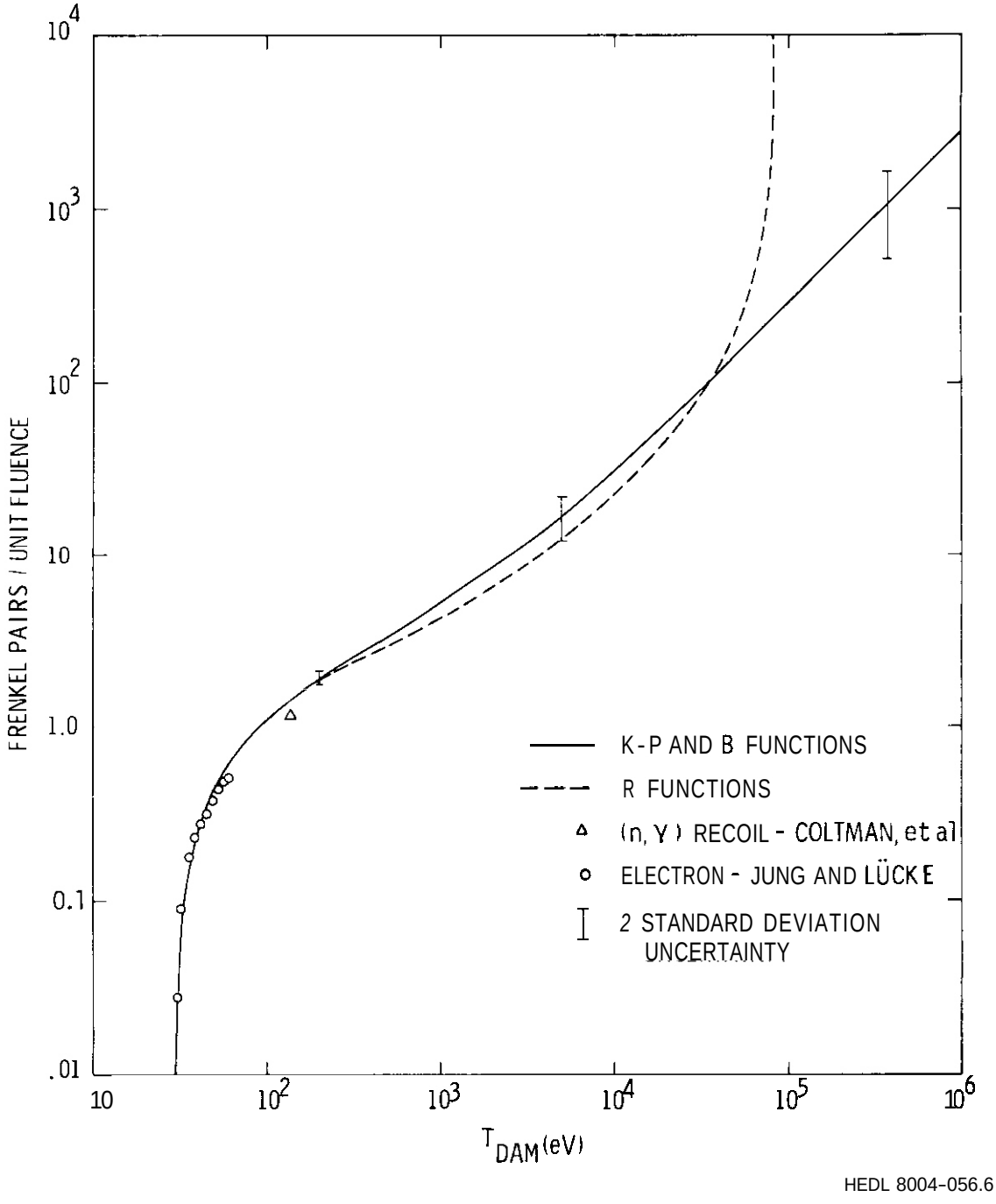

FIGURE 4. Defect Production Curves for Molybdenum.

TABLE V

Input Data (Frenkel/PKA), Deviation Between Calculated (K - P function) and Measured Data and Damage Response Limits for Molybdenum

Radiation Source	N_f	%Dev.*	90% Damage Response Limits T_I (eV)	T_{II} (eV)
(n,γ)	1.18	3.8	110.	-
0.85 MeV Electron	.032	9.5	34.9	36.
0.95 MeV Electron	.87	-39.	34.9	38.6
1.15 MeV Electron	.17	-19.	34.9	52.1
1.35 MeV Electron	.23	-7.1	38.6	70.3
1.55 MeV Electron	.27	-0.7	38.6	77.7
1.85 MeV Electron	.32	6.0	38.6	94.9
2.15 MeV Electron	.38	5.3	38.6	122.
2.45 MeV Electron	.44	3.2	42.6	149.
2.75 MeV Electron	.49	2.2	42.6	182.
3.05 MeV Electron	.50	7.1	42.6	222.
CP5	153.	6.5	737.	109000.
14 MeV	791.	1.7	27000.	444000.
LPTR	186.	-28.	1340.	109000.
Fission	283.	5.6	5400	134000.

* entry = $\left(\frac{E}{M} - 1\right) \times 100$

section for the appropriate electron energy. The values plotted in Figure 4 deviate from the calculated curve more than the deviations listed in Table V. This is probably due to the use of mean damage energy which is varying less rapidly than the actual $\nu(T)$ curve.

The neutron spectra show excellent correlation with the exception of the LPTR datum point. The CP5 spectrum, which is similar to the LPTR spectrum, shows good agreement with the calculated value. There was a measurement in a Be(d,n) spectrum [17] that was not used in this analysis because a PKA spectrum was not available. When a niobium PKA spectrum was used in place of the molybdenum PKA spectrum a 40% deviation from the rest of the data resulted.

3.4 Tungsten

The results for tungsten are shown in Figure 5. The experimental data for this material are limited to a few electron irradiations and a (n,γ) recoil point. All are at low energies. The bulk of data are from computer simulation of cascades in tungsten. Consequently, the analysis of the tungsten data is somewhat academic. However, it does enable one to compare how the various functions fit the simulation data which was meant to model a real material.

Most of the data were calculated by Guinan [17] with a fully dynamical computer code. Since he used two different potentials the data showed two different threshold energies. The data were normalized to a common damage energy threshold of 37 eV energy by multiplying the reported damage energy by 37 eV and dividing by the reported damage energy threshold. Beeler simulated cascades at 2.5 and 20 keV using a two-body collision model. These data were normalized to Guinan's point at 2.5 keV thus giving one additional "data point" at 20 keV. The normalization of Beeler's data is admittedly arbitrary (normalization is 0.4) in light of differences in interatomic potential, collision model, and, especially, displacement criteria.

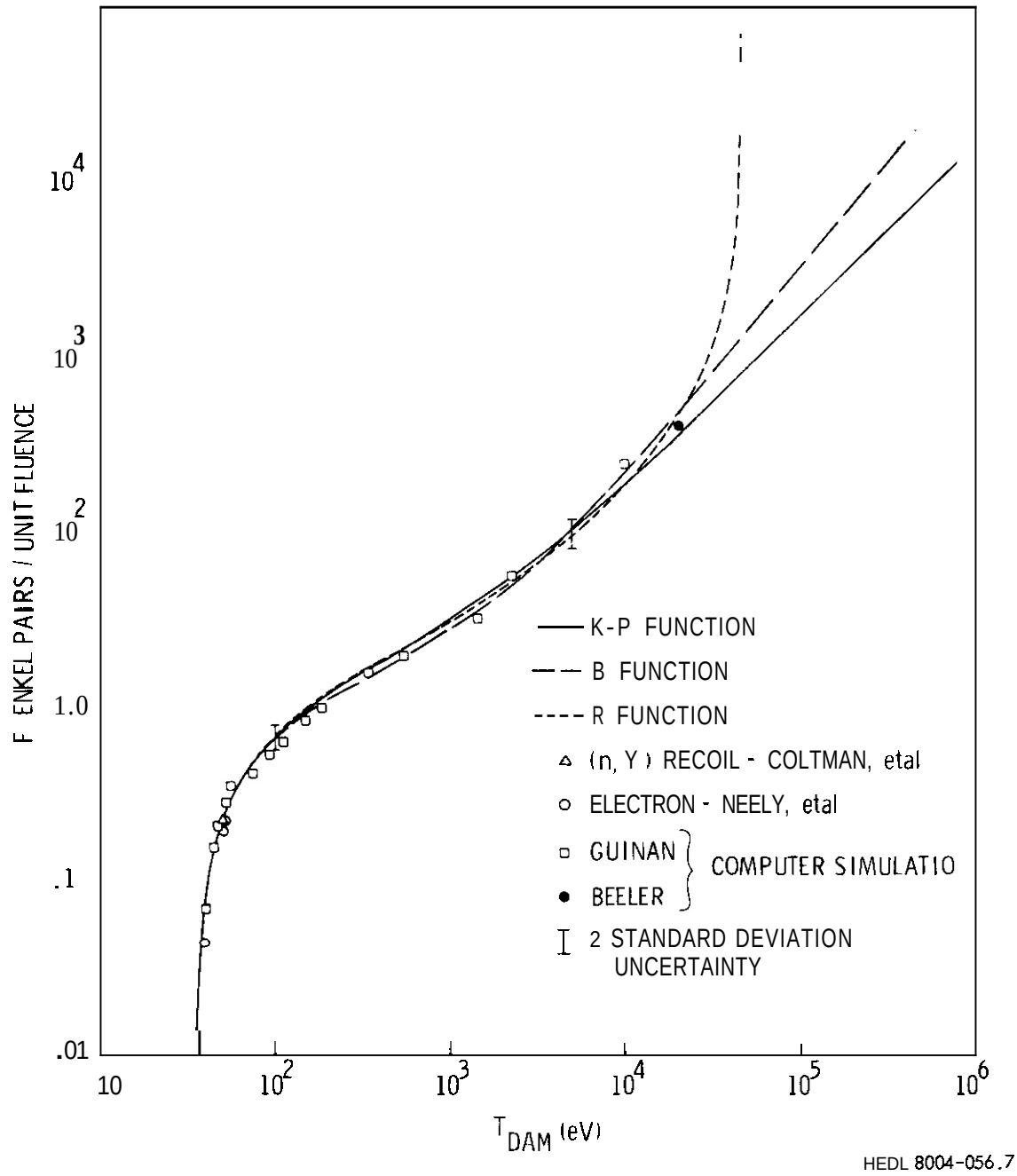

FIGURE 5. Defect Production Curves for Tungsten.

TABLE VI

Input Data, (Frenkel pairs/PKA), Deviation Between Calculated (K-P function) and Measured Data and Damage Energy for Tungsten

Radiation Source	N_F	%Dev.*	T_{DAM}(eV)
1.65 MeV Electron	0.045	18.1	39.6
2.0 MeV Electron	.20	2.4	50.6
2.1 MeV Electron	.23	-3.1	52.1
(n,γ) Recoil	.23	-2.6	50.8
Guinan	.073	-2.0	40.7
Guinan	.163	-30.9	44.4
Guinan	.216	-24.4	48.1
Guinan	.291	-32.6	51.8
Guinan	.364	-38.7	55.5
Guinan	.430	3.6	74.0
Guinan	.549	7.7	92.5
Guinan	.649	10.0	111.
Guinan	.854	8.4	148.
Guinan	1.000	9.8	185.
Guinan	1.62	3.6	342.
Guinan	3.30	20.8	142.
Guinan	2.00	10.6	541.
Guinan	5.80	-0.6	2260.
Guinan	25.0	-29.6	10000.
Beeler	41.0	-13.3	20000.

* entry = $(\frac{C}{M} - 1) \times 100$

The electron and (n,γ) recoil data show good agreement with the simulation data. The simulation data agree in general with the logarithmic function used in the low energy region. However, departure from the logarithmic function between 45 and 60 eV is noted. Above 20 keV there is a wide dispersion among the three models due to a lack of data. The R function shows a rapid upward turn which is physically unrealistic. The B function fits the data best but the positive departure above the K-P function is questionable. Below 20 keV the three functions are in reasonably good agreement.

Table VI shows the measured data used in the analysis and the percent deviation between measured and calculated values for the K-P function. The largest deviations are in the energy range 45 to 60 eV where the simulation data shows a more complex energy dependence than the logarithmic function.

3.5 Function Parameters

Table VII summarizes the coefficients for the three functions and four materials. The K-P function has two sets of coefficients for each material. The first are from the nonlinear fit of a log-normal distribution. The second are from the linear fit. It is apparent that the nonlinear and linear approaches give nearly identical results. None of the functions give an outstandingly lower percent deviation. In all cases (except W) the percent deviation is in the 10-15% range. The R function gives physically unrealistic results for Ag, Mo, and W in that the negative values of α allow the solution to go infinity. This may not be entirely the fault of the function but more due to the lack of appropriate data which determines physically realistic values of α and β. It is also noted that Robinson used his recombination model to describe displacement production in the 1 to 10 keV energy range.

For the B function the γ_1 coefficients for Cu and Mo are so small that they do not significantly affect the solution below T_{DAM} of 1 MeV. Thus, the K-P and B functions are essentially the same. The Ag and W

TABLE VII

COEFFICIENTS FOR THE THREE FUNCTIONS

K-P Function (Equation 11)

Material	% Deviation	A	B	C
cu	12.0	.699	3.85×10^{-3}	-2.04
	12.2	.690	3.76×10^{-3}	-2.01
Ag	12.1	.601	3.41×10^{-3}	-2.02
	12.7	.581	3.36×10^{-3}	-1.96
Mo	13.9	.877	2.80×10^{-3}	-3.18
	12.8	.872	2.74×10^{-3}	-3.16
W	19.1	.595	1.75×10^{-3}	-2.25
	18.3	.583	1.67×10^{-3}	-2.21

R Function (Equation 15)

Material	% Deviation	A	*a*	8	C
cu	12.0	.680	5.27×10^{-5}	248.	-1.99
Ag	11.5	.650	-1.75×10^{-4}	326.	-2.17
Mo	15.6	.944	-4.52×10^{-3}	641.	-3.37
W	18.8	.637	-9.45 x 10-3	723.	-2.40

B Function (Equation 16)

Material	% Deviation	A	γ_0	γ_1	C
cu	12.7	.679	4.02×10^{-3}	-2.26×10^{-5}	-1.98
Ag	10.6	.835	-2.18×10^{-3}	5.16×10^{-4}	-2.69
Mo	13.3	.878	$+2.55 \times 10^{-3}$	1.68×10^{-5}	-3.17
W	15.8	.751	-2.85×20^{-3}	4.90×10^{-4}	-2.73

results have negative γ_0 and positive γ_1 causing the solution to have a slope greater than the K-P function for these materials. It is also noted that the standard deviations for Ag and W are lower for the B function than for the K-P function. The steeper slope implies that recombination decreases as the cascade energy increases or the calculated damage energy is in error.

3.6 Uncertainty Analysis

Uncertainty in the coefficients was determined in accordance with the linear least squares method of Brown [24], and data were equally weighted. Thus, the resulting uncertainties are relative to the scatter about the fitted curve. If the uncertainty in the input data were known the absolute uncertainty would be greater than the relative uncertainty. The uncertainty in the integral measurement is generally considered to be small ($\pm$10%). The PKA spectra based on Lindhard's model have greater uncertainty (possibly in the 20-40% range) which is not well defined.

Table VIII shows the coefficients, their uncertainties, and the variance-covariance matrix for the K-P function and B function fit to the silver data. The uncertainty in the coefficients for the K-P function are less than 10%. This is typical for the other materials. The coefficients for the B function have higher uncertainties. However, the $\nu(T)$ function has a relatively small uncertainty (5-10% $\pm 1\sigma$) because of correlations between the coefficients in the covariance matrix. The γ_0 and γ_1 coefficients in the B function control the nonlinearity at high energies. The high uncertainty in these coefficients makes the significance of the non-linearity in this function questionable.

3.7 GENERALIZATION

Finally one would like to generalize the results so that the number of Frenkel pairs could be calculated for any material or radiation particle. The coefficients should be either constants for all conditions or related to known material parameters.

TABLE VIII

ERROR ANALYSIS FOR K-P FUNCTION [EQUATION (11)] FIT TO SILVER DATA

Coefficient	% Uncertainty*	Variance/Covariance Matrix** 1	2	3
A .581	8.2	2.24×10^{-3}	-8.32×10^{-6}	-7.12×10^{-3}
B .00336	6.5		-4.80×10^{-8}	2.59×10^{-5}
C -1.96	7.6			2.26×10^{-2}

* Standard error of all data is 12.7%

** Symnetric matrix

ERROR ANALYSIS FOR 8 FUNCTION [EQUATION (16)] FIT TO SILVER DATA

Coefficient	% Uncertainty*	Variance/Covariance Matrix** 1	2	3	4
A .835	9.2	5.93×10^{-3}	-1.01×10^{-4}	-1.75×10^{-2}	8.88×10^{-6}
γ_0 .00218	67.		2.10×10^{-6}	2.91×10^{-4}	-1.93×10^{-7}
C -2.69	8.5			5.17×10^{-2}	-2.55×10^{-5}
γ_1 5.16×10^{-4}	26.				1.80×10^{-8}

* Standard error of all data is 10.6%

** Symnetric matrix

A simple generalization is that the C coefficients for all the functions are related to the threshold energy. For example, $C = -(A \ln T_o + BT_o)$ for the K-P function. The accurate determination of the value of C (and T_o) relies on the use of electron data near the threshold energy. The response for heavier particles such as low energy protons generally lies well above the threshold and consequently does not establish the threshold behavior. Recasting the K-P function in terms of A, B, and T_o reduces the damage functions to two fitted coefficients and a material parameter known for a number of materials[27]. The K-P model would take the form

$$\nu(T) = \left[A \ln (T/T_o) + B (T/T_o) \right] \frac{T_{DAM}}{T}$$

Figure 6 shows the K-P function for all four materials plotted as a function of recoil energy divided by the threshold energy, T/T_o. The data shown are for production of Frenkel pairs by (n,γ) recoil. The data for hcp metals fall below the curves for Cu, Ag, and W, while the bcc and fcc data fall within the family of solutions. The two fcc data points falling below the family of curves are for Ag and Pd. The solution for Mo lies above the band of solutions for the other materials even though the (n,γ) datum point falls within the band. Since the A coefficient for Cu, Ag, and W fall within the range 0.6-0.7, one might infer. that most fcc and bcc metals would have a similar value for the A coefficient (0.65). In order to be conclusive, however, one would need to do a similar analysis on a wide range of materials.

The B coefficients for the K-P model appear to be dependent on the mass of the target material as expected since they incorporate E_d. To further substantiate this the data compiled by Kirk and Greenwood [9] were used to determine approximate values of B for other materials. The use of this data to determine B is a fairly good approximation since 95% of the damage in the neutron spectra occurs above 1 keV and the K-P function is linear in T_{DAM} above about 1 keV.

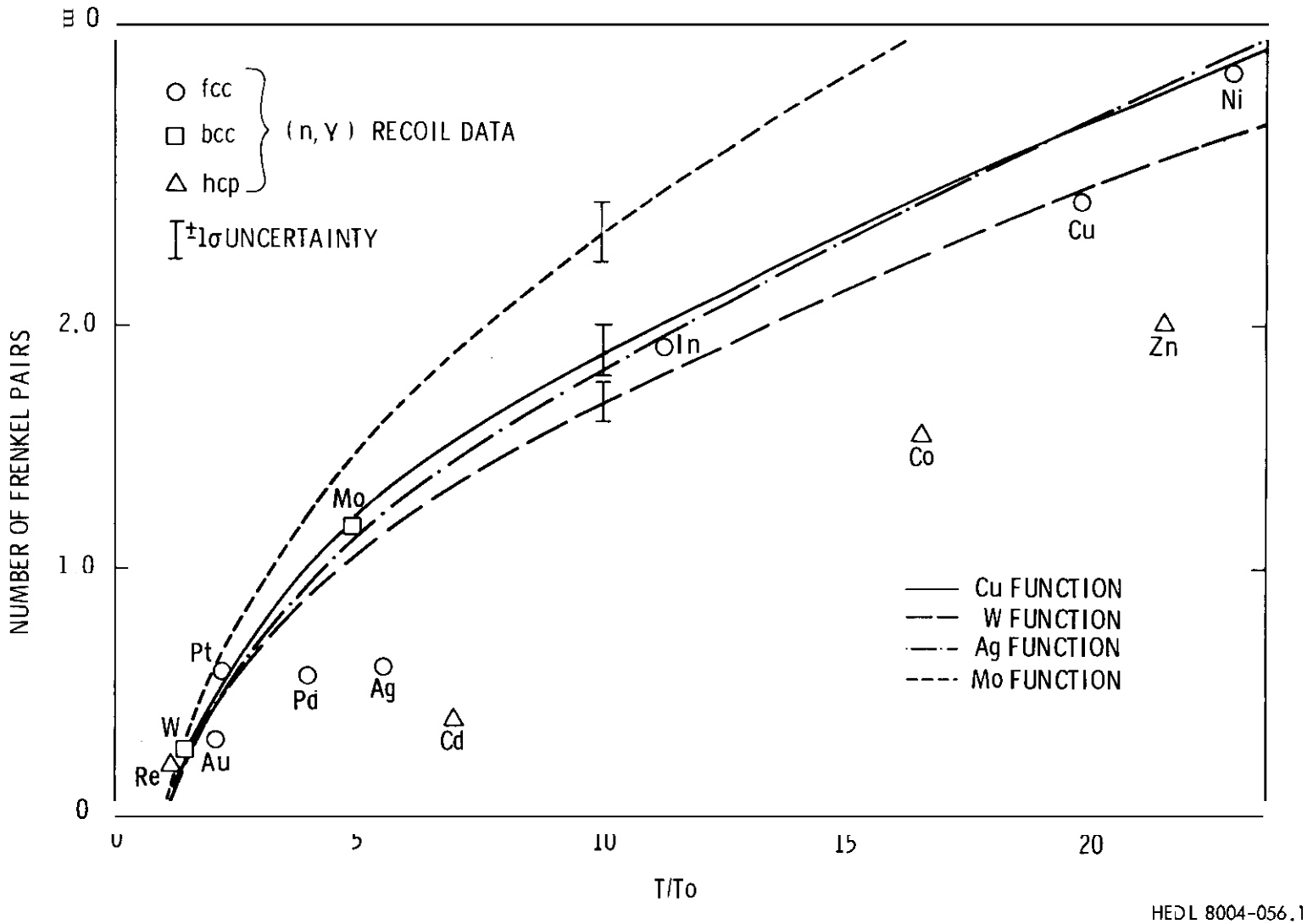

FIGURE 6. (n, γ) Recoil Data and Defect Production Curves Versus Normalized Recoil Energy.

$$B = \frac{d\Delta\rho}{d\phi t} \Big/ \Delta\rho_{FP} \langle \sigma T_D \rangle \qquad (17)$$

where $\frac{d\Delta\rho}{d\phi t}$ is the initial resistivity change per unit fluence, $\Delta\rho_{FP}$ is the specific Frenkel defect resistivity and $\langle \sigma T_D \rangle$ is the neutron spectrum averaged damage energy cross section. For a material with several measurements the average value of B was used. The B coefficients are shown as a function of mass in Figure 7. The ends of the bars show the actual values of B found in this analysis for the four materials Cu, Ag, Mo, and W. The symbols are the values found by Equation (17). The data range from Al with mass 27 to Pt with mass 195. The B coefficient is empirically described by a reciprocal square root of target mass law.

$$B = 10^{-3} (29.3/\sqrt{m} + 0.133) \qquad (18)$$

The standard deviation of the data fit to equation (18) is $\pm$ 10%

4. CONCLUSIONS

In general the K-P function [Equation (11)] of primary recoil damage energy, which shows a linear dependence above 1 keV, gives a good correlation of Frenkel pair production in copper, molybdenum, silver, and tungsten for charged particle and neutron irradiation experiments run at liquid helium temperatures. The coefficients are presented in Table VII.

The logarithmic recoil energy dependence at low energies appears to be adequate for most applications. However, because the threshold surface is anisotropic, the logarithmic function is not as accurate as other methods of treating the threshold region and may be inadequate for describing electron irradiations. Except for Mo, the coefficient of the logarithmic term is 0.65 $\pm$ .05. The coefficient in the K-P function that controls high energy damage is inversely proportional to the square root of target mass for materials ranging from aluminum to platinum.

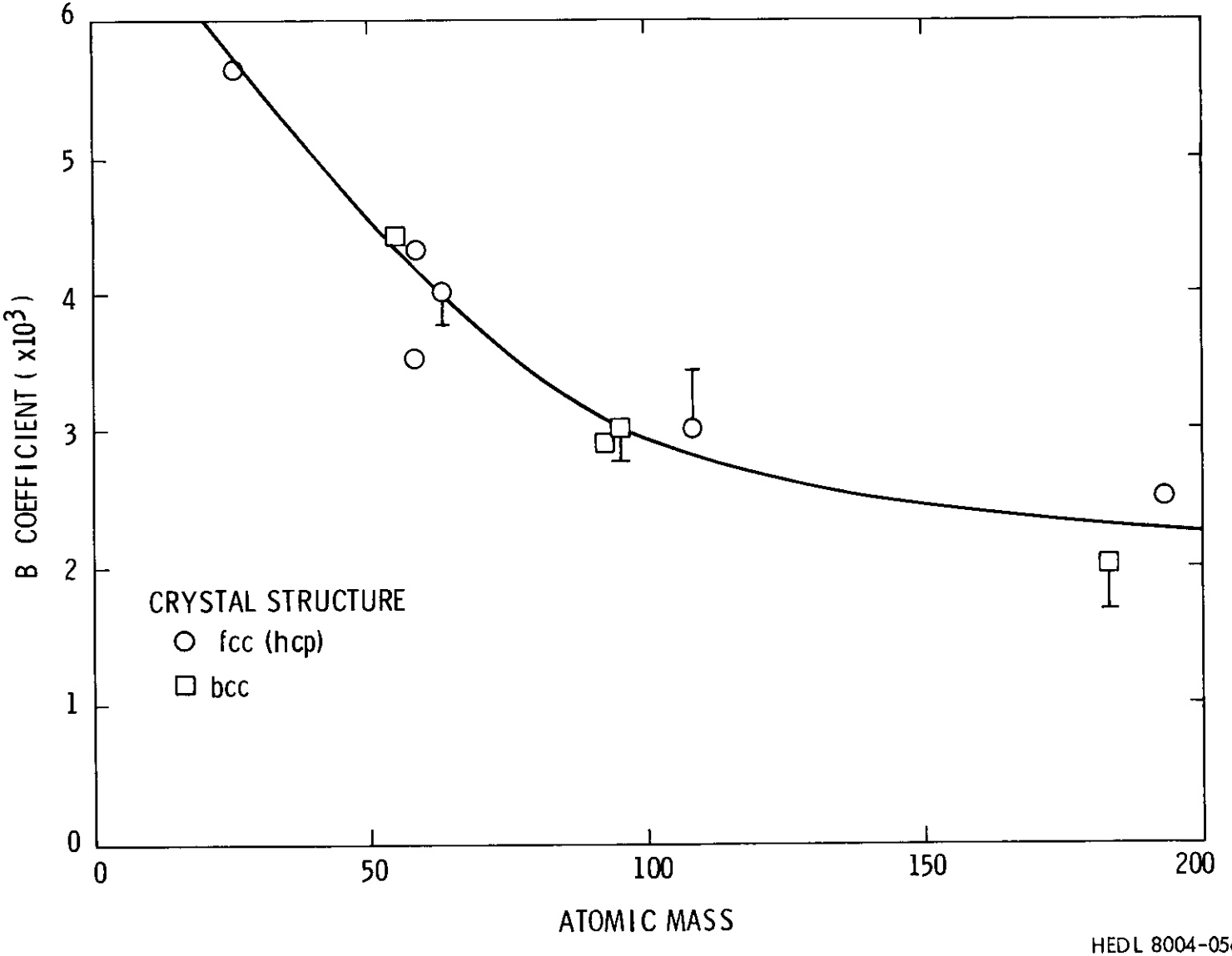

FIGURE 7 Mass Dependence of B Coefficient in K-P Function

The B function [Equation (16)] shows some improvement over the K-P function for silver and tungsten. The B function for silver and tungsten deviate in a positive sense from the K-P function at high energies. This is probably due to a lack of high energy data such as Be(d,n) rather than having any physical significance. For copper and molybdenum no significant differences were found between the K-P and B functions.

The R function [Equation (15)] gave a physically unrealistic fit to the data. This was also due, in part, to a lack of high energy response from such PKA spectra as Be(d,n).

5. Acknowledgements

Thanks are extended to L. R. Greenwood of Argonne National Laboratory for calculating the PKA spectra for the neutron irradiation environments.

VI. REFERENCES

1. R. L. Simons, "Neutron Energy Dependent Damage Functions for Tensile Properties of 20% CW 316 Stainless Steel," Irradiation Effects on the Microstructure and Properties of Metals, ASTM STP 611, American Society for Testing and Materials, 1976, pp. 181-192.

2. R. L. Simons and D. G. Doran, "Application of Damage Functions to CTR Component Fluence Limit Predictions," Proceedings of the International Conference on Radiation Effects and Tritium Technology for Fusion Reactors, CONF-750989, March 1976, Vol. II, pp. 18-37.

3. G. R. Odette, D. R. Doiron, and R. J. Kennerley, "Energy Dependent Neutron Sputtering and Surface Damage Cross Sections," Presented at the International Conference on Surface Effects in Controlled Fusion Devices, San Francisco, Cal. (1977), available as University of California at Santa Barbara Dept. of Chemical Nuclear Engineering Research Report.

4. R. S. Averback, R. Benedek, and K. L. Merkle, "Defect Production in Copper and Silver by Light Energetic Ions," Applied Physics Letters, 30, May 1977, p. 455.

5. R. S. Averback, R. Benedek, and K. L. Merkle, "Efficiency of Defect Production in Cascades," International Conference on the Properties of Atomic Defects in Metals, CONF-761027-14, October 18-22, 1976.

6. R. S. Averback, R. Benedek, and K. L. Merkle, "Correlations Between Ion and Neutron Irradiations: Defect Production and Stage I Recovery," J. Nucl. Mat., 75, (1978), 162-166.

7. K. L. Merkle, R. S. Averback, and R. Benedek, "Energy Dependence of Defect Production is Displacement Cascades of Silver," Phys. Rev. L., 38, February 1977, 424-427.

8. H. H. Anderson and H. Sorenson, "The Energy Dependence of Proton, Deuteron, and Helium-Ion Radiation Damage in Silver," Rad. Effects, 14, (1972), 49-66.

9. M. A. Kirk and L. R. Greenwood, "Determination of the Neutron Flux and Energy Spectrum in the Low-Temperature Fast-Neutron Facility in CP-5, Calculations of Primary-Recoil and Damage Energy Distributions, and Comparisons with Experiment," J. Nucl. Mat. 80 (1979) 159-171.

10. P. G. Lucasson and R. M. Walker, "Energy Dependence of Electron-Induced Atomic Displacements in Al, Ag, Cu, Fe, and Ni," Disc. Faraday Soc., 31 (19610 57-66.

11. R. R. Coltman, Jr., C. E. Klabunde, and J. K. Redman, "Survey of Thermal-Neutron Damage in Pure Metals," Phys. Rev. 156 (1967) 715-734.

REFERENCES (Cont'd)

12. J. O. Schiffgens and R. O. Bourquin, "Computer Simulation of Low Energy Displacement Cascades in a Face Centered Cubic Lattice," J. Nucl. Mat. 69 and 70 (1978) 790-796.

13. P. Jung and G. Lucke, "Damage Production by Fast Electrons in Dilute Alloys of Vanadium, Niobium, and Molybdenum," Rad. Eff. 26 (1975) 99-103.

14. R. R. Coltman, Jr., C. E. Klabunde, and J. K. Redman, "Recovery in Stages I and II of Thermal and Fission Neutron Irradiated Molybdenum," CONF-751006-P1, October 6-10, 1975.

15. H. H. Neely, O. W. Keefer, and A. Sosin, "Electron Irradiation and Recovery of Tungsten," Phys. Stat. Sol., 28 (1968) 675.

16. F. Maury, et al., "Frenkel Pair Creation and Stage I Recovery in W Crystals Irradiated Near Threshold," Rad. Eff. 38 (1978) 53-65.

17. M. W. Guinan, et al., "A comparison of Experimental Defect Production Efficiency in Mo with Computer Simulation in W," DOE/ET-0065/6, Damage Analysis and Fundamental Studies Quarterly Progress Report, July 1979.

18. M. T. Robinson, "The Dependence of Radiation Effects on the Primary Recoil Energy," Proceedings of Conference on Radiation-Induced Voids in Metals, CONF-71-61, April 1972, 397-429.

19. K. B. Winterbon, Peter Sigmund, and J. B. Sanders, "Spatial Distribution of Energy Deposition by Atomic Particles in Elastic Collisions," Kgl. Dan. Vidensk. Selsk. Mat.-Fys. Medd., 37 (1970).

20. J. Lindhard. V. Nielsen, M. Scharff, and P. V. Thomsen, "Range Concepts and Heavy Ion Ranges (Notes on Atomic Collisions)," Kgl. Dan. Vidensk. Selsk. Mat.-Fys. Medd., 33 (1963).

21. V. J. Orphan, et al.." Line and Continuum Gamma-Ray Yields From ThermalNeutron Capture in 75 Elements," GA 10248, Gulf General Atomic, Inc. July 1970.

22. O. S. Oen, "Cross Sections for Atomic Displacements is Solids by Fast Electrons," ORNL-4897, Oak Ridge National Laboratory, August 1973.

23. M. T. Robinson and I. M. Torrens, "Computer Simulation of AtomicDisplacment Cascades in Solids in the Binary-Collison Approximation," Phys. Rev., B9, (15 June 1974), 5008-5024.

24. J. R. Beeler, Jr., "Displacement Spikes in Cubic Metals. I -Iron, Copper, and Tungsten," Phys. Rev., 150, (Oct. 1966), 470-487.

REFERENCES (Cont'd)

25. K. M. Brown," Computer Oriented Methods for Fitting Tabular Data in the Linear and Nonlinear Least Squares Sense," Tech. Report 72-13 Department of Computer Science, University of Minnesota, 1972.

26. K. M. Brown and S. Lin, "A Fortran Package for Multiple Linear Regression," Department of Computer Science, University of Minnesota.

27. P. Lucasson, "The Production of Frenkel Defects in Metals," Proceeding Conference on Fundamental Aspects of Radiation Damage in Metals, CONF-751006-P1, Oct. 1975, 42-65.

APPENDIX A

An average recoil energy was determined for each isotope using the binding energy of the last neutron added to the target nucleus. Thus

$$T_i = Ng\,(E)^2/2mc^2$$

where N_g is the average number of gamnas emitted per reaction from the element as reported by Orphan [21]. It was assumed that each isotope emitted the average number of gamnas measured for the element. E is the binding energy divided by the average number of gammas emitted; mc^2 is the rest mass of a photon. The average recoil energy for the element was the weighted average for all the isotopes.

$$\bar{T} = \frac{\sum_{i=i}^{N} T_i Y_{i\ i} P_i}{\sum_{i=1}^{N} Y_i \sigma_i P_1}$$

where Y_i is the abundance of each isotope, σ_i is the (n,γ) reaction cross section for thermal neutrons, and P_i is the probability that the recoil will produce a displaced atom. The P_i was taken from the paper by Lucasson [27]. The factor P_i was important only in the cases where the isotope recoil energy was near the threshold energy. Without it, some of the element recoil energies were below the threshold values summarized by Lucasson.

Figure A-1 shows the recoil data as a function of reduced recoil energy (i.e., T/T_o). The curves shown are for the fit to the copper data (solid curve) and computer simulation data for tungsten [17] represented by the dashed curve. Comparing this figure with Figure 6 shows some improvement in the alignment of the data with the Cu curve. This may be fortuitous.

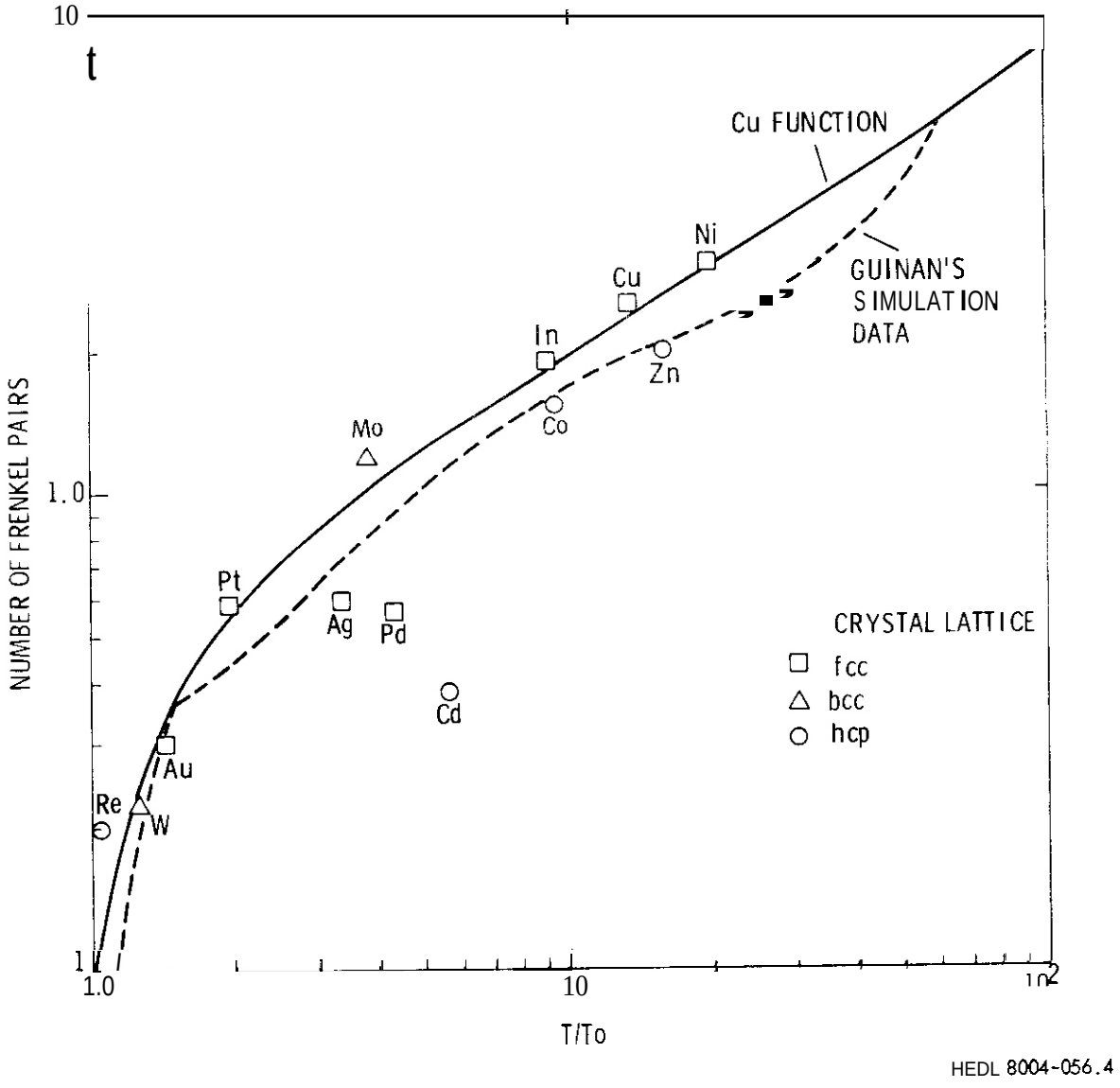

FIGURE A-1. (n,γ) Recoil Data Versus Normalized Recoil Energy.

I. PROGRAM

Title: Irradiation Effects Analysis (AKJ)
Principle Investigator: D. G. Doran
Affiliation: Hanford Engineering Development Laboratory (HEDL)

II. OBJECTIVES

1. Determine defect survivability in copper alloys irradiated at 25°C and the influence of solute additions and neutron fluence.

2. Determine the validity of using TEM and microhardness measurements to study the dependence of survivability on neutron energy and solute additions.

3. Study the nature of microstructural evolution during 14 MeV neutron irradiations for later comparison to fission reactor data.

111. RELEVANT DAFS PROGRAM PLAN TASK/SUBTASK

SUBTASK II.B.3.2 Experimental Characterization of Primary Damage State; Studies of Metals

II.C.6.3 Effects of Damage Rate and Cascade Structure on Microstructure; Low-Energy/High-Energy Neutron Correlations

IV. SUMMARY

Microscopy and microhardness measurements have been performed on pure copper and copper with 5% of either Al, Ni or Mn, all irradiated in RTNS-II at 25°C to fluences as large as 7.5 x 10^{17} n/cm^2. The analysis shows that a substantial fraction of the defects are below the resolution limit of the microscope and account for a large

amount of the hardening that, results from irradiation. It also appears that each cascade event and its subsequent .internal rearrangements may be considered at this flux and fluence to be a separate event, both in time and space. It also appears that some solutes such as Al may lead to substantial differences in clustering of point defects within the cascade and thus affect the subsequent visibility of the clusters. There does not appear to be any substantial effect of any solute studied on the number of total defects surviving the cascade. The fraction of defects surviving the original cascade event appears to be at least 9%.

V. ACCOMPLISHMENTS AND STATUS

A. Microstructural Development for Copper Alloys Irradiated in RTNS-II - H. R. Brager, F. A. Garner, and N. F. Panayotou (HEDL)

1. Introduction

The following alloys were examined by either microscopy or microhardness measurements.

TABLE I

Alloys (atomic %)	TEM Specimens			Microhardness Measurements
	Neutron Fluence		Helium	Fluence Ranqe
	(n/cm^2)	(dpa)	(appm)	(n/cm^2)
Cu	2.7×10^{17}	0.001	0.01	0 to 3.0×10^{17}
Cu + 5% Mn	7.4×10^{17}	0.003	0.04	0 to 7.1×10^{17}
Cu + 5% Ni	7.6×10^{17}	0.003	0.04	0 to 7.3×10^{17}
Cu + 5% Al	7.1×10^{17}	0.003	0.04	0 to 6.8×10^{17}

The experimental techniques employed were standard microhardness and microscopy techniques reported previously.[1,2] In Figure 1, note that the microhardness data for all alloys are linear with the square root of fluence and extrapolate back to the origin. The microstructural data extracted

by transmission microscopy are shown in Table II. Note that for all alloys except Cu + 5%Al there are slightly more than two visible clusters per calculated PKA. There are approximately five visible clusters per PKA in the Al-modified alloy.

Typical micrographs of each alloy examined are also shown in Figure 1, along with an indication of the associated hardness measurement. Figure 2 shows that the size distribution of defects in each of the various alloys is not very different, even though the pure copper specimen was irradiated to a much lower fluence than was the other alloys.

2. Discussion

For fluences approaching 10^{18} n/cm^2 (0.004 dpa) at current peak flux levels of about 2 x 10^{12} n/cm^2 at RTNS-II, the PKA-cascade damage events and their subsequent internal rearrangements can be considered to be essentially isolated events, both in space and time. The evidence supporting this conclusion is that the visible cluster density is linear with fluence, the mean size of these clusters is independent of fluence, and the hardness measurements vary linearly with $(\phi t)^{1/2}$ with a zero incubation period. This conclusion is significant in that no conclusion concerning the magnitude of defect survivability can be made if a significant fraction of the point defects created by each cascade are erased by subsequent cascades.

There are several significant observations to be made concerning the size of the clusters. First, the clusters are significantly larger than predicted by currently available cascade/clustering models. Second, the hardness calculations indicate that the total hardening is independent of the alloy while the visible cluster density is significantly larger in the copper-aluminum alloy. This suggests that a substantial fraction of the defects are below the resolution limit of the microscope.

TABLE II

MICROSCOPY DATA - RTNS-II COPPER BINARY SERIES

Alloy	ϕt Neutron Fluence (10^{17} n/cm^2)	$\bar{d}$ Cluster Diameter (nm)	ρ Cluster Conc. (10^{17}/cm^3)	($\rho/\phi t$) Cluster Conc./ Unit ϕt	N Total Defect Density (10^{19} defects/cm^3)	($N/\phi t$) Defect Density/ Unit ϕt	PKA Conc. (10^{17}/cm^3)	ρ/PKA
Cu	2.7	2.6	1.3	0.48	1.3	49	0.57	2.3
Cu + 5% Mn	7.4	2.7	3.4	0.46	3.7	50	1.57	2.2
Cu + 5% Ni	7.6	2.3	3.6	0.47	3.5	46	1.61	2.2
Cu + 5% Al	7.1	2.0	[illegible]	[illegible]	[illegible]	83	1.51	5.1

A lower-bound estimate of the number of invisible clusters can be made using the following logic. If the copper and copper plus 5% aluminum alloys exhibit identical hardening then the density (p) and diameter (d) of the invisible (i) and visible (v) clusters should obey the following relationship.

COPPER COPPER + 5% ALUMINUM

$$\rho_v^{Cu}\, d_v^{Cu} + \rho_i^{Cu}\, d_i^{Cu} = \rho_v^{Al}\, d_v^{Al} + \rho_i^{Al}\, d_i^{Al} \qquad (1)$$

Rearranging this expression leads to

$$1 + \frac{\rho_i^{cu}\, d_i^{cu}}{\rho_v^{cu}\, d_v^{cu}} = \frac{\rho_v^{Al}\, d_v^{Al}}{\rho_v^{cu}\, d_v^{cu}} + \frac{\rho_i^{Al}\, d_i^{Al}}{\rho_V^{cu}\, d_v^{Cu}} \qquad (2)$$

where the first term on the right hand side is a known quantity and therefore

$$\frac{\rho_i^{cu}\, d_i^{cu}}{\rho_v^{cu}\, d_v^{Cu}} = 0.84 + \frac{\rho_i^{Al}\, d_i^{Al}}{\rho_v^{cu}\, d_v^{Cu}} \qquad (3)$$

The above expression defines the lower limit of the hardening due to the invisible cluster population in copper if one assume that no clusters are invisible in the 5% aluminum alloy. Since the resolution limit of the microscope in these studies is ~1.0 nm it is not unreasonable to assume that the invisible clusters lie in the range $0.5 \leq d_i^{Cu} \leq 1.0$ nm where a typical atomic diameter is ~0.2 nm. Since the mean visible cluster diameter is about 2.5 nm, therefore

$$\frac{d_i^{Cu}}{d_v^{Cu}} \sim \frac{1}{3} \qquad (4)$$

Using this relationship and assuming that the clusters are circular loops, the following quantities can be calculated.

Fraction of hardening due to unresolved defect clusters

$$\frac{\rho_i^{cu}\, d_i^{cu}}{\rho_v^{cu}\, d_v^{cu} + \rho_i^{cu}\, d_i^{cu}} \gtrsim 46\% \qquad (5)$$

Fraction of unresolved defect clusters:

$$\frac{\rho_i^{Cu}}{\rho_v^{Cu} + \rho_i^{cu}} \gtrsim 72\% \qquad (6)$$

Fraction of defects in the form of unresolved clusters

$$\frac{\rho_i^{Cu} \left(d_i^{Cu}\right)^2}{\rho_v^{Cu} \left(d_v^{Cu}\right)^2 + \rho_i^{Cu} \left(d_i^{Cu}\right)^2} \gtrsim 22\% \qquad (7)$$

The total defects in the visible clusters at 7.5 x 10^{17} n/cm^2 is

$$N_v \sim \frac{\pi d^2 \rho}{4} \sim 3.6 \times 10^{19} \text{ defects/cm}^3, \qquad (8)$$

which means that the visible and invisible clusters can account for at least 4.4 x 10^{19} defects/cm^2.

Assuming 8.42 x 10^{22} atoms/cm^3, a displacement cross section of 3690 barns, and two defects per displacement leads to the conclusion that 4.7 x 10^{20} defects/cm^3 were originally created. At least 9% now survive. (Remember that 9% is a lower bound estimate in that some clusters in the 5% aluminum alloy must also be invisible.

It is important to notice that the above analysis assumes that the solute hardening and defect cluster hardening are directly additive. As shown in Table III, the differences in measured hardness of the alloys in the unirradiated condition are qualitatively consistent with that expected on the basis of an increase or a decrease in the lattice parameter (Figure 3). Quantitatively, the concentration of the solute atoms ($\sim$4 x 10^{21} atoms/cm^3) is about 100 times larger than that estimated for the defect clusters. Since the magnitude of solute hardening is comparable to or less than that of the defect cluster hardening, the hardening per solute atom would be about two orders of magnitude smaller than that due to defect clusters and could be considered separable and additive.

TABLE III

ROOM TEMPERATURE HARDNESS OF UNIRRADIATED ALLOYS

Alloy	Hardness (DPH)	Solute hardening (DPH)
pure copper	56	0
copper + 5% nickel	58	2
copper + 5% aluminum	66	10
copper + 5% manganese	73	17

The data presented in this report also appear to indicate that solutes such as nickel and manganese have no significant effect on the damage production and recombination process in copper. This is not surprising in that the atomic weight of each element is not too different. The atomic weight is an important determinant of the amount of energy transferredfromthe neutron. The difference in atomic weight of solute and solvent atoms also affects atomic replacement sequences and energy propagation in the lattice. The magnitude and sign of the difference in lattice parameter (See Figure 3) does not appear to be a decisive factor either.

The aluminum atom has only 43$ of the weight of the average copper atom however. This means that per collision the aluminum atom will receive a greater share of the neutrons energy. There will also be a ~15% inefficiency of energy transfer between an energetic aluminum atom and the copper atoms which compose 95% of the alloy however. These factors may have important consequences in the spatial distrubution of damage. This possibility will be treated in more depth in the next reporting period. For the present however, it appears that solutes such as aluminum lead to substantial differences in the in-cascade clustering of point defects and therefore affect the subsequent visibility of such clusters. It is also expected that there may exist substantial interactions between vacancies and elements such a silicon or aluminum. These interactions would thus affect the defect clustering and recombination processes.

2. H. R. Brager, H. L. Heinisch and N. F. Panayotou, "Microstructural Development in Copper Irradiated in RTNS-II," 9th OAFS Quarterly Technical Progress Report (May 1980) DOE/ER-0046/1, p. 76.

3. M. Hansen, "Constitution of Binary Alloys", McGraw-Hill, 1958, pg. 597.

VII. FUTURE WORK

A similar analysis will proceed on the nickel-5% solute series irradiated in RTNS-II to 7.5 x 10^{17} n/cm^2 at 25°C. The considerations of solute size, weight, and interaction with point defects will also be treated in depth.

3. Conclusions

1. At least 72% of the clusters produced by 14 MeV neutrons in the pure copper and in 5%-nickel and 5%-manganese copper alloys are smaller than the resolution limit of the microscope ($\sim$1 nm). It also means that TEM, used alone, is an inadequate tool to study the survivability of point defects.

2. Providing that assumptions can be made on cluster size distributions, microhardness measurements are an excellent tool to measure the relative amounts of defects, both visible and invisible. A better approach is the coupled use of TEM and microhardness measurements.

3. A minimum of 9% of the calculated displacements survive the original defect cascade event.

4. Additions of Ni and Mn have no observable effect on the damage production and recombination process in copper. The addition of Al has a strong effect on defect size distributions and possible defect survivability. None of these elements affect the radiation-induced change in microhardness.

5. Comparison of the results with other irradiation data suggest that in-cascade defect-solute interactions are important in defect survivability.

VI. REFERENCES

1. N. F. Panayotou et al, "RTNS-II Irradiation Program Status," (a) DAFS Quarterly Progress Report, DOE/ET-0065/5 (January-March 1979), p. 112, (b) DAFS Quarterly, DOE/ET-0065/6 (April-June 1979), p. 84, (c) DAFS Quarterly, DOE/ET-0065/7 (July-October 1979), p. 65, (d) DAFS Quarterly, DOE/ET-0065/8 (October-December 1979), p. 113.

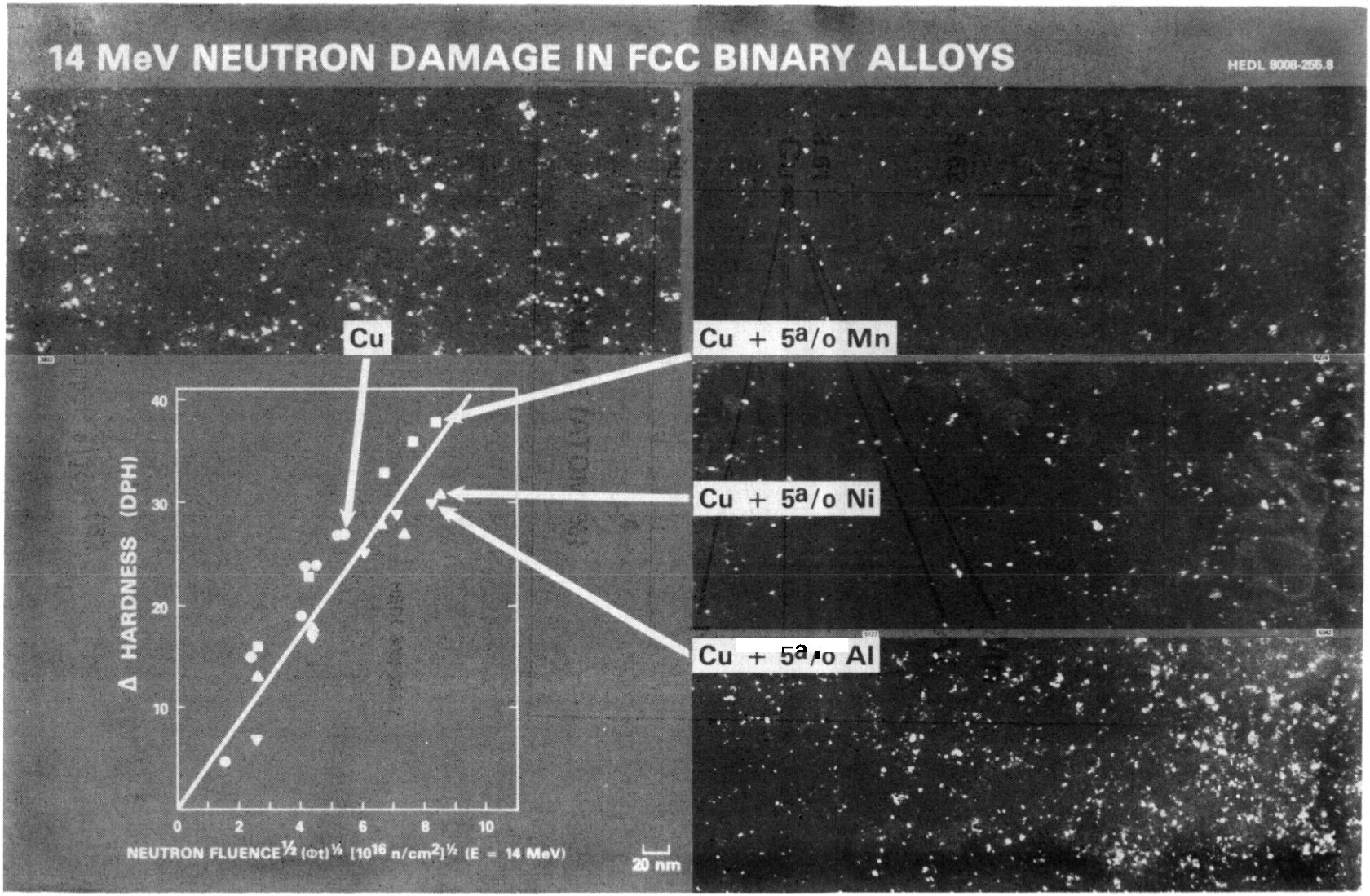

Figure 1. Microhardness and microstructure of copper and copper alloys irradiated in RTNS-II at 25°C with 14-MeV neutrons.

DEFECT CLUSTER SIZE DISTRIBUTION

COPPER BASED ALLOY; 25°C IRRADIATION BY 14 MeV NEUTRONS

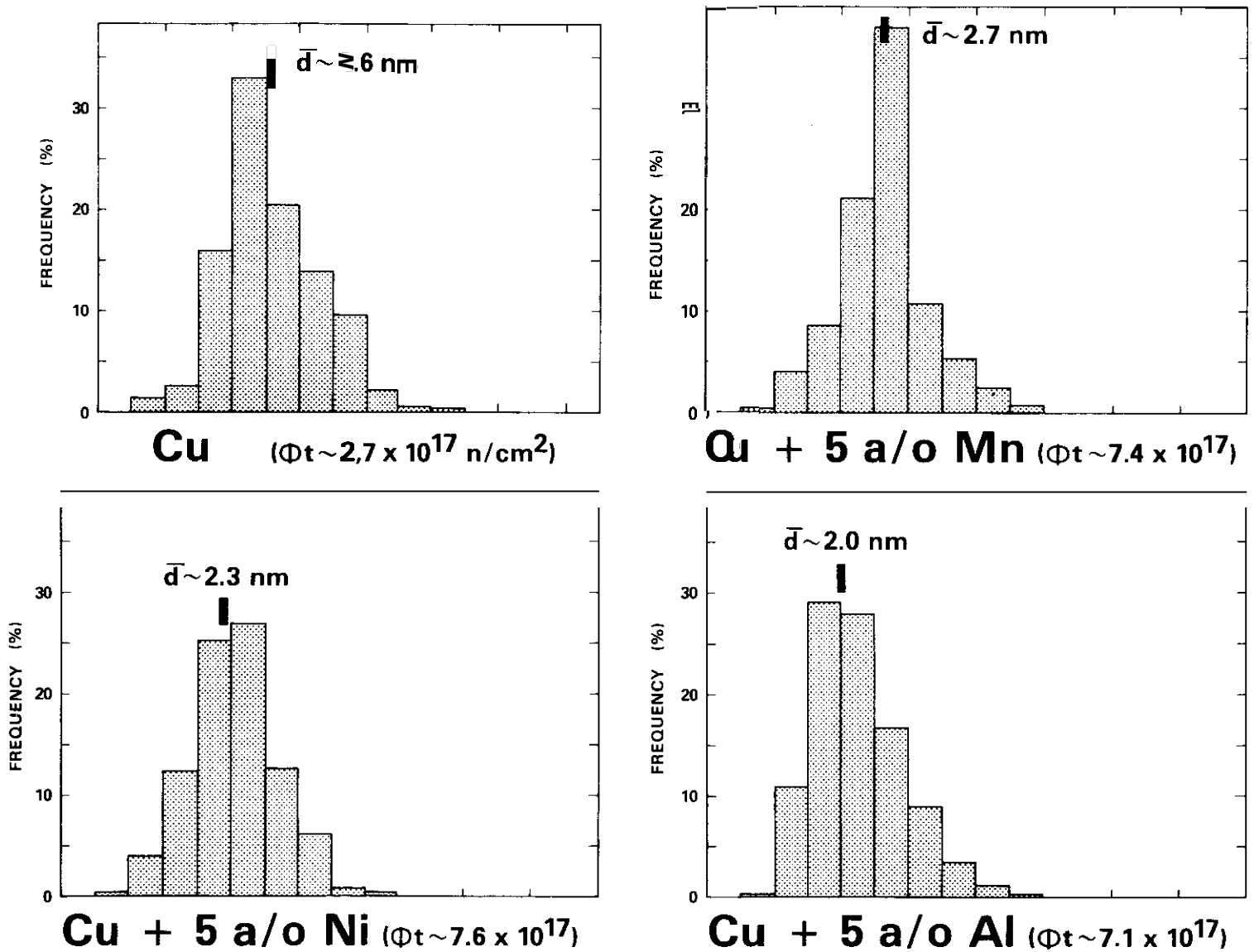

HEDL 8008-255.13

Figure 2. The size distribution of visible defect clusters formed in the copper and copper alloys. The mean size of the clusters are indicated.

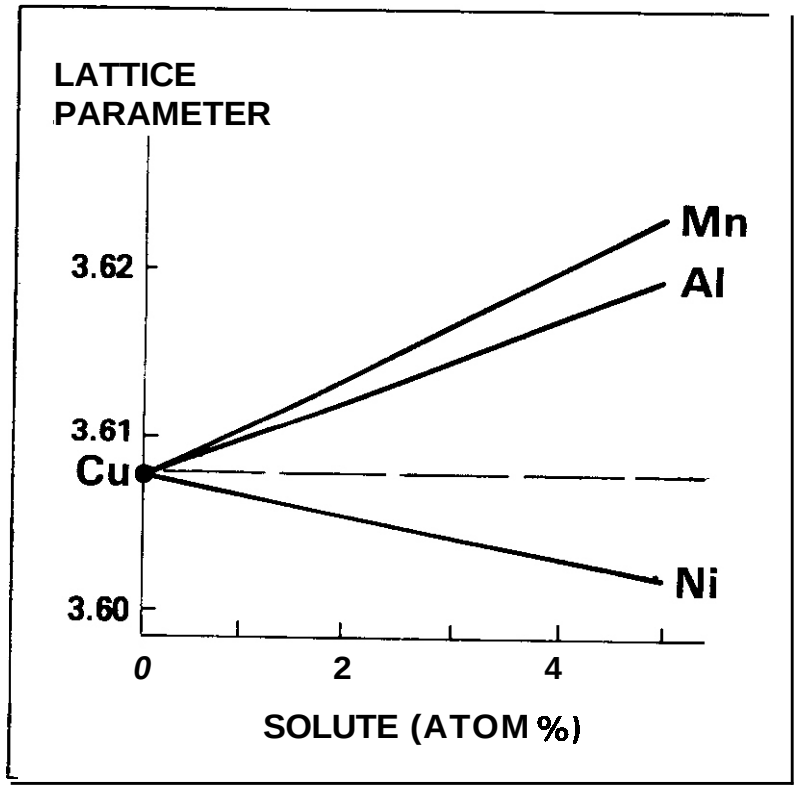

HEDL 8009-255.2

Figure 3. Lattice parameter of copper alloys(3).

CHAPTER 3

FUNDAMENTAL MECHANICAL BEHAVIOR

I. PROGRAM

Title: Irradiation Effects Analysis (AKJ)
Principal Investigator: D. G. Doran
Affiliation: Hanford Engineering Development Laboratory (HEDL)

11. OBJECTIVE

The objective of this effort is to estimate the effects of irradiation pulsing on irradiation creep, and to modify correlations developed from fast breeder reactor data for fusion reactor applications.

III. RELEVANT OAFS PROGRAM PLAN TASK/SUBTASK

TASK II.C.5 Effects of Cycling on Microstructure
TASK II.C.14 Models of Flow and Fracture Under Irradiation

IV. SUMMARY

For the temperatures and pulsing conditions anticipated in the Engineering Test Facility it has been found that both the stress-induced preferential absorption (SIPA) and climb-glide creep mechanisms are essentially unaffected by the pulsing of the irradiation. It is therefore not necessary to add corrections based on pulsing to creep correlations developed from breeder reactor data.

V. ACCOMPLISHMENTS AND STATUS

A. Effect of Irradiation Pulsing on the SIPA Creep Mechanism -

H. Gurol (UCSB) and F. A. Garner (HEDL)

1. Introduction

The design of projected fusion reactors relies strongly on accurate predictions of dimensional changes in structural materials due to irradiation creep and swelling. Since fusion reactors are anticipated to run in non-steady state modes, there is a need for studying the effects of pulsing on these processes. Swelling and the climb-glide model of creep have been addressed earlier.[1,2] Under the range of scenarios of microstructural evolution applicable to the environment of the Engineering Test Facility (ETF), enhancement of the climb-glide process was found to be negligible. There may be a two to three-fold increase in the creep rate at low fluences where the obstacles to climb are rather small.

There are basically two widely accepted models of irradiation creep however: not only the climb-controlled glide mechanism[3,4,5] but also the stress-induced preferential absorption of the point defects (SIPA).[6,7,8] There is considerable controversy over which creep mechanism is the dominant one in a given set of conditions. In general, both the climb-glide and SIPA mechanism are probably operating simultaneously. The SIPA creep may be dominant and operating alone only under certain conditions, such as in solution-annealed material at low neutron fluences.

Simonen and Hendrick[9] have measured the irradiation creep of deuteron-irradiated nickel subject to repeated sequences of 1000 seconds irradiation, followed by 100 seconds of annealing. They measured a creep rate under pulsing which is approximately three times the creep rate obtained by steady irradiation, and conclude that the climb-glide process is the dominant creep mechanism under these circumstances. Recently, Gurol and Ghoniem[2] have investigated theoretically the effects of pulsing on the climb-glide creep mechanism. Depending on the material, temperature and pulsing conditions, they find that pulsing can enhance the climb-glide creep by as much as a factor of two or three. Greater enhancements were found for conditions typical of projected Inertial Confinement Fusion Reactors (ICFR).

The purpose of this effort is to investigate the response of the SIPA creep mechanism when the irradiation is pulsed under proposed ETF conditions (30 - 50 seconds on-time, 10 - 15 seconds off-time, 50 - 300°C). Specifically, we shall confine our analysis to calculating the ratio of the pulsed to the steady irradiation creep rate. The rate theory formulation previously employed is used throughout.[1,2]

2. Theory

The SIPA creep rate can be written as[10]

$$\dot{\varepsilon} = (N_\ell \zeta_\ell + \rho_d \zeta_d) \left(\frac{\sigma}{G}\right) \frac{1}{\bar{Z}_v} D_i C_i(t), \qquad (1)$$

where σ is the stress, G the shear modulus, N_ℓ and ρ_d the dislocation loop and edge dislocation densities, and $\bar{Z}_v$ is the average vacancy sink efficiency. ζ_ℓ and ζ_d are the bias contributions of the loops and dislocations, respectively, and of course D_i and C_i are the interstitial diffusion coefficient and concentration. The quantity of interest for the purpose of studying the SIPA mechanism under pulsing is the time dependence of $C_i(t)$. Any differences between the pulsed and steady irradiation creep rates must be due to the differences in $C_i(t)$. It is assumed here that the pulsing itself does not produce any changes in the normally evolving microstructure. This should be a valid assumption under low frequency pulsing, but is expected to break down for example under ICFR conditions.[11]

It has been previously found[2] that for a given microstructure the time-dependence of the point defect concentrations is critically sensitive to the relative magnitude of the mean vacancy diffusion time to sinks τ_v and the duration of the pulse on-time T_{on}. We now consider the following cases, divided with respect to the point-defect kinetics.

2.1 Sink-Dominant Case

The sink-dominant case is characterized by a microstructure and temperature where direct recombination of vacancies and interstitials is negligible.

This is satisfied when

$$\frac{1}{\alpha P} > \tau_i \tau_v \ , \tag{2}$$

where α is the recombination coefficient, P is the average damage rate and $\tau_{i,v}$ is the point-defect diffusion time to sinks. The interstitials reach the steady-state concentration almost instantaneously when the pulse is turned on, and rapidly decline to thermal equilibrium values when the pulse is turned off. Therefore, after adjusting the damage rate P for dose equivalence, the SIPA creep rate will be identical for both pulsed and steady irrradiation. Using the following values, characteristic of stainless steels, $E_v^m = 1.3eV$, $E_i^m = 0.2eV$, $D_i^o = 0.001\ cm^2/s$, $D_v^o = 0.5\ cm^2/s$, $(\frac{\alpha}{D_i}) = 10^{16}$, $P = 10^{-6}$ dpa/s, the sink-dominant case will fall in the temperature range $T \geq 300°C$ for total sink densities between 10^{11} and $10^{12}/cm^2$.

2.2 Transient Interstitial Behavior for All Pulses: τ_v > Irradiation Time

The vacancy and interstitial concentrations will always be in a transient (for both pulsed and steady irradiation), for values of τ_v greater than the irradiation time. Using the above parameters, for sink densities on the order of $10^{11}/cm^2$, this corresponds to temperatures less than approximately 100°C. The interstitial concentration for the kth pulse is given by[2]

$$\begin{aligned} C_i^{(k)}(t) &= \left(\frac{P}{\alpha h}\right)_1^{1/2} [t-(k-1)(T_f-T_{on})]^{-1/2} \ , \text{ on-time} \\ C_i^{(k)}(t) &= 0 \ , \text{ off-time} \end{aligned} \tag{3}$$

where T_f is the period of the pulsing. Under steady irradiation, the interstitials will exhibit the same $t^{-1/2}$ dependence as under pulsed irradiation. Hence, one finds that SIPA creep is virtually unaffected by pulsing for very large values of τ_v.

2.3 Steady-State Achieved During the On-Time: $\tau_v < T_{on}$

For sink densities on the order of $10^{11}/cm^2$, and temperatures $T \gtrsim 200°C$, one finds that $\tau_v \lesssim 50$ seconds. Therefore, under these conditions the point-defect concentrations will be able to reach their steady-state values in one pulse. The behavior of the interstitial concentration will be repeated in every pulse. However, during parts of the irradiation pulse, the interstitials will be in a transient. The interstitial concentration for the kth pulse is given by[2]

$$C_i^{(k)}(t) = \left(\frac{P}{\alpha\lambda_i\tau_v'}\right)^{1/2}\left[t-(k-1)(T_f-t^*)\right]^{-1/2} \quad , (k-1)T_f < t < (k-1)T_f + \tau_v'$$

$$C_i^{(k)}(t) = C_i^{ss} \quad , (k-1)T_f + \tau_v' < t < (k-1)T_f + T_{on} \qquad (4)$$

$$C_i^{(k)}(t) = 0 \quad , \text{off-time}$$

where $t^* \equiv \tau_v \exp[-2\lambda_v(T_f-T_{on})]$,

and $\tau_v' \equiv \tau_v - t^*$

Using equations (4) and (1), the ratio of the creep strain per pulse for pulsed irradiation to steady irradiation can be evaluated for the SIPA mechanism. The result is:

$$\frac{\Delta\varepsilon_p}{\Delta\varepsilon^{ss}} = \frac{2\left(\frac{P}{\alpha\lambda_i}\right)^{1/2}\left(\tau_v^{1/2}-t^{*1/2}\right) + C_i^{ss}\left(T_{on}-\tau_v'\right)}{C_i'^{ss}\,T_f} \qquad (5)$$

where $C_i'^{ss}$ is the steady-state concentration using the dose-equivalent damage rate $P' = P\left(\frac{T_{on}}{T_f}\right)$. The greatest difference between pulsed and steady

irradiation can be expected for $\tau_v = T_{on}$, for which equation (5) becomes

$$\frac{\Delta\varepsilon_p}{\Delta\varepsilon_{ss}} \approx \left(\frac{T_{on}}{T_f}\right)^{1/2} \left[2\left(1-\exp\left[-\frac{T_f-T_{on}}{T_{on}}\right]\right) + \exp\left[-2\,\frac{T_f-T_{on}}{T_{on}}\right]\right] \qquad (6)$$

We find that this ratio is always close to unity. For example for T_{on} = 50 seconds, T_f = 65 seconds, the ratio is 0.97. For T_{on} = 1000 seconds, T_f = 1100 seconds (which corresponds to the pulsing conditions of Simonen and Hendrick's experiment[9]) it is 0.95. This means that the SIPA mechanism cannot give rise to the enhancement observed in their experiment.

For intermediate τ_v values (temperature between 100°C and 200°C), the interstitial concentration will exhibit transient behavior initially (as in section 2.2). Thereafter one finds a repeatable interstitial profile for every pulse (as in this section). Since the interstitial behavior will have the elements of both cases, no enhancement will occur over steady irradiation.

3. Conclusions

For the temperatures and pulsing conditions appropriate to the environment anticipated in the ETF, it has been found that the SIPA creep mechanism is virtually unaffected by pulsing. Since a similar conclusion was reached for the climb-glide mechanism under most conditions it is not anticipated that the pulsed nature of the irradiation in ETF will lead to substantial changes in the irradiation creep behavior.

VI. REFERENCES

1. N. M. Ghoniem and H. Gurol, "An Analytical Approach to Void Growth In Inertial Confinement Fusion Reactor First Wall:' University of California Engineering Report UCLA/ENG/7984 (1979).

2. H. Gurol and N. M. Ghoniem, "Irradiation Creep by the Climb--Controlled Glide Mechanism in Pulsed Fusion Reactors," Rad. Eff. (1980), in press.

3. W. J. Duffin and F. A. Nichols, J. Nucl. Mat. 45, 302 (1972/73).

4. F. A. Nichols, J. Nucl. Mat. 84, 207 (1979).

5. S. R. MacEwen and V. Fidleris, Phil. Mag. 31, 1149 (1975).

6. P. T. Heald and M. V. Speight, Phil. Mag. 29, 1075 (1974)

7. R. Bullough and J. R. Willis, Phil. Mag. 31, 855 (1975).

8. W. G. Wolfer and M. Ashkin, J. Appl. Phys. 46, 547 (1975).

9. E. P. Simeon and P. L. Hendrick, J. Nucl. Mat. 85 & 86, 873 (1979)

10. W. G. Wolfer, L. K. Mansur and J. A. Sprague, "Theory of Swelling and Irradiation Creep," Proc. of Conf. on Radiation Effects in Breeder Reactor Structural Materials, June 19 - 23, 1977, Scottsdale, Arizona, Eds. M. L. Bleiberg and J. W. Bennett, p. 841.

11. N. M. Ghoniem, J. Nucl. Mat. 89, 359 (1980).

VII. FUTURE WORK

This analysis has proceeded on the assumption that the rate theory approach yields an adequate description of the time-dependent point defect concentrations. As sensed by the individual dislocation however, the point defect concentrations exhibit considerable variation in time and space, resulting from the discrete nature of the displacement cascade. There exists a possibility that the cascade-induced variability will lead to a substantial increase in the amount of climb experienced by each dislocation over its obstacles. This possibility will be examined in the next reporting period.

I. PROGRAM

Title: Effects of Irradiation on Fusion Reactor Materials
Principal Investigators: F. V. Nolfi, Jr. and A. P. L. Turner
Affiliation: Argonne National Laboratory

11. OBJECTIVE

The objective of this work is to establish the effects of flux, stress, alloying elements and solute redistribution on the creep-deformation behavior of various classes of materials during light-ion irradiation.

III. RELEVANT OAFS PROGRAM PLAN/SUBTASK

SUBTASK II.C.ll.l Light Particle Irradiations

IV. SUMMARY

Experiments were performed on Ni-4 at. % Si to examine stress dependence and flux dependence of the irradiation creep in this model alloy. The stress dependence of the irradiation creep rate showed a transition from linear to stronger than linear with increasing stress. A linear dependence of creep-rate on damage rate was observed in the linear stress dependence regime. The irradiation creep of this alloy appears to be controlled by the SIPA-driven climb and by the dislocation glide enabled by the SIPA-climb at low and high stresses, respectively.

V. ACCOMPLISHMENTS AND STATUS

A. Irradiation Creep of Hi-4 % Si -- J. Nagakawa and V. K. Sethi

In recent progress reports it has been shown that the presence of solute atoms causes considerable irradiation hardening in Ni-4 at. % Si

alloy (1,2). It was concluded that this hardening effect is associated with radiation-induced segregation (RIS) and concomitant precipitation/decoration of Frank loops (2). The irradiation hardening saturates nearly at a low dose (∿ 0.01 dpa) and further irradiation reduces the thermal creep rate only slightly, suggesting an early formation of a rather stable microstructure in the alloy. In-situ HVEM irradiation study indicates that even after the irradiation to ∿ 0.15 dpa only a fraction of solute atoms are precipitated on Frank loops and a substantial fraction are still in the matrix (2).

This report presents stress dependence and damage rate dependence or irradiation creep in Ni-4 at. % Si alloy after saturation of irradiation hardening, i.e. after a pseudo-stable microstructure has been attained. In order to eliminate sample to sample variations, all experiments on the stress and damage rate dependence were performed using the same specimen (Ni-4Si-9), which had been irradiated previously to 0.031 dpa mainly for the measurements of postirradiation creep rate as a function of irradiation dose (Fig. 6 in ref. 2). Thermal creep data obtained with this specimen confirmed the stress exponent of 3 for the postirradiation creep rate previously reported for another specimen (Ni-4Si-3) at a higher dose (0.075 dpa) (1) as shown in Fig. 1. The agreement of the thermal creep data for the two samples demonstrates the reproducibility of the experiment. All experiments were performed with 21 MeV deuterons and at a specimen temperature of 350°C.

Stress Dependence

Figure 2 shows irradiation creep curves of Ni-4 % Si at various stresses and a damage rate of 1.3×10^{-6} dpa $\cdot s^{-1}$. The irradiation creep strain (irradiation-enhanced component) was evaluated by subtracting the thermal creep stain, estimated from the postirradiation creep rate (at ∿ 15 hours after each irradiation), from the total creep strain during the irradiation. Strain data were aquired every minute by a digital data logger newly installed to the torsional creep system. The irradia-

tion creep rates indicated in Fig. 2 were obtained by fitting a smooth curve through the digital data (c.f. data points shown at the top) by a least square method. The stress indicated for each curve is the maximum shear stress.

The stress dependence of the irradiation creep rate (irradiation-enhanced component) is shown in Fig. 3. The irradiation creep rate data for 1.3 x 10^{-6} dpa . s^{-1} shown in Fig. 2 and other data for 2.0 x 10^{-6} dpa · s^{-1} and 0.5 x 10^{-6} dpa . s^{-1} are summarized in this figure. The irradiation creep rates for 1.3 x 10^{-6} dpa . s^{-1} gave a linear stress dependence below ∿ 50 MPa, while above ∿ 70 MPa the creep-rate showed a stronger dependence on stress. The stress exponent in the high stress regime appears to increase smoothly to 3 or higher with increasing stress. Although the number of data points for other damage rates is not adequate to make a conclusive statement, the trends in Fig. 3 appear similar. The region with the linear dependence appears to extend to a higher stress with increasing damage rate, but again the data are insufficient to state this conclusively.

A change in stress exponent similar to the present result has been reported for cold-worked Type 321 (3) and 316 (4) stainless steel. Schwaiger, Jung and Ullmaier (4) argued that the transition from linear to quadratic in the cold-worked Type 316 stainless steel could be explained by Mansur's model (5). According to this model the linear stress dependence at low stresses is caused by the stress-induced preferential absorption (SIPA) of point defects (PA - creep) and the quadratic dependence at higher stresses results from the climb-enabled glide (bow-out) of network dislocations due to SIPA (PAG - creep). Higher dislocation density enhances PA-creep more than PAG-creep and shifts the transition to a higher stress because of the different dependences on the dislocation density (5).

Although the Ni-4 % Si specimen in the present investigation was not cold-worked, the very high density of decorated Frank loops suppress

the glide contribution to the irradiation creep and consequently the SIPA-driven climb overwhelms the climb-glide contribution at low stresses. Frank loops may contribute to the irradiation creep by the SIPA-driven climb (growth) in addition to the climb of other dislocations introduced during the thermal creep prior to the irradiation (usually for $\sim$ 60 hours). At higher stresses the climb-enabled glide contribution appears to become dominant with a greater than linear stress dependence as suggested by Mansur (5). The observed stress dependence did not remain quadratic and the stress exponent appeared to increase to three or higher with increasing stress. More sophisticated climb-enabled glide medels based on the high temperature thermal creep mechanisms are expected to give a greater than quadratic stress dependence.

Damage Rate Dependence

Figure 4 shows the damage rate dependence of the irradiation creep rate (irradiation-enhanced component) for Ni-4 at. % Si irradiated with 21 MeV deuterons at 350°C under the maximum shear stress of 34.5 MPa. This figure clearly shows that the creep component due to irradiation has a linear dependence on the damage rate. The irradiation at 2.0 x 10^{-6} dpa . s^{-1} appears to show a greater than linear flux dependence. However, this may be due to the fact that strong focusing was required for the cyclotron beam to obtain the high damage rate. This increases the uncertainty of measurement of the beam intensity on the sample. It is quite possible that the damage rate of 2.0 x 10^{-6} dpa • s^{-1} is an underestimate for this particular datum.

Figure 5 shows the damage rate dependence of the irradiation creep at a higher stress (103 MPa) and at a lower stress (23 MPa) in addition to the data shown in Fig. 4 on a logarithmic scale. At the higher stress, which is above the linear stress dependence range, the damage rate dependence appears to be weaker than linear (exponent $\sim$ 2/3). However, confirmation of a 2/3 dependence in the high stress regime will require more experiments.

Effect of Solutes

Solute atoms in the matrix are expected to affect the irradiation creep by the following mechanisms: i) Point defect trapping at solute atoms reduces the free interstitial concentration by an enhanced vacancy-interstitial recombination (6,7). ii) If the solute atom is undersized so as to form mobile interstitial-solute complex, the bias factor would be altered owing to a reduced size effect contribution and to a change in modulus of the interstitial dumbbell (6). iii) Composition gradients or precipitation at defect sinks through RIS may modify the bias factor for defects (7). In general solute atoms are expected to reduce the irradiation creep.

It is difficult to make a clear comparison of the irradiation creep behavior between pure Ni and Ni-4 % Si because of the difference in microstructure and of the uncertainty of irradiation creep mechanism in pure Ni. For a crude approximation one might compare the irradiation creep of the two materials at the stresses which give the same post-irradiation creep rate. This condition can be attained at 20 MPa for pure Ni and at 34.5 Mpa for Ni-4 % Si as shown in Fig. 1. At these stresses the alloy and, probably, the pure Ni are the lienar stress dependence range, and the simple SIPA mechanism may be operational in both materials. The irradiation creep rates at 2×10^{-6} dpa $\cdot s^{-1}$ are 3.7×10^{-9} s^{-1} and 2.2×10^{-9} s^{-1} for pure Ni (ref. 1) and Ni-4 % Si (Fig. 5), respectively. Solute atoms seem to reduce the irradiation creep rate of Ni by about 40 % which appears to be a reasonable amount for any combination of the mechanisms mentioned above.

VI. REFERENCES

1. V. K. Sethi, R. Scholtz and F. V. Nolfi, Jr., DAFS Quarterly Progress Report for Period Ending June 30, 1979, p. 226.

2. V. K. Sethi, R. Scholtz. F. V. Nolfi. Jr. and A. P. L. Turner, DAFS Quarterly Progress-Report for Period Ending December 31, 1979, p. 117.

3. J. A. Hudson, R. S. Nelson and R. J. McElroy, J. Nucl. Mat., 65, 279 (1977).

4. Chr. Schwaiger, P. Jung and H. Ullmaier, J. Nucl. Mat., 90, 268 (1980).

5. L. K. Mansur, Phil. Mag. A, 39, 497 (1979).

6. H. Wiedersich and S. R. MacEwen, J. Nucl. Mat., 90, 157 (1980).

7. L. K. Mansur, J. Nucl. Mat., 83, 109 (1979).

VII. FUTURE WORK

The temperature dependence of the irradiation enhanced creep of Ni–4 % Si will be investigated.

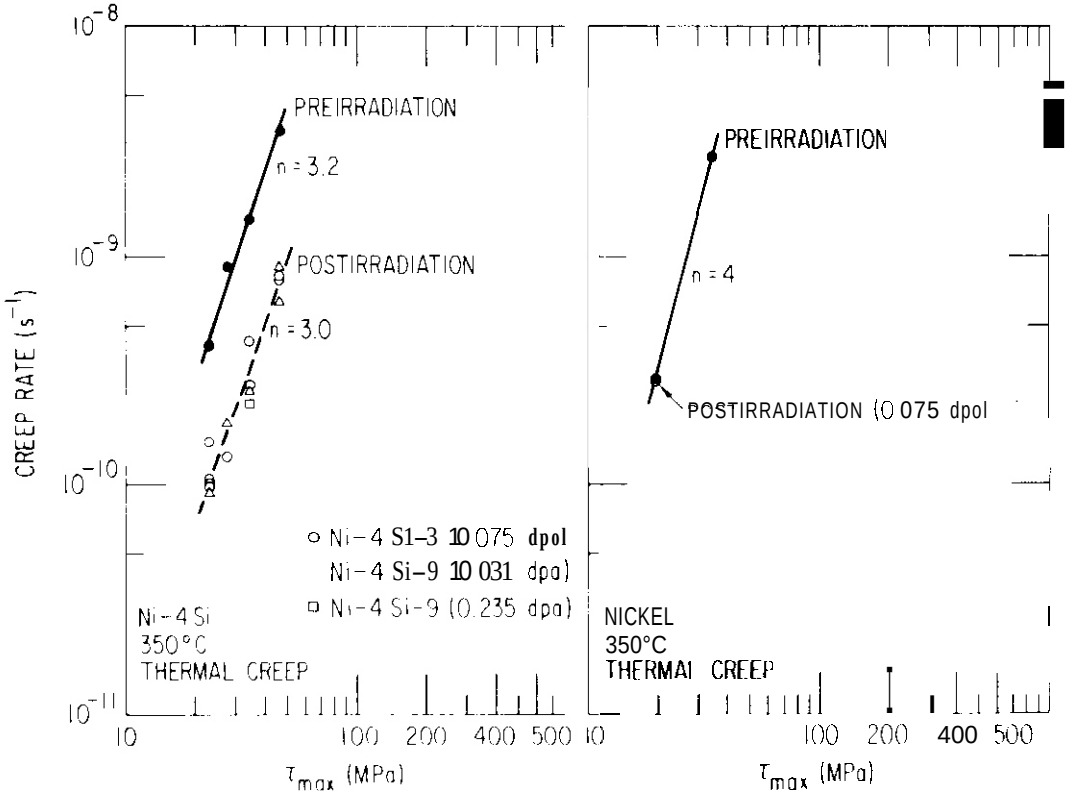

Figure 1. Comparison of the stress dependence of the thermal creep rate for Ni-4 at. % Si and pure Ni.

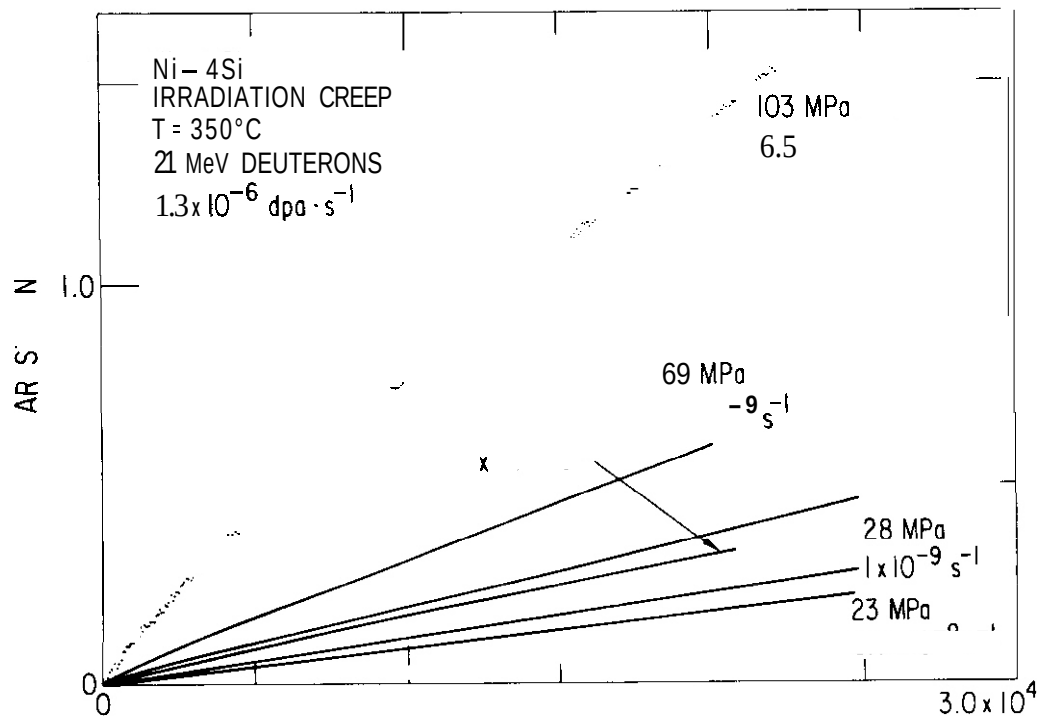

Figure 2. Irradiation creep curves (irradiation-enhanced creep strain vs. time) of Ni-4 at. % Si at 1.3 x 10^{-6} dpa • s^{-1} for various stresses. Each curve was obtained by subtracting the thermal creep component and by shifting back to the origin.

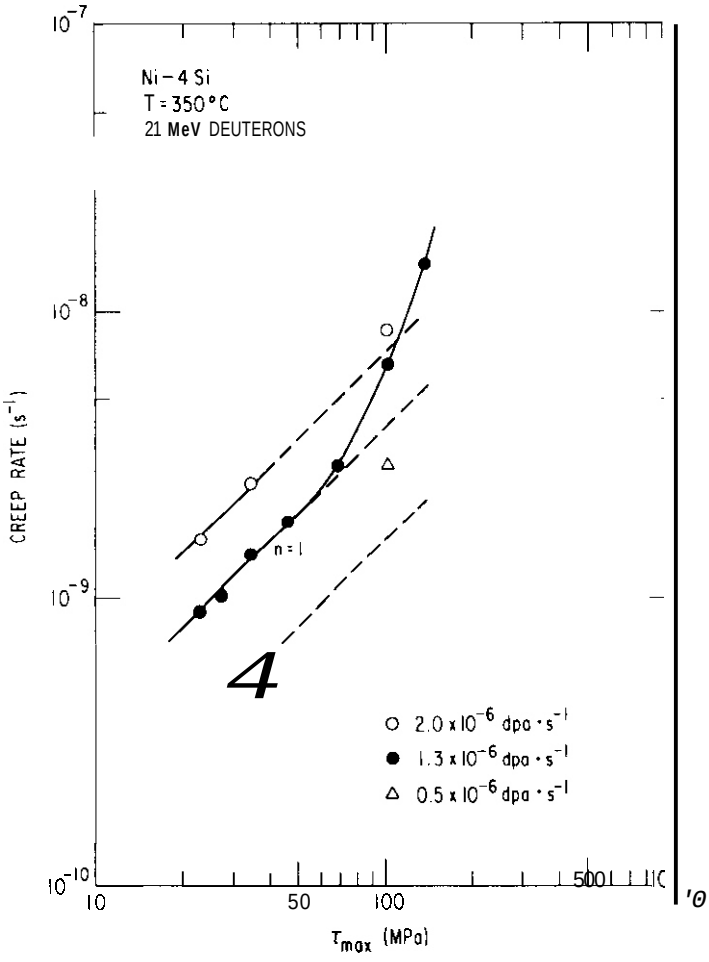

Figure 3. Stress dependence of the irradiation creep (irradiation-enhanced component) for Ni-4 at. % Si.

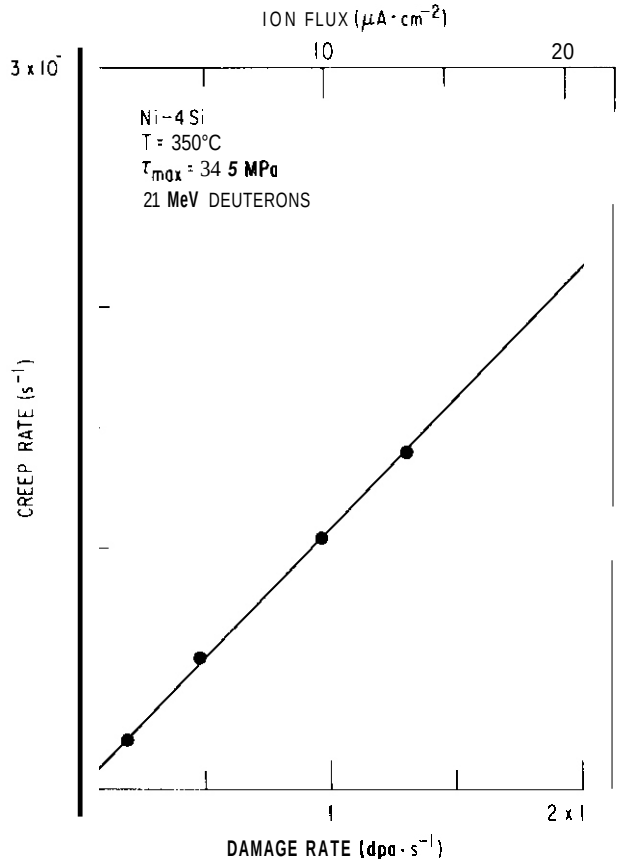

Figure 4. Irradiation creep rate (irradiation-enhanced component) as a function of damage rate (ion flux) for Ni-4 at. % Si at 34.5 MPa.

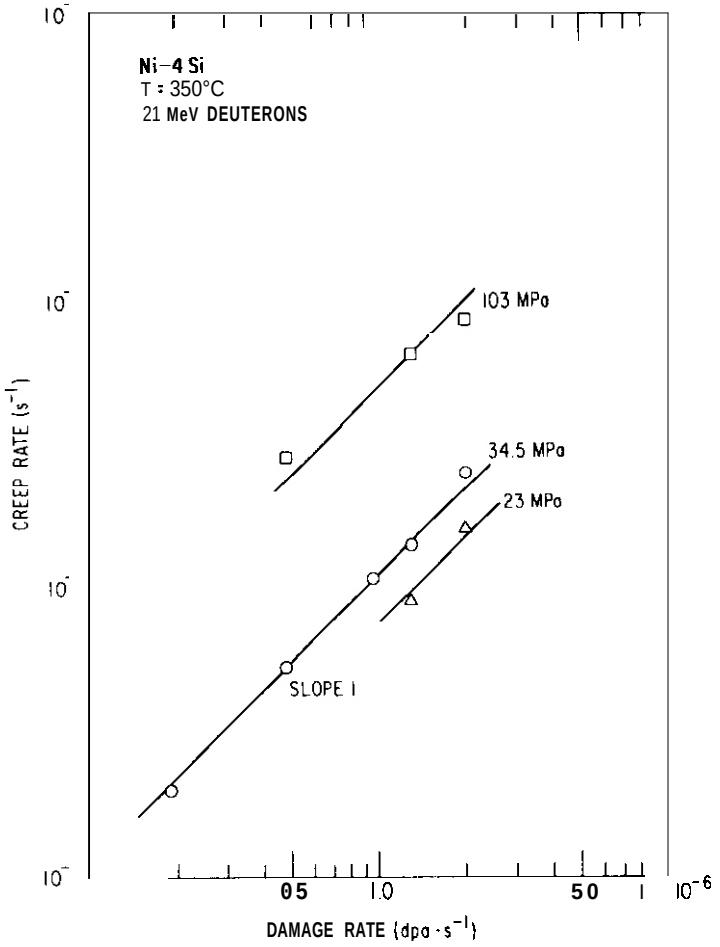

Figure 5. Damage rate dependence of the irradiation creep (irradiation-enhanced component) for Ni–4 at. % Si at 23 MPa, 34.5 MPa and 103 MPa.

I. PROGRAM

Title: Simulating the CTR Environment in the HVEM

Principal Investigators: W. A. Jesser and R. A. Johnson

Affiliation: University of Virginia

II. OBJECTIVE

The objective of this work is to investigate the influence of a radiation produced microstructure in the fracture of helium irradiated type 316 stainless steel at room temperature.

III. RELEVANT DAFS PROGRAM TASK/SUBTASK

Task II.C.14.2 Fundamental relations between microstructure and fracture mechanisms.

IV. SUMMARY

Two helium irradiated samples of type 316 stainless steel irradiated to the same fluence, but each aged at a different temperature to produce dissimilar microstructures, were both tensile tested at room temperature in an HVEM. Embrittlement occurred in the sample with no visible cavities, in contrast to the more ductile failure of the sample with large cavities.

V. ACCOMPLISHMENT AND STATUS

Room Temperature Helium Embrittlement in 316 Type Stainless Steel

J. I. Bennetch and W. A. Jesser, Materials Science Department, University of Virginia, Charlottesville, Virginia 22901.

I. Introduction

The effect of the presence of helium in the first wall candidate materials for the fusion program has been and is being extensively investigated at high temperatures. Less emphasis has been placed on helium's effects on these materials at low temperatures, e.g. room temperature,

especially under conditions when a void population is not present. Instabilities in the plasma, however, can cause large amounts of helium to be injected in a short time into the first wall, before a cavity population has developed. The intent of this research is to demonstrate that helium embrittlement in 316 SS is possible at room temperature, when no visible cavities are present.

2. Experimental Details

Electropolished electron transparent solution annealed ribbons of 316 type stainless steel were first helium ion irradiated in-situ in an HVEM-ion accelerator link to fluences $\sim 10^{18}$ cm^{-2} at an irradiation temperature of $\sim 250^{o}$ C. At a depth of 100 nm, this fluence corresponds to $\sim$ 0.01 He atoms deposited per atom (10,000 appm), if one assumes that no helium escaped during irradiation. After the irradiation was completed, Sample A was aged at 400^{o} C for 2 minutes and Sample B was aged at 900^{o} C for 10 minutes (both in a clean vacuum of about 10^{-5} Pa). Then, the samples were tensile tested to failure at room temperature in an HVEM.

3. Results

a. Microstructure

After the completion of the aging treatment at 400^{o} C, Sample A had a high density of black spot (interstitial dislocation loop) damage. Since no bubbles were visible when viewed at a magnification of 100,000, a maximum bubble diameter was estimated to be less than 2 nm. However, a high temperature aging treatment (900^{o} C) for Sample B produced in the thicker regions very large bubbles or cavities, both in the grain interior (150 nm < diameter < 400 nm) and in grain boundaries (300 nm < diameter <

800 nm). Even larger cavities were observed on occasion in both locations; however, as bubble diameters approach the film thickness (< ∿ 700 nm), the bubbles likely become penny shaped in appearance.

b. Crack Propagation Characteristics

Despite the fact that both aged samples likely contained similar amounts of helium (∿ 10,000 appm at a depth of 100 nm), the respective cracks propagated in quite different manners as the two samples were tested to failure at room temperature. Cracks advancing in Sample A (containing no visible bubbles or cavities) were of a mixed intergranular and transgranular mode. On the other hand, cracks in Sample B (containing large bubbles in the matrix and on grain boundaries) propagated in a purely transgranular mode. Further, these large helium filled cavities, instead of acting as embrittling agents in the material, were observed to behave in the opposite fashion, elongating in front of the crack tip in a ductile, not brittle, fashion. This same ductile influence of cavities on crack propagation has been observed in neutron irradiated specimens tested at 600° C [1].

Other TEM measures of ductility include crack angle and plastic zone width perpendicular to crack flanks. It has been shown, for instance, that cracks propagating in an unirradiated solution annealed sample of 316 SS tested at 25° C typically have crack angles at ∿ 10° and zone widths of 1-2 μm [2]. An examination of these criteria in Sample A revealed that crack angles ranged from 3° to 6° and zone widths ranged from 0.05 to 0.2 μm. The values of these parameters in Sample B were ∿ 10° for the crack angle and 0.3 to 0.9 μm for a range of values for the zone width.

One can clearly see the dramatic loss of ductility over unirradiated 316 SS as demonstrated in Sample A (which likely contained 10^4 appm He in the thinner regions but no visible cavities). In comparison, Sample B (which contained a similar concentration of He but had very large cavities) showed only a slight reduction in ductility, as shown by a decrease in zone width, but no change in crack angle. It is no surprise then that Sample A had brittle intergranular and transgranular cracks while Sample B had only more ductile transgranular cracks. As an illustration of these features discussed in the text, Figures 1 and 2 show micrographs of typical cracks in Samples A and B. Note the long narrow crack from Sample A in Figure 1 showing the very small plastic zone width. In comparison, the crack in Sample B in Figure 2 opened to a much larger angle. The light areas parallel to the main crack in Figure 2 are thinned regions opening in front of the crack. Their widths are a measure of the size of the plastic zone, much larger than those widths in Sample A.

4. Discussion

At first glance, the results of this investigation appear to be in direct conflict to those findings by Fish and Hunter [3] and Bloom et al. [4]. They reported only transgranular fracture for room temperature deformation of neutron irradiated stainless steel, independent of fluence and hence independent of helium concentration. However, Rawl et al. [5] and West and Rawl [6] have reported room temperature embrittlement of stainless steel containing ^3He. The resolution of this apparent paradox may be found in an examination of the microstructure. Although the fast neutron irradiated samples of Fish and Hunter [3] and of

Bloom et al. [4] do not have a cavity size quoted, Fish and Hunter's samples were damaged in the EBR-II reactor. Since the fast neutron irradiated samples tested at the University of Virginia were also damaged at that same reactor facility, the microstructures of the samples are presumed to be similar. These samples, having cavities with diameter $\leq$ 20 nm, failed in a transgranular mode at room temperature and in an intergranular mode at 600° C [1, 7]. A similar pattern was found for a certain sample helium irradiated at this facility. A 316 SS ribbon irradiated to 10^{17} cm^{-2} (probably corresponding to a 10^3 appm concentration of He at a depth of 100 nm), aged at 900° C for 38 minutes to produce $\sim$ 3.5 nm diameter cavities, contained both transgranular and intergranular cracks that were created by the aging process at the elevated temperature. Only transgranular cracks continued to grow when the sample was tested at room temperature [8]. In support of these findings, A. W. Thompson [9] noted a similar temperature dependent fracture behavior for 304L and 309S stainless steel samples containing ^3He with cavities whose diameter averaged a larger 4.5 nm diameter.

In contrast, when Rawi et al. and West and Rawl found that tritium charged stainless steel was aged at low temperatures (-20° C and 0° C, respectively) and then tensile tested, loss of ductility (and often intergranular failure) occurred at room temperature. They linked this loss of ductility to a supposed lack of ^3He filled bubbles in their samples. (Even though no TEM examinations were actually carried out on their samples, it was felt that ^3He would not cluster into bubbles at T = 0° C or -20° C.) They suggested helium, trapped in the lattice, could then

serve as pinning sites for dislocations, creating the embrittling effect observed at 25° C.

VI. CONCLUSIONS

In the present work, room temperature embrittlement occurred in a sample with no visible cavities. Since another sample with the same amount of helium but with large bubbles failed in a transgranular mode at room temperature, it can be concluded that the existence of helium in the sample is not sufficient to cause embrittlement, as has been reported previously [10]. Further, a critical parameter for helium embrittlement at room temperature appears to be a maximum cavity diameter which is apparently less than 3.5 nm.

VII. REFERENCES

1. J. I. Bennetch, J. A. Horton, W. A. Jesser, D. Kuhlmann-Wilsdorf, R. A. Johnson, and H. G. F. Wilsdorf, "In-situ HVEM Tensile Tests Irradiated and Unirradiated Stainless Steel," DAFS Quarterly Progress Report DOE/ET-0065/2 (1979) 177.

2. J. A. Horton and W. A. Jesser, "Coarse Slip Processes and Crack Propagation in Irradiated Stainless Steel" in ASTM Symposium on Effects of Radiation on Materials in Savannah, Georgia (June 3-5, 1980) (in press).

3. R. L. Fish and C. W. Hunter, "Tensile Properties of Fast Reactor Irradiated Type 304 Stainless Steel" in Irradiation Effects on the Microstructure and Properties of Metals ASTM STP 611 (1976) 119.

4. E. E. Bloom, "Irradiation Strengthening and Embrittlement" in Radiation Damage in Metals ed. by N. L. Peterson and S. D. Harkness (Metals Park, Ohio: American Society for Metals, 1976) 295.

5. D. E. Rawl, Jr., Q. R. Caskey, Jr., and J. A. Donovan, "Low Temperature Helium Embrittlement of Tritium-Charged Stainless Steel," 190th Annual AIME Meeting in Las Vegas, Nevada (Feb. 24-28, 1980) (to be published in Metallurgical Transactions).

6. A. J. West and D. E. Rawl, "Hydrogen in Stainless Steels: Isotopic Effects on Mechanical Properties" in Proceedings: Tritium Technology in Fission, Fusion and Isotopic Applications in Dayton, Ohio (Apr. 29-May 1, 1980) (Southwestern Ohio Section, American Nuclear Society, 1980) CONF-800427, 69.

7. W. A. Jesser, J. A. Horton, and J. I. Bennetch, "In-situ HVEM Tensile Tests of Irradiated and Unirradiated Stainless Steel," DAFS Quarterly Progress Report DOE/ET-0065/1 (1978) 204.

8. J. I. Bennetch, R. D. Gerke, and W. A. Jesser, "HVEM Observations of Crack Propagation in Helium Irradiated Type 316 Stainless Steel Containing Precipitates," DAFS Quarterly Progress Report DOE/ET-0046/2, 75.

9. A. W. Thompson, "Mechanical Behavior of Face-Centered Cubic Metals Containing Helium," Materials Science and Engineeri (1975) 41.

10. J. I. Bennetch, J. A. Horton, and W. A. Jesser, "An Experimental Investigation Into Some Parameters and Fracture Criteria Used in Recent Helium Embrittlement Theories," DAFS Quarterly Progress Report DOE/ET-0065/8 (1980) 131.

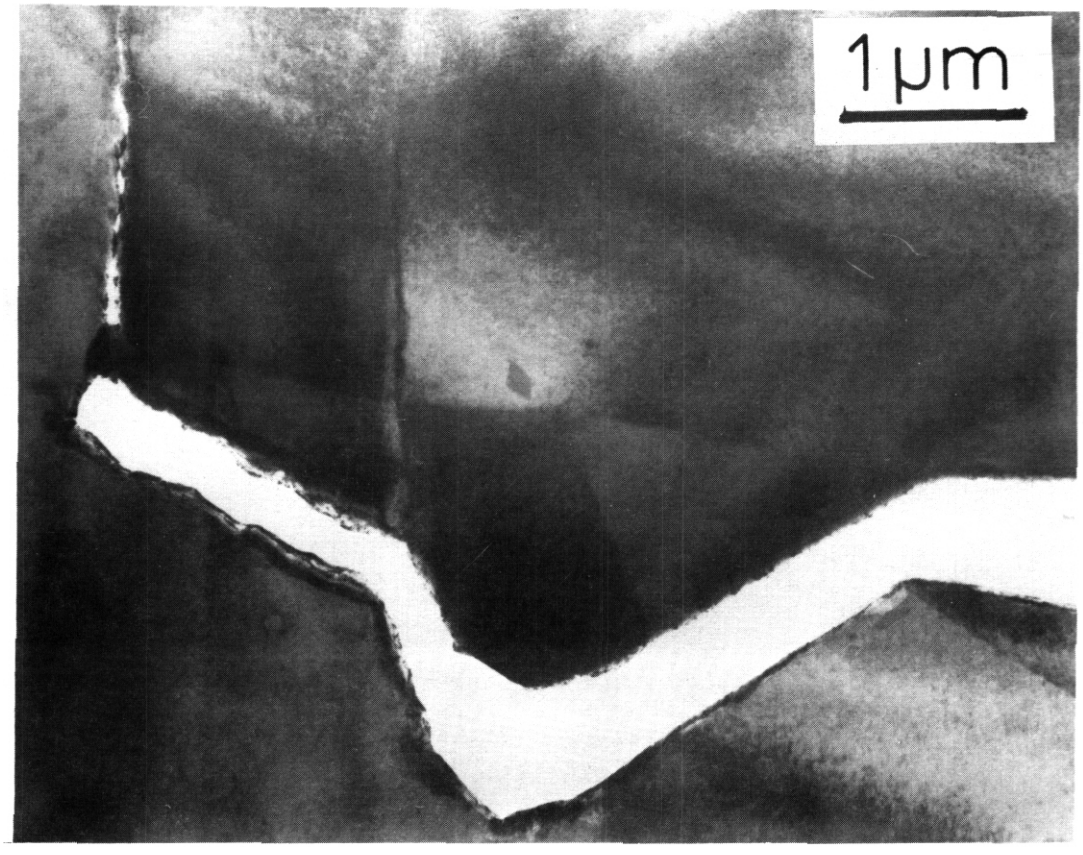

Figure 1: TEM micrograph of an intergranular crack propagating in Sample A, which was helium irradiated to a fluence of $\sim 10^{18}$ cm^{-2} ($\sim 10^{4}$ appm of He at a depth of 100 nm) aged for 2 minutes at 400° C and tested at room temperature.

Figure 2: HVEM micrograph of a transgranular crack propagating in Sample B, which was helium irradiated to a fluence of $\sim 10^{18}$ cm^{-2} ($\sim 10^{4}$ appm of He at a depth of 100 nm) aged for 10 minutes at 900^{o} C and tested at room temperature.

CHAPTER 4

CORRELATION METHODOLOGY

I. PROGRAM

Title: Effects of Irradiation on Fusion Reactor Materials
Principal Investigators: A. P. L. Turner and F. V. Nolfi, Jr.
Affiliation: Argonne National Laboratory

II. OBJECTIVE

The objective of this work is to determine the extent and characteristics of solute redistribution during irradiation in candidate classes of MFR alloys, and its concomitant effect on phase stability and materials properties.

III. RELEVANT OAFS PROGRAM PLAN TASK/SUBTASK

SUBTASK II.C.1 - I - Phase Stability Mechanism Experiments

IV. SUMMARY

Radiation-induced segregation (RIS) of alloying elements to the surface during 3 MeV $^{58}Ni^{+}$ ion bombardment was investigated in alloys of Fe-20Cr-12Ni (at. %) containing controlled additions of Si and Mo. The segregation profiles, determined by Auger electron spectroscopy, show that Ni and Si are enriched, while Cr and Mo are depleted at the irradiated surfaces. The data indicates that the RIS of Ni and Cr are affected by the presence of Mo and Si in the alloy. However, no obvious trends are observed as a function of the minor solute concentration. The temperature dependence of the RIS of the alloying elements was also investigated. A local maximum of segregation at $\sim$ 500°C is observed for Si followed by a sharp increase in segregation at higher temperatures. The temperature dependence of segregation for Cr, Ni and Mo shows continuous increase with temperature in the temperature regime investigated.

The void swelling data on these alloys is also presented as a function of temperature and composition. Additions of Si reduce the swelling by affecting both the nucleation and the growth of the voids. The swelling temperature for all the alloys containing minor solutes are found to be lower ($\sim$ 50°C) than that of the base alloy (peak swelling temperature $\sim$ 660°C).

V. ACCOMPLISHMENTS AND STATUS

A. Effects of Minor Elements on the RIS and Swelling in Type 316 SS Alloys -- V. K. Sethi

1. Introduction

Radiation-induced segregation (RIS) of alloying elements to and away from defect sinks during displacement producing irradiations is a commonly observed phenomenon. Over the past few years, numerous experimental observations have been made on various binary alloys (1-16), while the number of investigations that dealt with the understanding and characterization of the RIS in complex alloys is limited (17-21). In engineering alloys, the compositional modifications caused by RIS can have a deleterious effect on the alloy performance with respect to the void swelling, mechanical properties, and corrosion resistance. An understanding of RIS and its extent in these alloys is thus of considerable importance in fission and fusion reactor technology.

We report here results on Fe-20Cr-12Ni (at. %) alloys with minor additions of Mo and Si. Segregation of the alloying elements, and void swelling of the alloys were determined as a function of temperature and composition, in order to establish a correlation between the two phenomenon.

2. Experimental

Samples in the form of 3mm disks were punched out from the rolled stock of Fe-20Cr-12Ni; Fe-20Cr-12Ni-1Si; Fe-20Cr-12Ni-2Si; Fe-20Cr-12Ni-1Mo; Fe-20Cr-12Ni-2Mo; Fe-20Cr-12Ni-1Mo-1Si; and Fe-20Cr-12Ni-2Mo-2Si (at. %) alloys. The alloys were prepared from high purity starting materials by vacuum arc melting, and were homogenized by leviation. Samples were solution annealed in an inert atmosphere for 2 h at 1050°C, followed by an 8 h aging treatment at 800°C. Prior to irradiation, one surface of each sample was metallographically polished optically flat and then electropolished to remove any cold-worked surface material.

Irradiations were performed at the Argonne National Laboratory Dual-Ion Irradiation Facility with 3.0 MeV $^{58}Ni^{+}$ ions in 10^{-8} torr vacuum. An infrared pyrometer was used to monitor the individual sample temperatures during irradiation. Alloy samples were irradiated at various temperatures to $\sim 2 \times 10^{-3}$ dpa $. s^{-1}$. The rate at the surface of the sample was $\sim$ 30% of the peak rate. The doses were calculated by the Brice codes RASE3 and DAMG2 (22) using a displacement energy of 40 eV.

The irradiated surfaces were composition depth profiled by Auger electron spectroscopy using a primary electron beam of 5 kV. Sputtering with 1 kV argon ions was interrupted periodically to record Auger spectra. The concentrations of major alloying elements were calculated using sensitivity factors determined from the standard alloys of Fe-Cr-Ni. For minor elements the sensitivity factors used were those available in the literature (23).

Void swelling measurements were made by transmission electron microscopy. Irradiated specimens, after AES depth profiling, were electrochemically sectioned to the peak damage region and back-thinned for TEM observations.

3. Results

The composition depth profiles for various alloys are shown in Figs. 1-7. Each figure shows depth profiles of specimens irradiated at 430°, 540°, 600" and 675° (± 5°)C. Considerable solute redistribution is obvious (no significant compositional variations are observed in un-irradiated control specimens, except for a slight enrichment of Cr at the surface caused by oxidation). In all the alloys and at all the temperatures, RIS of the constituent elements is consistent with the predictions of the size-effect (18). Ni and Si are undersize solutes and are enriched in the near surface region, while Cr and Mo are oversize solutes in these alloys and are depleted. It should be noted that frequently a narrow Cr peak is observed close to the surface. A careful analysis of the Auger spectra obtained from the near surface region indicated that the surface region (∿ 2 nm) contained an appreciable amount of oxygen, indicating that the excess Cr could be related to the slight oxidation that occurs either during irradiation or during subsequent storage.

Comparison of the Ni profiles in various alloys shows that in Si containing alloys in Figs. 2, 3, 6 and 7, at temperatures where considerable Si segregation occurs, the maximum Ni concentration is observed not at the irradiated surface but at depths where Si concentration falls to ∿ 15 at. %. In addition, although the enrichment of Ni in the near surface region varies and can be as large as 45 at. %, the concentration of Ni in the underlying depleted zone is always ∿ 10 at. %. Maximum Si concentration is always observed at the irradiated surface, and in some cases is as large as 50 at. %.

For quantitative comparison of the RIS of Cr, Ni, Si and Mo as a function of composition and temperature, a measure of segregation was defined as the amount of solute transported to or away from the surface. This quantity is determined by integrating the excess (or deficit) of the concentration above (or below) the concentration C_B from the surface

to the appropriate depth where $C = C_B$ (the bulk concentration).

The segregation of Ni and Cr as a function of Si and Mo content of the alloy are shown in Figs. 8(a) and 8(b). Clearly, the minor solute additions affect the segregation of the major alloying elements. The data shows that in general, Si additions affect the segregation of Ni and Cr more than do the Mo additions. No clear trends are observed as a function of minor solute concentration.

The temperature dependencies of the RIS of various elements in these alloys are shown in Fig. 10. It is evident that the segregation of Ni, Cr, and Mo increases monotonically with increasing temperature in the temperature regime investigated. The temperature dependence of Si segregation exhibits a maximum at $\sim 600°C$, and a sharp increase at higher temperatures.

The void swelling data obtained from the same specimens on which AES measurements were made is shown in Figs. 11-14, as a function of temperature and composition. The main features of the data are

1. Si additions to the alloys inhibit swelling by affecting both the nucleation and the growth of the voids.

2. The effects of Mo additions on the swelling appear to be complex. Increasing additions of Mo to the base alloy first increase the swelling and then decrease. Similar behavior is observed when Mo is added to the Si containing alloys.

3. The peak swelling temperature for the base alloy (Fe-20Cr-12Ni) is $\sim 660°C$, and shifts to lower temperatures with the addition of minor solutes.

These observations are consistent with those of previous investigators on similar alloys (24-28).

4. Discussion

Radiation-induced solute segregation can be understood in terms of a preferential migration of interstitials via undersize solute atoms, and of vacancies via oversize solute atoms resulting in the transport of the undersize solutes to the sinks (enrichment), and the transport of the oversize solutes away from the sinks (depletion) (18). However, since during irradiation the mass transport occurs via the vacancy as well as via the interstitial flux. The transport of any given alloying component by the interstitial flux to the sink, and by the vacancy flux away from the sink compete against each other. For a concentrated alloy Wiedersich and co-workers (29) have shown that the depletion of a component occurs at the sinks when the preferential transport of the component atoms by vacancies outweighs that by interstitials. Conversely, enrichment of the component occurs. Maximum enrichment (depletion) of the alloying element occurs when the atoms diffuse exclusively via an interstitial (vacancy) mechanism. It appears likely that transport by interstitials dominates for undersize elements and by vacancies for oversize elements. As stated earlier, the depletion of Cr and Mo and the enrichment of Ni and Si near the surface are consistent with this interpretation.

For dilute solutes the mobile defect-solute complexes concept may also be important. Solute atoms interact with vacancies and/or self interstitials to form mobile defect-solute complexes that undergo protracted random walks before thermally dissociating. In initially homogeneous alloys, the flow of interstitial-solute complexes, and strongly bound vacancy solute complexes can cause solute enrichment at sinks. For small binding energies (< 0.1 -0.2 eV) between solute atoms and vacancies, theoretical calculations for dilute binary alloys show that depletion can occur at the sinks **(30).** The observed depletion of Mo at the surface indicates that the binding energy between Mo atoms and vacancies must be small and, hence, vacancy complex formation is unimportant for Mo.

The defect-solute complexes are likely to be more important for an undersize solute like Si that traps interstitials more strongly than do oversize solutes. The transport of Si in Fe-Cr-Ni base austenitic alloys to the surface could be described as Si-interstitial complex migration. Strongly bound Si-interstitial complexes are consistent with the effectiveness of Si in reducing swelling in these alloys, presumably by interstitial trapping. The observation that the maximum in the Ni concentration in the Si-bearing alloys is distinctly displaced from the surface can be related to the very strong coupling of the Si to the defect fluxes which is also apparent from the steep drop-off of the Si concentration profile.

The temperature dependence of Si segregation shows a local maximum at relatively low temperatures, followed by a minimum and then a sharp rise for temperatures > 600°C. The behavior could be due to either a change in segregation mechanism or due to a change in the sink structure in the vicinity of the irradiated surface. The low temperature maximum in Si segregation occurs in the temperature regine where γ' phase has been observed in neutron irradiated annealed and 20% cold-worked 316 stainless steel (31).

Void swelling is similar to RIS in that it is caused by the flow of vacancies and interstitials to sinks. Therefore both phenomena are expected to occur in a comparable temperature regime, and to exhibit similar temperature dependences. In binary alloys there is evidence that such a correlation does exist. For example, Rehn and co-workers (10) showed that in Ni-1 % Si alloy, maximum segregation is observed at 560°C, approximately the maximum swelling temperature for pure Ni (32). Even though we find swelling maxima in all our alloys between ~ 600° and 650°C, the amount of segregation of Ni, Cr, and Mo increases monotonically with temperature throughout the range investigated. It should be pointed out that the quantitative description of segregation used in this work is different from the one used by Rehn et al. (10).

VI. REFERENCES

1. P. R. Okamoto, A. Taylor and H. Wiedersich, in: Fundamental Aspects of Radiation Damage in Metals, Vol. II (CONF-751006-D2-1975) p. 1188.

2. A. Barbu and A. J. Ardell, Scripts Met. 9 (1975) 1233.

3. G. Silvestre, A. Silvent, C. Regnard and G. Sainfort, J. Nucl. Mater. 57 (1975) 125.

4. A. Barbu and G. Martin, Scripta Met. 11 (1977) 771.

5. D. I. Potter, L. E. Rehn, P. R. Okamoto and H. Wiedersich, Scripta Met. 11 (1977) 1095.

6. D. I. Potter and D. G. Ryding, J. Nucl. Mater. 71 (1977) 14.

7. A. D. Marwick and R. C. Pillar, Radiation Effects 33 (1977) 245.

8. G. Martin, J. L. Bocuet, A. Barbu and Y. Adda, in: Radiation Effects in Breeder Reactor Structural Materials, Eds. M. L. Bleiberg and J. W. Bennett (AIME, New York 1977) p. 899.

9. R. C. Pillar and A. D. Marwick, J. Nucl. Mater. 71 (1978) 309.

10. L. E. Rehn, P. R. Okamoto, O. I. Potter and H. Wiedersich, J. Nucl. Mater. 74 (1978) 242.

11. P. P. Pronko, P. R. Okamoto and H. Wiedersich, Nucl. Instr. Methods 149 (1978) 77.

12. L. E. Rehn, P. R. Okamoto and H. Wiedersich, J. Nucl. Mater. 80 (1979) 172.

13. A. D. Marwick, R. C. Pillar and P. M. Sivell, J. Nucl. Mater. 83 (1979) 35.

14. D. I. Potter and H. Wiedersich, J. Nucl. Mater. 83 (1979) 208.

15. R. Cauvin and G. Martin, J. Nucl. Mater. 83 (1979) 67.

16. P. R. Okamoto and L. E. Rehn, J. Nucl. Mater. 83 (1979) 2.

17. P. R. Okamoto, S. D. Harkness and J. J. Laidler, ANS Trans. 16 (1973) 70.

18. P. R. Okamoto and H. Wiedersich, J. Nucl. Mater. 53 (1974) 336.

19. W. G. Johnston, W. G. Morris and A. M. Turkalo, in: Radiation Effects in Breeder Reactor Structural Materials, Eds. M. L. Bleiberg and J. W. Bennett (AIME, New York 1977) p. 421.

20. R. E. Clausing and E. E. Bloom, in: Grain Boundary in Engineering Materials, Eds. J. L. Walters, J. W. Westbrook and D. A. Woodford (Claitors, Baton Rouge, 1975) p. 491.

21. V. K. Sethi, DAFS Quarterly Progress Report, Oct.-Dec. 1978, p. 103 [The data also appears in the review article by Okamoto and Rehn - Reference 16].

22. D. K. Brice, Sandia Laboratories, Albuquerque, New Mexico, Research Report SLA-73-0416 (1973).

23. "Handbook of Auger Electron Spectroscopy" Physical Electronics Industries, Inc. (1976).

24. J. F. Bates, J. J. Holmes, M. M. Paxton and J. L. Straalsund, U. S. Pat. 3, 856, 517 (1974).

25. W. G. Johnston, T. Lauritzen, J. H. Rosolowski, and A. M. Turkalo, J. Metals, June 1976.

26. M. J. Makin, J. A. Hundson, D. J. Mazey, R. S. Nelson, G. P. Walters and T. M. Williams, in: Radiation Effects in Breeder Reactor Structural Materials, Eds. M. L. Bleiberg and J. W. Bennett (AIME, New York, 1977) p. 645.

27. J. F. Bates and W. G. Johnston, in: Radiation Effects in Breeder Reactor Structural Materials, Eds. M. L. Bleiberg and J. W. Bennett (AIME, New York, 1977) p. 625.

28. G. R. Gessel and A. F. Rowcliffe, in: Radiation Effects in Breeder Reactor Structural Materials, Eds. M. L. Bleiberg and J. W. Bennett (AIME, New York, 1977) p. 431.

29. H. Wiedersich, P. R. Okamoto and N. Q. Lam, J. Nucl. Mater. 83 (1979) 98.

30. H. Wiedersich, P. R. Okamoto and N. Q. Lam, in: Radiation Effects in Breeder Reactor Structural Materials, Eds. M. L. Bleiberg and J. W. Bennett (AIME, New York, 1977) p. 801.

31. H. R. Brager and F. A. Garner, in: Effects of Radiation on Structural Materials, ASTM STP 683, J. A. Sprague and D. Krarner, Eds., American Society for Testing and Materials, 1979, pp. 207-232.

32. T. D. Ryan, Ph.D. Thesis, University of Michigan, Ann Arbor, Michigan (1975).

VII. FUTURE WORK

No further experiments are planned to study the effect of minor solute

elements on the RIS behavior or void swelling behavior of Type 316 stainless steel alloys. The extent of RIS in other candidate classes of MFR alloys is currently being investigated.

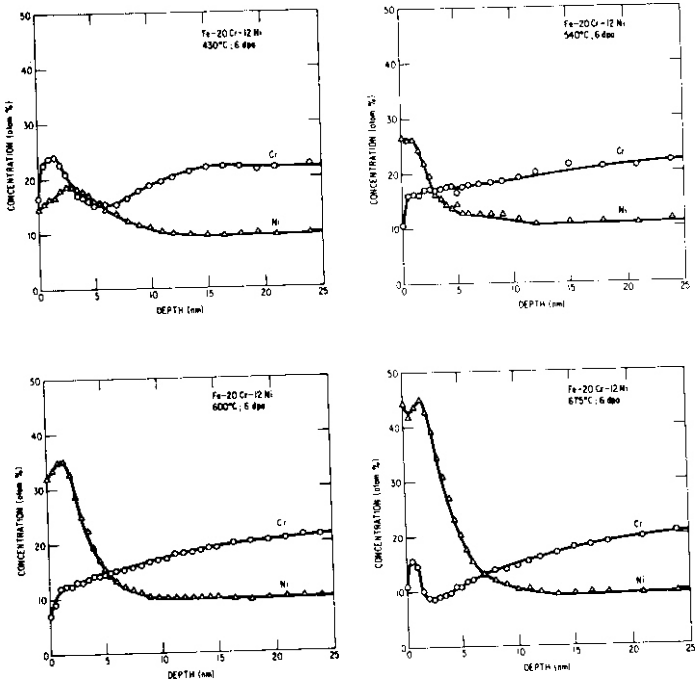

Figure 1. Composition depth profiles of the solute elements in the Fe-20Cr-12Ni base alloy.

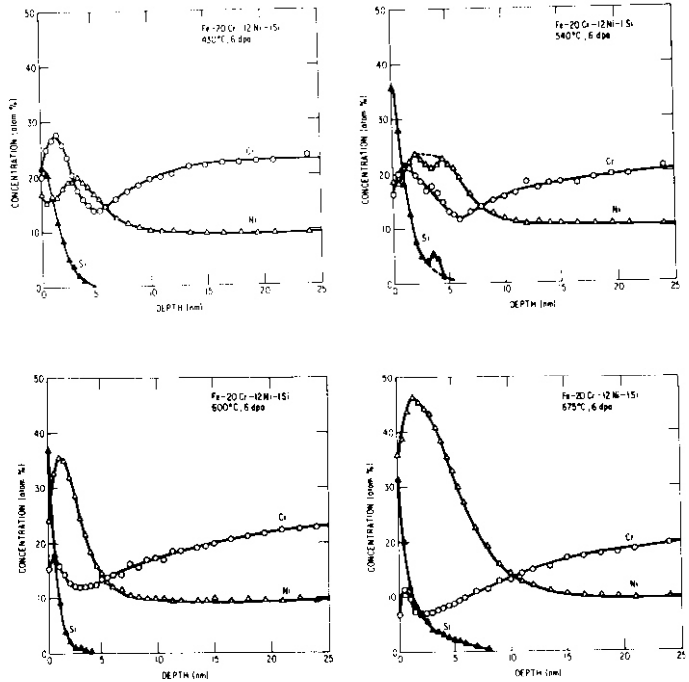

Figure 2 Composition depth profiles of the solute elements in the Fe-20Cr-12Ni-1Si alloy.

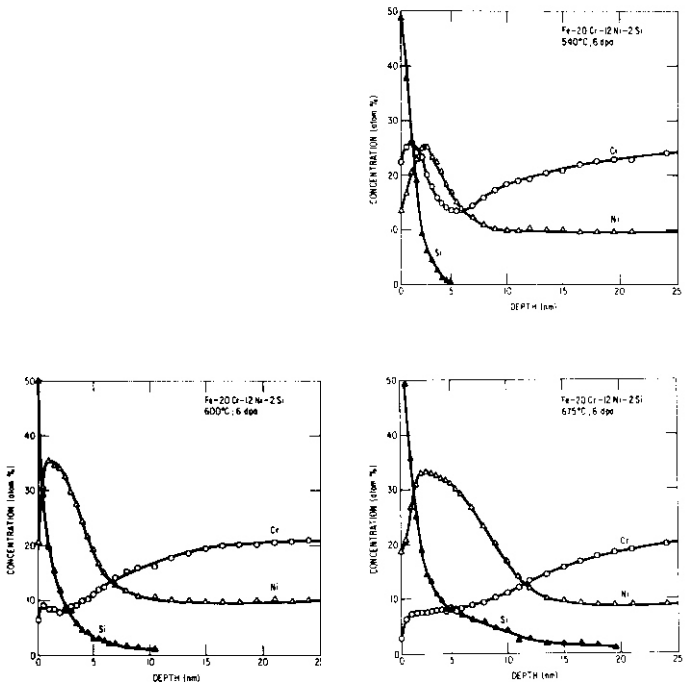

Figure 3 Composition depth profiles of the solute elements in the Fe-20Cr-12Ni-2Si alloy.

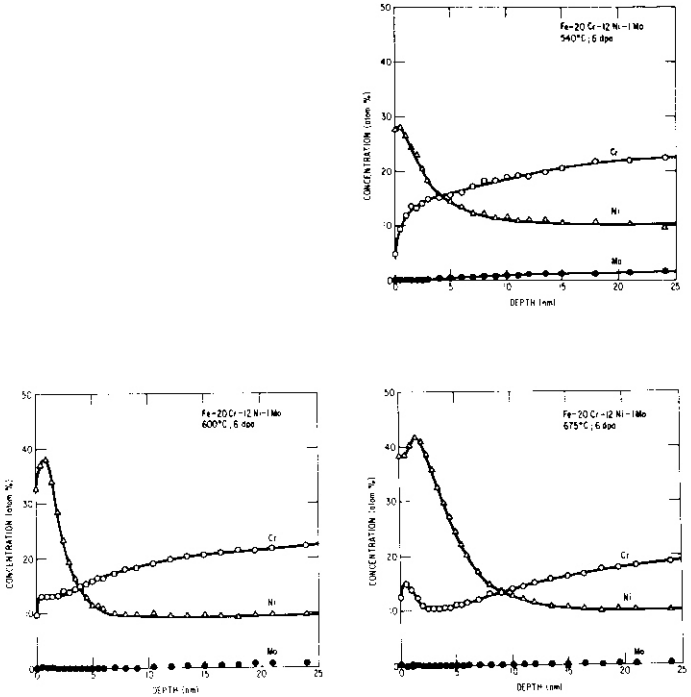

Figure 4. Composition depth profiles of the solute elements in the Fe-20Cr-12Ni-1Mo alloy.

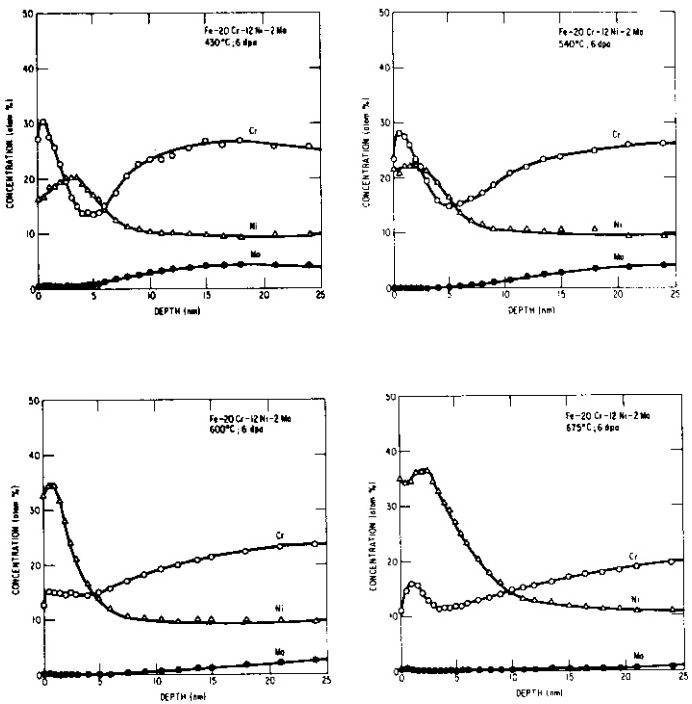

Figure 5. Composition depth profiles of the solute elements in the Fe-20Cr-12Ni-2Mo alloy.

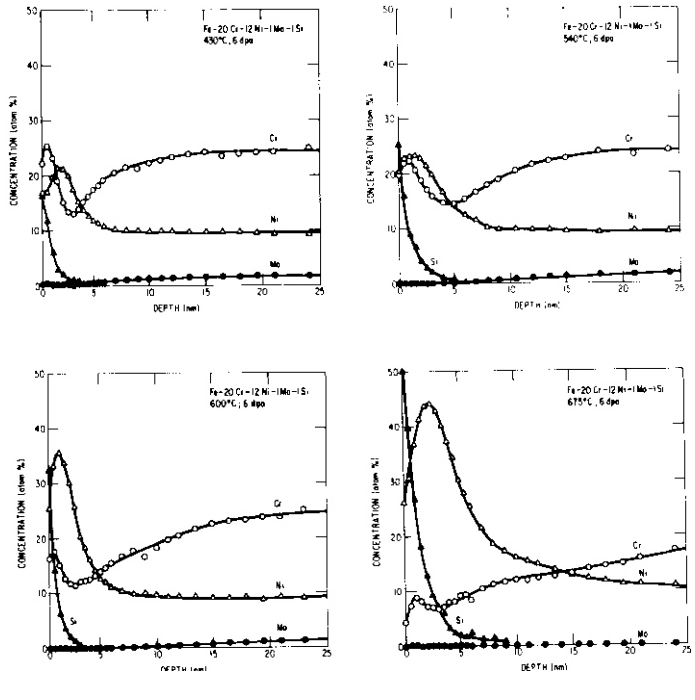

Figure 6. Composition depth profiles of the solute elements in the Fe-20Cr-12Ni-1Mo-1Si alloy.

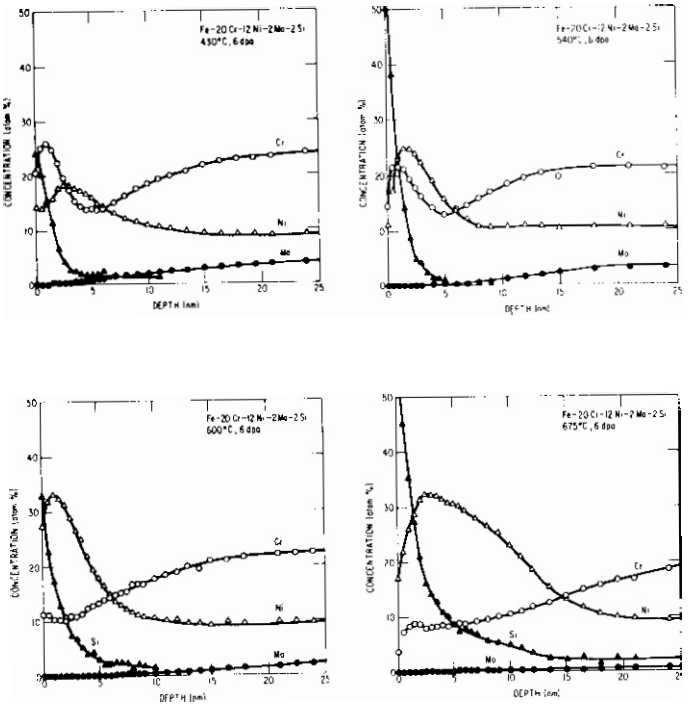

Figure 7. Composition depth profiles *of* the solute elements in the Fe-20Cr-12Ni-2Mo-2Si alloy.

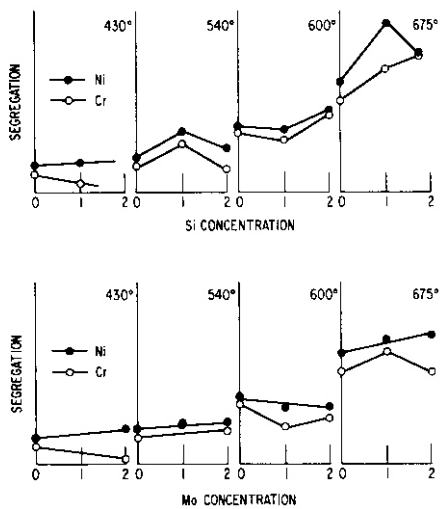

Figure 8 Segregation of Ni and Cr in Fe-20Cr-12Ni alloys as a function of minor solute concentration.

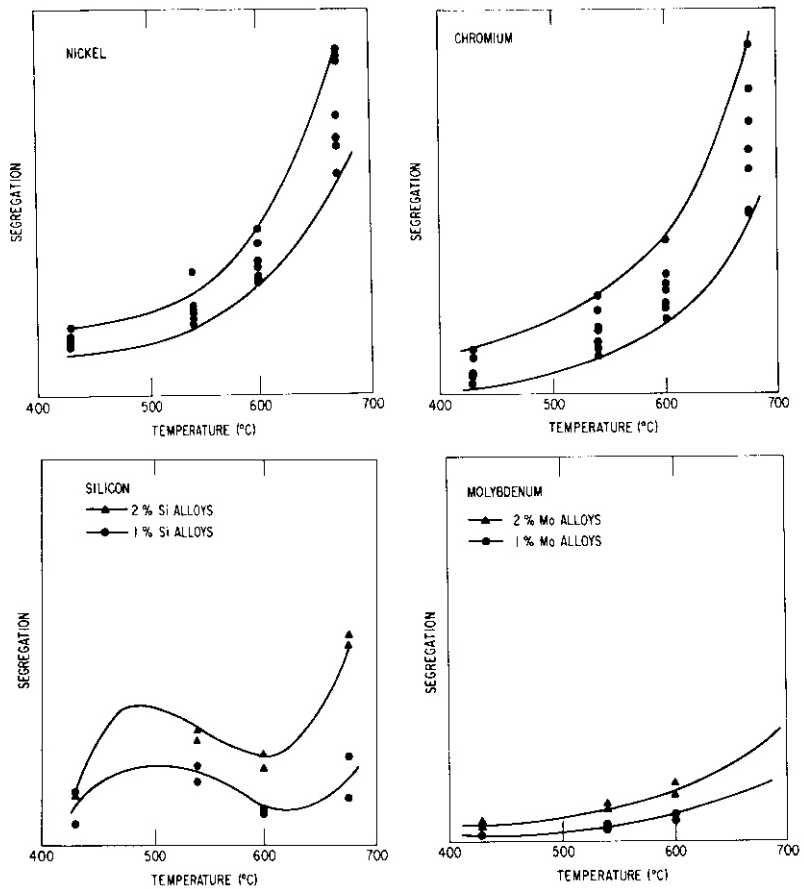

Figure 9 Temperature dependence of the RIS of alloying elements in Fe-20Cr-12Ni based alloys.

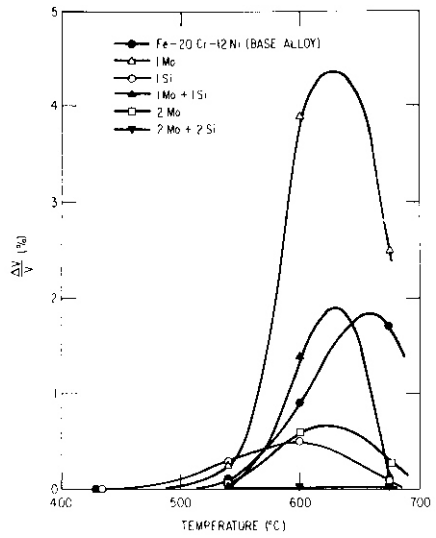

Figure 10. Temperature dependence of void swelling in various alloys irradiated to ∿ 6 dpa with 3 MeV $^{58}Ni^{+}$ ions.

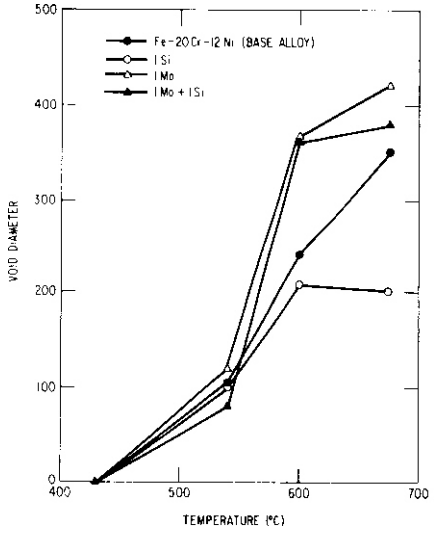

Figure 11. The void diameter in 3 MeV $^{58}Ni^{+}$ ion irradiated alloys as a function of temperature. Total dose ∿ 6 dpa.

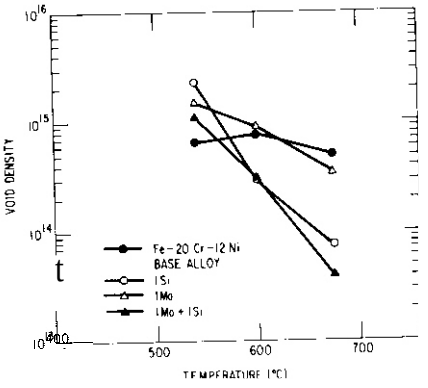

Figure 12. The void density in 3 MeV $^{58}Ni^{+}$ ion irradiated alloys as a function of temperature. Total dose ∿ 6 dpa.

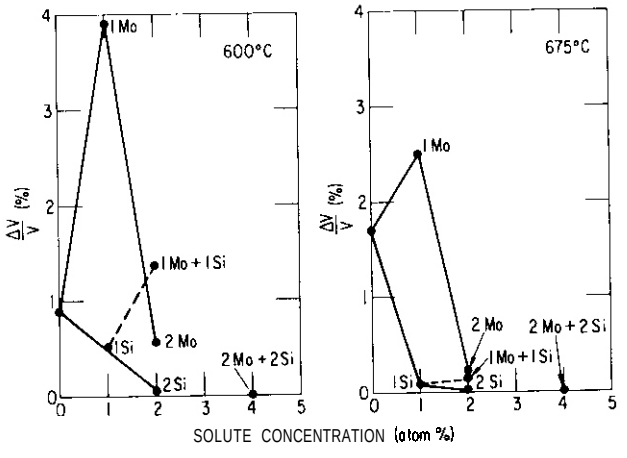

Figure 13. The void swelling data of Figure 10 plotted as a function of minor solute concentration in Fe-20Cr-12Ni base alloy.

I. PROGRAM

Title: Irradiation Response of Materials

Principal Investigators: S. Wood, J. A. Spitznagel and W. J. Choyke

Affiliation: Westinghouse Research and Development Center

II. OBJECTIVE

The objective of this work is to assess the phenomenology and mechanisms of microstructural evolution in materials exposed to simultaneous helium injection and creation of atomic displacement damage by a second ion beam.

III. RELEVANT DAFS PROGRAM TASK/SUBTASK

SUBTASK II.C.1, II.C.2, II.C.3, II.C.5, II.C.9, II.C.18

IV. SUMMARY

Microstructural evaluation of dual-ion bombarded titanium-modified 316 SS from the same heat of material used in previous HFIR studies has been completed. The results demonstrate that the same helium trapping mechanism operates at He:dpa ratios of 0.2:1, 12:1 and 70:1 corresponding to EBR-II, Tokamak and HFIR conditions when MC carbide particles precipitate. When the MC particles do not form, swelling can be as great as that observed in unmodified 316 SS at identical He:dpa ratios, bombardment temperatures and dpa rates. Inhomogeneous distributions of Ti and C in "stringers" leads to nonreproducible results and spatially inhomogeneous swelling behavior.

V. ACCOMPLISHMENTS AND STATUS

A. Microstructural Analysis of Simultaneously Bombarded Ti-Modified 316 SS

Some recent work by Maziasz and Bloom[1] has shown that dramatic reductions in swelling in Ti-modified 316 SS can be obtained with respect to a standard SA 316 SS. Figure 1 illustrates the reason for this change in the cavity volume. After irradiation in HFIR at 610°C to 57 dpa and 3400 appm He, TEM analysis revealed that MC carbides had nucleated and grown in the austenite matrix, and that the carbide/austenite interface appeared to be a very effective collection site for helium and vacancies. This resulted in the encrustation of the carbides by numerous small helium bubbles, as shown in Fig. 1. (Note that the scale of both micrographs is such that the length of the rod-shaped precipitate is ~100 nm). Two precipitate morphologies were observed: namely, cube-on-cube and rod-like. Both appear to be equally effective in stabilizing small bubbles. The low swelling in this material is a direct result of the vacancy and helium trapping at the interface since the bubbles remain small in size (~10 nm after 57 dpa) and do not reach the bias driven growth regime.[2]

These results by Maziasz and Bloom suggested the need to further investigate the helium trapping mechanism and its dependence upon such parameters as temperature, helium injection and damage rates. Dual ion bombardment is an efficient way of performing such an investigation since it provides a rapid means of accurately and independently changing the variables of interest. The dual-ion results presented here encompassed a matrix of specimens irradiated between 550 to 700°C and with appm He/dpa ratios of 70:1, 12:1 and 0.2:1 corresponding to HFIR, anticipated first wall fusion and E8R-II conditions, respectively. All specimens were dually bombarded with a damage rate of ~10^{-4} dpa/s (and, therefore, helium injection rates corresponding to the appm He/dpa ratios). Most microstructural analyses, to date, have been performed at a section depth corresponding to a fluence of ~3 dpa.

Table 1 compares the composition of the Ti-modified 316 SS utilized in the investigation with that of the SA 316 SS from the MFE heat which was studied earlier in the program. The principal difference between the two is the higher Ti and Mo and lower Mn content of the Ti-modified material. As mentioned in a previous report,[3] which presented preliminary data on the Ti-modified steel, the final thermomechanical history of the material was a 50% reduction in area of the rod by cold swaging followed by a solution anneal for 1 h at 1050°C. The anneal was performed in vacuum and followed by an argon quench. This treatment yielded an initial inhomogeneous MC carbide distribution of $\sim 3 \times 10^{13}$ particles/cm^3 with an average diameter of 30-40 nm.

TABLE 1 - COMPOSITION OF 316 SS USED IN DUAL ION BOMBARDMENT STUDIES

Alloy	Cr	Ni	Mo	Mn	C	Ti		P	S	N	B
Standard (MFE) 316 SS	17.4	12.4	2.21	1.80	0.05	<.001	0.68	0.033	0.015	0.044	<.0030
Ti-Modified 316 SS	17.0	12.0	2.50	0.50	0.06	0.230	0.40	0.010	0.130	0.005	0.0007

* Balance Fe

The first dual ion experiment on the 316 SS + Ti was performed at 600°C and with an appm He/dpa ratio of 70:1. Microstructural data from this specimen are presented in Figs. 2 and 3. Figure 2 reveals two very interesting developments. First, as shown by the DF micrograph, copious MC carbide precipitation was induced during bombardment. It is entirely of the cube-on-cube morphology and the rod-shaped particles observed by Maziasz in HFIR irradiated samples were not seen in this specimen (even utilizing the optimum g = [220]). The second important result is that the swelling is very low compared to SA 316 SS irradiated under the same conditions.[4] Close inspection of the absorption contrast micrograph showing the bubbles/cavities and precipitates reveals that, in addition to the few

heterogeneously distributed "large" cavities, there are numerous small (≤3 nm diameter) bubbles associated with the carbide particles. Thus, it is apparent that the helium trapping mechanism at the carbide/austenite interface is also effective at these higher damage and helium injection rates.

Figure 3 compares the cavity and dislocation microstructures which developed at 12:1 and 70:1 appm He/dpa ratios (at 600°C). It must be noted that the apparent cavities present in the 12:1 specimen were shown by stereo observations to be polishing artifacts developed during the thin foil preparation procedure. In fact, no visible bubbles were detected in this foil which means that again the swelling was very much reduced compared to SA 316 SS bombarded under the same experimental conditions. [Our SA material from the MFE heat exhibited the anomalous cavity growth phenomenon with concomitant high swelling at this temperature and fluence.[4]] The absence of any visible cavities in the 316 SS + Ti suggests that, despite the lack of DF evidence, He was again being effectively trapped on a very fine scale. Close inspection of the dislocation micrograph indicates the presence of a low No. density of MC carbides which are thought to be the original thermally produced precipitates. Comparison of the two dislocation structures reveals a higher number density of faulted loops at 12:1. It is not known whether this truly reflects the well-documented[5] effect of helium on loop formation or is simply a manifestation of the material inhomogeneity. This latter point will be discussed further later.

As might be expected, at an appm He/dpa ratio of 0.2:1, at the same bombardment temperature, no visible bubbles were observed (apparent cavities are due to specimen preparation [Fig. 4]). The dislocation microstructure shows some small faulted loops and possibly a few MC carbides (which may have been thermally produced). DF microscopy failed to image the MC carbides due, presumably, to the low number density.

At 700°C (Fig. 5) low swelling was again observed for both 12:1 and 70:1 appm He/dpa ratios. The most common form of precipitates were the small rod-shaped particles associated with cavities which may be the second variant of MC carbide found by Maziasz (Fig. 1). Some evidence for cube-on-cube particles along dislocations is also shown in the higher helium concentration specimen. However, it is suspected that invisible MC clusters may be providing the bulk of the helium trapping sites but considerable searching with DF microscopy failed to reveal such small precipitates. The dislocation structure in the high helium specimen was composed almost entirely of line dislocations suggesting again that helium was not acting as a loop growth inhibitor.[5] At the lower appm He/dpa ratio, the dislocation structure is obscured by the strongly diffracting ion milling damage which could not be avoided under 2-beam dynamical diffracting conditions.

In contrast to the previous results, data obtained at 550°C show some startling differences (Fig. 6). First, for both conditions, the swelling is now comparable with that observed in the MFE SA 316 SS.[6] Furthermore, the dislocation structures are also rather typical of this material, with a fairly large faulted loop component. Little evidence was found for MC carbide formation in either specimen, although there is some indication of a very low number density at the lower helium level.

It appears that at this lower irradiation temperature the kinetics of MC precipitation are slow relative to those of bubble nucleation and growth. Thus, particularly since the critical radius for the transition from gas-driven to bias-driven growth is small at this temperature,[2] the bubbles are able to reach this size relatively quickly and hence become the dominant vacancy sink. This would further inhibit MC precipitation because the large positive misfit (+70%) of this phase in the austenite matrix necessitates a ready vacancy flux if growth is to proceed. The kinetic factors are obviously also related to the damage rate and lower damage rate experiments are needed to determine if bubble nucleation and growth can be suppressed in favor of carbide precipitation.

It was mentioned earlier that certain microstructural results might be related to materia1 inhomogeneity. This suspicion arose because a very recent experiment performed in an attempt to duplicate the microstructures shown in Fig. 2 failed to do so. The results are presented in Fig. 7. For this repeat specimen, irradiated under conditions identical to those of the previous one, the copious carbide precipitation was not observed and the dislocation structure shows a significant loop component. However, although some cavities are present, the swelling is still low compared to a conventional SA 316 SS sample and subcritical MC particles may be present. Nevertheless, it is obvious that large discrepancies exist between the two specimens and it is believed that local inhomogeneities in Ti, Mo and perhaps C concentrations are responsible for such differences. The second set of data presented in this figure, from a specimen bombarded to 5 dpa, but at the same damage rate, shows a microstructure which suggests that no helium trapping (and thus no MC precipitation) has occurred.

It is now known that this material can be rather heterogeneous with respect to Ti concentration on a small scale because microstructures developed during HFIR irradiation also reflect this problem (Fig. 8). This micrograph shows that although some MC particles are present, generally in the form of stringers, the matrix regions unaffected by MC-helium trapping have gross swelling. It is suggested that the microstructure observed in the previous figure, at 5 dpa, is a manifestation of this problem. Unfortunately, the heterogeneity in chemical composition was introduced during early stages of the thermomechanical processing. The 5 dpa microstructure shown in Fig. 7 may simply be a region between stringers which contained little residual Ti prior to bombardment. Experimental factors are certainly not responsible for the observed lack of reproducibility since similar experiments performed over a three-year period on both 316 SS (unmodified) and 304 SS have shown a remarkable repeatability.

A summary of the microstructural observations is included in Table 2. An important conclusion from the investigation is that, under these experimental conditions, MC carbides effectively suppress swelling when they

TABLE 2 - 316 SS + Ti - MICROSTRUCTURAL OBSERVATIONS

T°C	appm He/dpa	dpa	Irradiation-Induced MC Precipitation	$\Delta V/V_o$	Original MC Precipitation
550	12:1	3	Possible	Quite high	No
550	70:1	3	No	Quite high	No
600	0.2:1	3	Possible	None	Possible
600	12:1	3	Possible	None	Possible
600*	12:1	3	Possible	Quite high	No
600	70:1	3	Copious	Very low	Yes
600	70:1	5	No	High	No
600†	70:1	3	Possible	Quite high	No
700	12:1	3	Acicular Precipitates	Very low	No
700	70:1	3	Some + Acicular Precipitates	Low	Possible

*Repeat experiment performed at a later date.

†Low damage rate experiment — 3 x 10^{-5} dpa/s.

precipitate. Other forms of phase instability, such as acicular precipitates (of the "Ni-Si" variety), Laves phase and $M_{23}C_6$ carbides, were not observed at low doses in this Ti-modified alloy. It is apparent that STEM/EDS analyses are required to determine the chemical compositions of the austenite matrix on a submicron scale to further illuminate the chemical heterogeneity problem and its relationship to the results presented here. Future experiments aimed at further investigations of the helium trapping mechanism will require the more homogeneous and better characterized Path A PCA material.

VI. REFERENCES

1. P. J. Maziasz and E. E. Bloom, ADIP Quarterly Report, DoE/ET/0058/1, August 1978.

2. M. R. Hayns and M. H. Wood, J. Nucl. Mater. 87, No. 1, p. 97 (1979).

3. J. A. Spitznagel, Susan Wood and W. J. Choyke, DAFS Quarterly Report No. 10, April-June (1980).

4. S. Wood, J. A. Spitznagel and W. J. Choyke, DAFS Quarterly Report No. 8, October-December (1979).

5. W. J. Choyke, J. A. Spitznagel, S. Wood, N. J. Doyle, J. N. McGruer and J. R. Townsend, "Implantation Rate Effects on Microstructure," Proceedings of the Symposium on Ion Beam Modification of Materials, Albany, NY, July (1980), to be published in J. Nucl. Instr. & Methods.

6. S. Wood, J. A. Spitznagel, W. J. Choyke, N. J. Doyle, J. N. McGruer and J. R. Townsend, "Microstructural Development in Dual-Ion Bombarded 316 SS," to be published in the Proceedings of the 10th ASTM Symposium on Effects of Radiation on Materials, July 1980, Savannah, GA.

VII. FUTURE WORK

Dual ion studies on the Ti-modified 316 SS used in previous HFIR irradiations will be discontinued because of the inhomogeneous nature of the material. Final experiments on the current program will aim at overlapping ANL damage rates for the completion of the interlaboratory correlation experiment on the MFE 316 SS in the 800°C aged condition.

VIII. PUBLICATIONS

S. Wood, J. A. Spitznagel, W. J. Choyke, N. J. Doyle, J. N. McGruer and J. R. Townsend, "Microstructural Development in Dual-Ion Bombarded 316 SS," to be published in the Proceedings of the 10th ASTM Symposium on Effects of Radiation on Materials, July (1980), Savannah, GA.

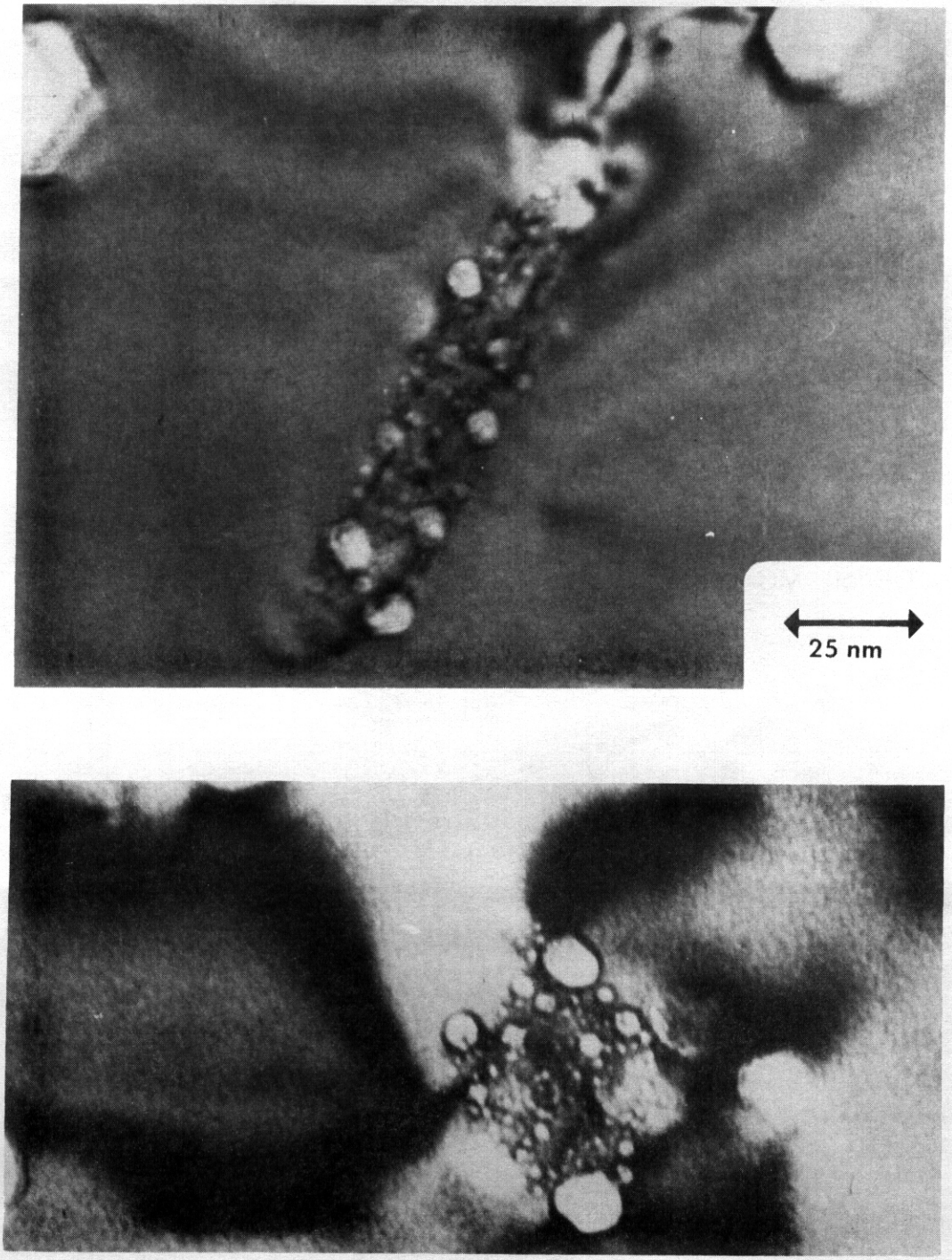

Fig. 1 TEM micrographs of MC carbide particles encrusted with helium bubbles in Ti-modified 316 SS after irradiation in HFIR at 610°C to 57 dpa and 3400 appm helium.

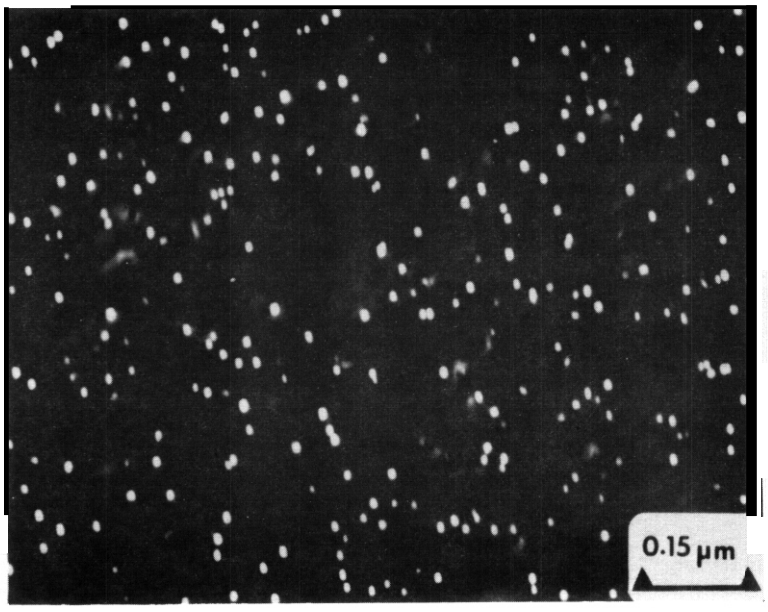

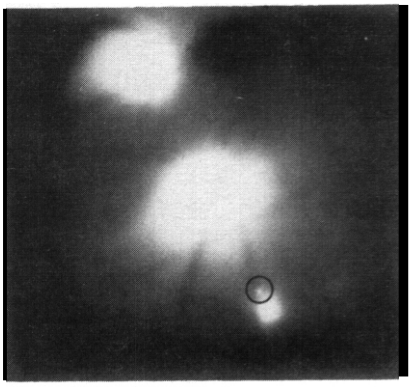

DF of MC carbides

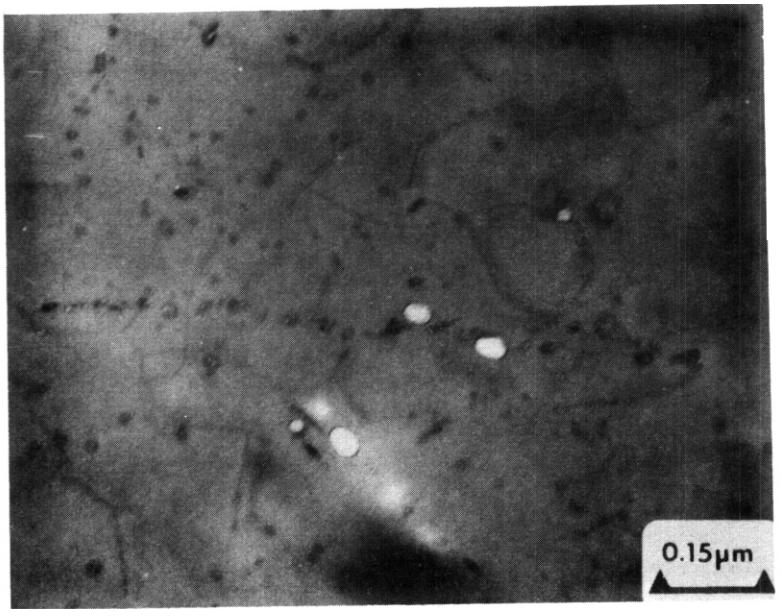

appm He/dpa = 70:1

Bubbles and Precipitates

Fig. 2 TEM micrographs showing copious MC carbide precipitation and bubble nucleation on those carbides in Ti-modified 316 SS dually bombarded at 600°C to 3 dpa and 210 appm helium.

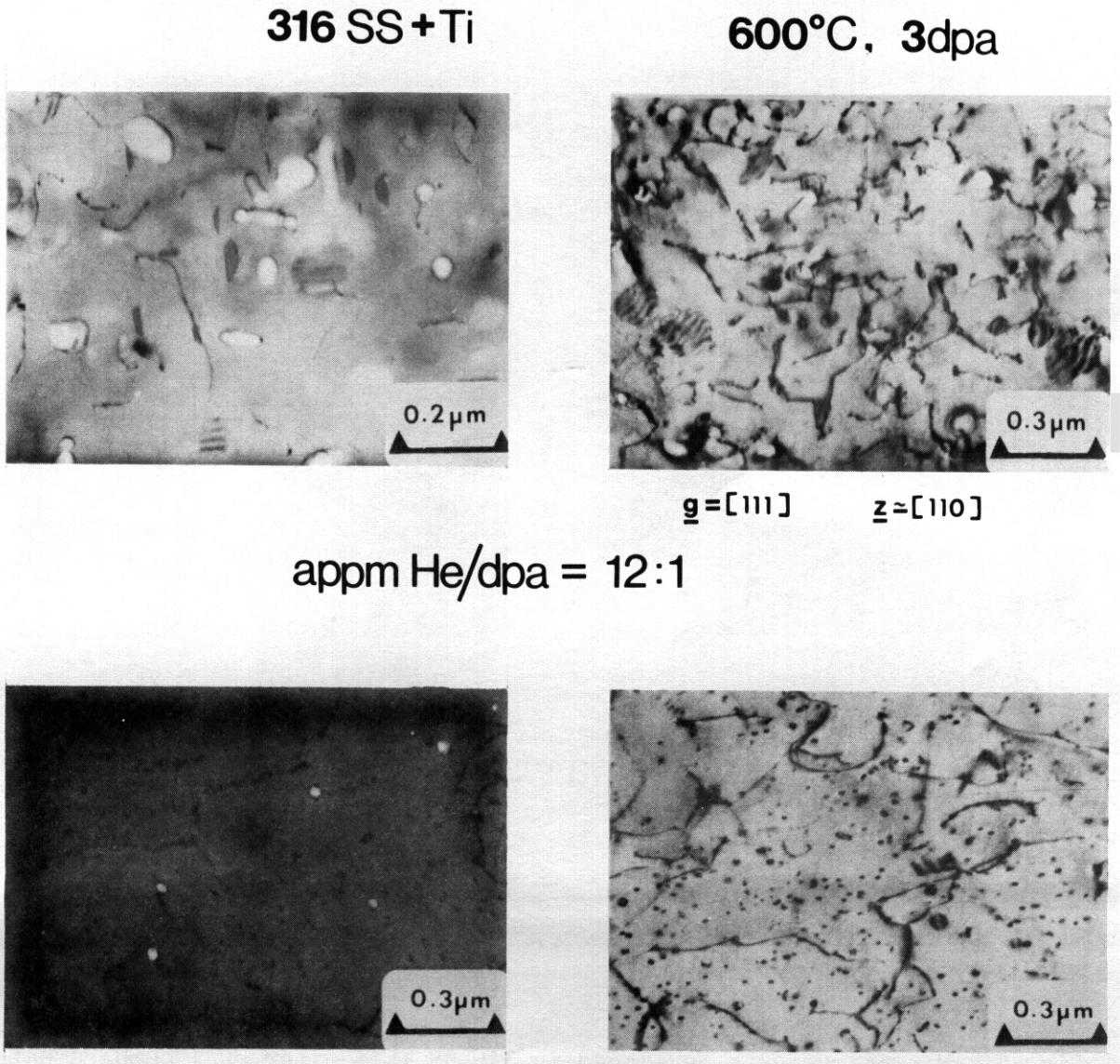

Fig. 3 Comparison of cavity and dislocation structures in Ti-modified 316 SS irradiated to 3 dpa at 600°C. (Note that the apparent cavities in the 12:1 specimen are polishing artifacts.)

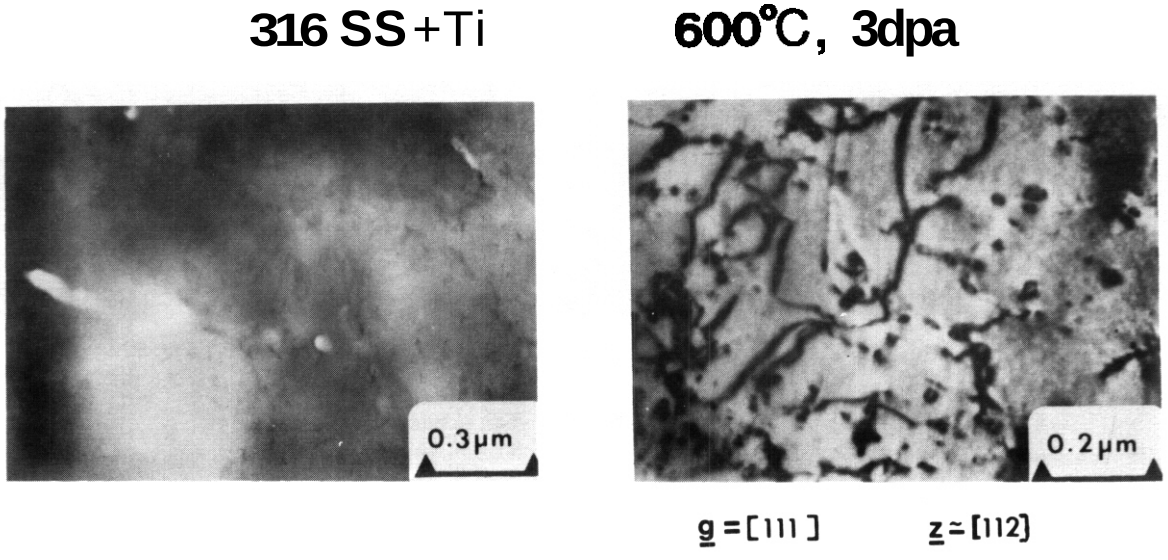

Fig. 4 Microstructures developed in 316 SS **t** Ti after dual bombardment at 600°C (apparent cavities are polishing artifacts).

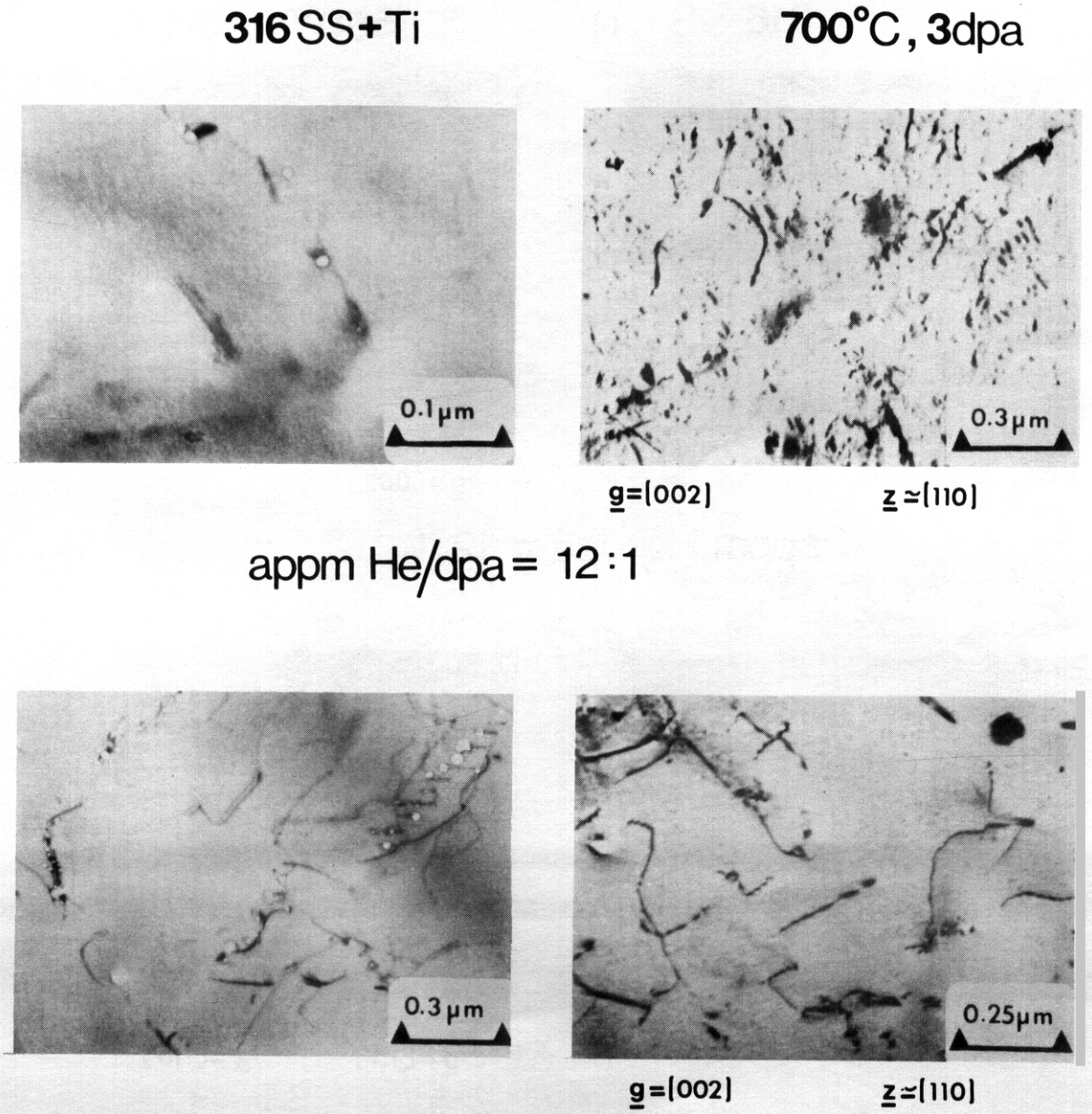

Fig. 5 Comparison of cavity and dislocation structures in Ti-modified 316 SS irradiated to 3 dpa at 700°C. Acicular precipitates appear to be the rod-shaped variant of the MC phase.

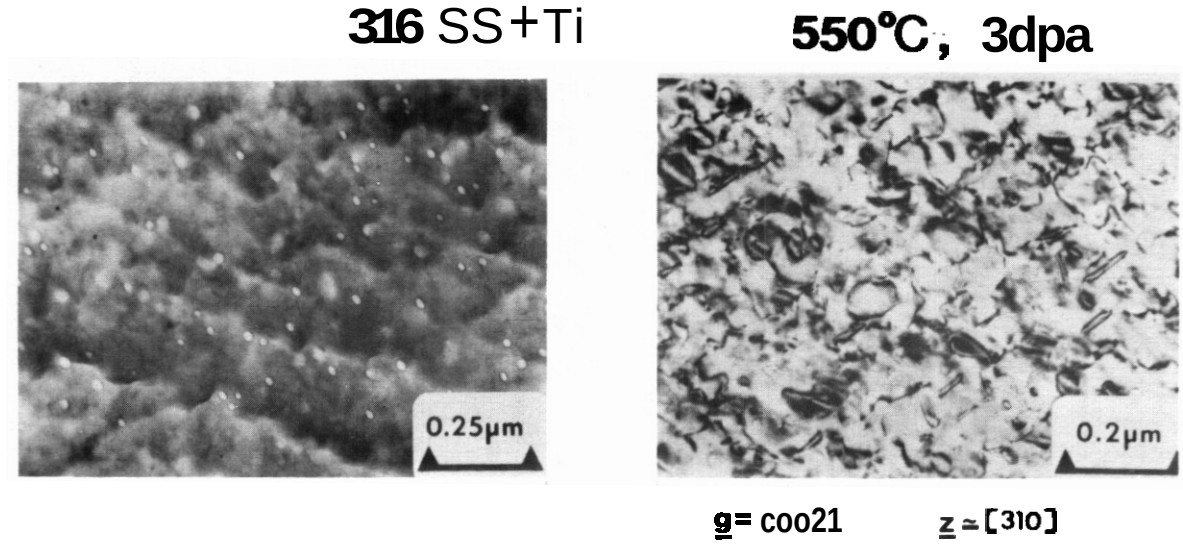

Fig. 6 Typical microstructures developed in Ti-modified 316 SS at 550°C. Note that swelling is comparable with SA 316 SS.

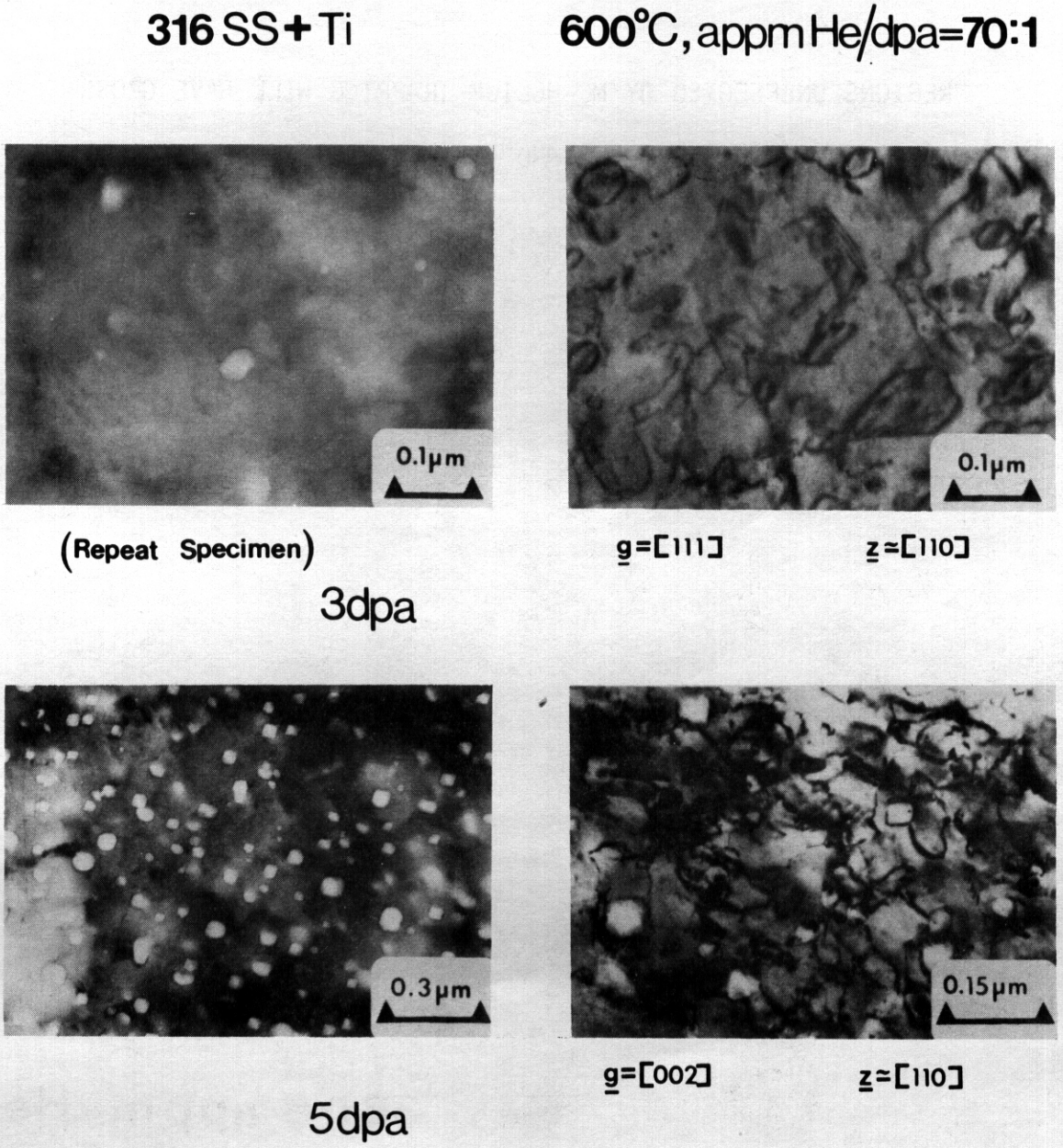

Fig. 7 Absence of MC precipitation and high swelling at 5 dpa suggest an initial chemical inhomogeneity of the base material.

REGIONS UNAFFECTED BY MC-HELIUM TRAPPING WILL HAVE GROSS PHASE INSTABILITY AND CONSIDERABLE SWELLING

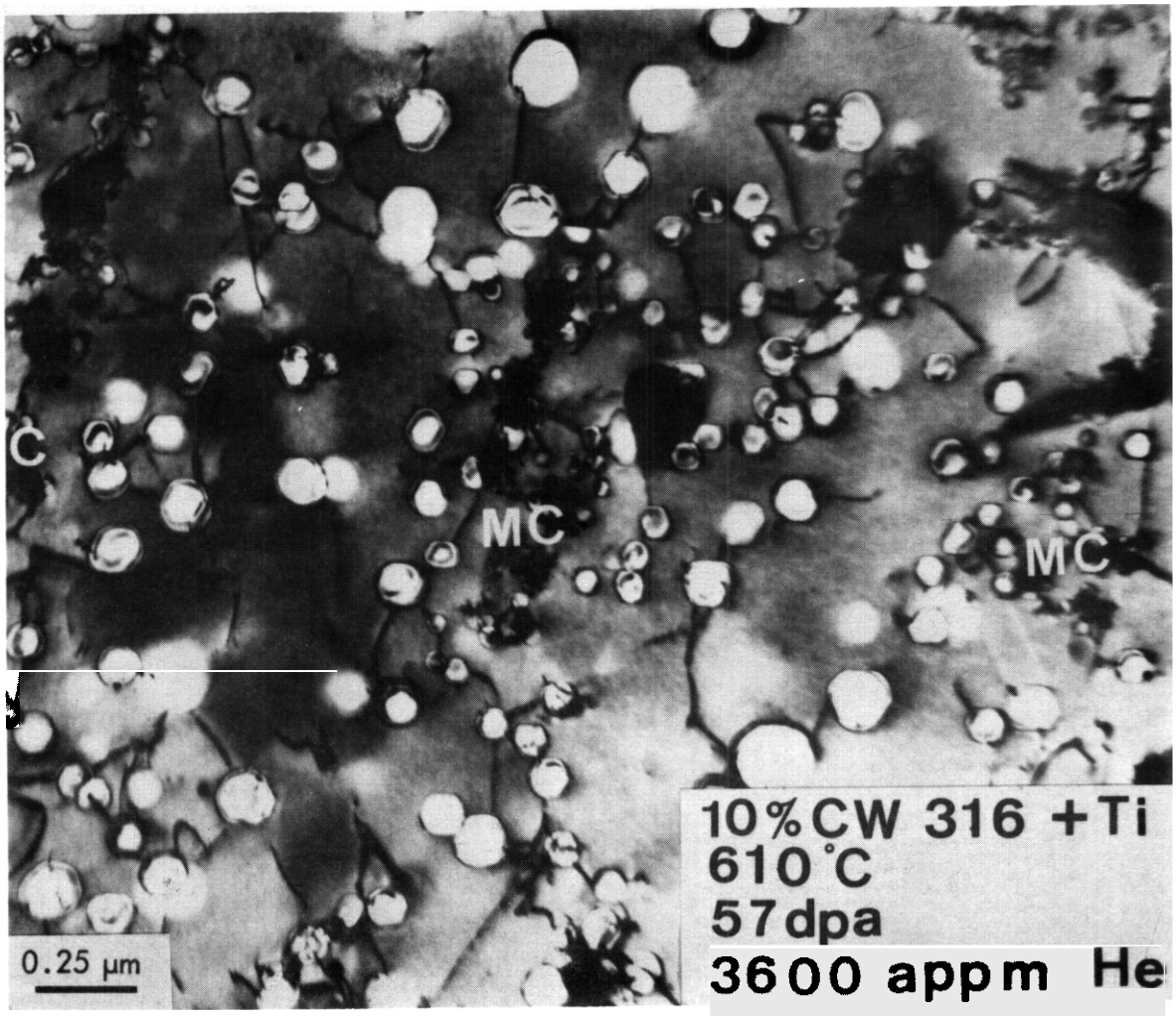

Fig. 8 HFIR irradiated 316 SS + Ti; micrograph indicates the effects of heterogeneous MC carbide formation prior to irradiation. Matrix regions between MC stringers exhibit high swelling and phase instability.

I. PROGRAM

Title: Irradiation Effects Analysis (AKJ)
Principal Investigator: D. G. Doran
Affiliation: Hanford Engineering Development Laboratory (HEDL)

II. OBJECTIVE

The objective of this effort is to develop procedures for predicting swelling in fusion reactor applications.

111. RELEVANT DAFS PROGRAM PLAN TASK/SUBTASK

TASK II.C.2 Effects of Helium on Microstructure

IV. SUMMARY

The difficulties involved in the development of swelling correlations for AISI 316 in fusion environments are discussed. A set of void and bubble-swelling correlations has been developed which incorporates the limited available data from EBR-II and HFIR irradiations. It appears that at high fluences helium may play a minor role in the determination of total swelling over a considerable temperature range.

V. ACCOMPLISHMENTS AND STATUS

A. Development of a Swelling Equation for 20%-CW 316 in a Fusion Device-

F. A. Garner (HEDL), P. J. Maziasz (ORNL), and W. G. Wolfer (U. of Wisc.)

1. Introduction

The development of a swelling equation for any given environment would normally proceed with a data base on the material of interest in the antici-

pated environment. Unfortunately, no such data base exists for AISI 316 stainless steel that can be applied directly to the environment anticipated in the Engineering Test Facility (ETF), where the temperatures are expected to range from 50° to 300°C. Data for the swelling of AISI 316 generally exist only above 270°C, the core inlet temperature of the DFR fast reactor in Britain. The most comprehensive data base has been developed in the U.S. Breeder program and has a lower temperature limit of only 370°C, the core inlet temperature of the EBR-II fast reactor. There is also some data which spans the temperature range 285-780°C from the mixed spectrum reactor designated HFIR (High Flux Isotope Reactor).

Neither the fast reactors nor HFIR match the atom-displacing and helium-producing characteristics of the ETF neutron spectrum. While both types of fission reactors possess much softer neutron spectra than that of fusion devices, the fast reactors produce helium at much lower rates than will ETF, and the HFIR reactor produces more helium (in nickel-containing alloys such as 316).

In order to provide the best estimate of the swelling anticipated in ETF and other fusion devices, one must determine both the influence of neutron spectrum on displacement rate and the effect of helium on swelling, and then extrapolate in some cases to a temperature regime devoid of data. The task is further complicated by the fact that AISI 316 has shown a very strong dependence of swelling on a range of environmental parameters, as well as minor compositional variations and preirradiation thermal-mechanical treatment. Figure 1 demonstrates the variability of swelling behavior in two essentially identical steels irradiated in the breeder reactor program.

It is possible that the steel used in construction of early fusion devices will be similar to that developed for the U.S. Breeder program although other steels such as Ti-modified 316 are being considered. A relation for the swelling of this steel currently exists,[11] but this steel is different

in composition from that employed in the HFIR irradiations. For instance, the DO-heat irradiated in HFIR possesses a larger level of silicon than does the breeder steel, and this element has been shown to have a large effect on swelling. A swelling equation also exists for N-lot steel, which is nominally similar to first core breeder steel, but exhibits a much longer incubation period for swelling.[2]

For the purposes of this study, it will be assumed that the spectral differences between fission and fusion neutron spectra can be adequately described by the use of standardized displacement calculations.[3] It will also be assumed that the range of operational variables in fusion devices will not be significantly different from those of the breeder reactor, and the swelling will therefore be identical in the two devices. (While the first assumption is probably valid, the latter most likely is not, but this issue will be addressed elsewhere).

The most important question is whether the higher helium/displacement ratio found in HFIR leads to significantly different levels of swelling than would occur in the breeder reactors. Although previous analyses of HFIR data concluded that swelling increased with helium level,[4,5] this conclusion is now considered to be incorrect, particularly at fluences greatly above the incubation dose. As shown in Figures 2 and **3,** the only heat of AISI 316 for which both HFIR and EBR-II data exist is the DO-heat. This is an exceptionally sparce data set. The EBR-II data exist at displacement levels which are just above or below the incubation fluence while the HFIR data exist at displacement levels well above the incubation fluences. The swelling rates necessary to bridge the two data fields and normalize the swelling fall at or under that specified in the current design equation.'') In addition, the density measurements shown in Figure 1 are thought to be too high, particularly those in the vicinity of 600-700°C: (These measurements are subject to very large uncertainties and are not supported by microscopy measurements).

Note that the data in Figure 3 suggest a double-peaked (or plateau) swelling behavior with a minimum in the vicinity of 500°C. This behavior is not typical of that of first core heats of this alloy, but has been observed in other heats of AISI 316, particularly in the annealed condition.

Table I contains a compilation of the microstructural and swelling data accumulated for DO-heat irradiated in HFIR. Table II presents a comparison of the swelling data for 20% cold-worked DO-heat with two different swelling correlations shown to fit the first-core steel data equally well. Note that at 460, 550 and 600°C the equations predict greater swelling than indicated by the data. At other temperatures, the data are larger than the predictions. There is a strong indication here that this data field may reflect the heat-to-heat variability of swelling rather than only the influence of helium on swelling. (This possibility will be checked in ORNL examination of HFIR irradiated steels .)

In an attempt to provide insight on the role of helium on swelling, additional fast reactor data were sought. As shown in Table III and Figures 4 and 5, two new data points were secured from DO-heat which originally irradiated to 6.6 x 10^{22} n/cm^2 in one experiment and carried to higher fluence in another experiment. These data suggest that the role of helium in determining the total swelling may not be as large as previously suggested. The larger amount of helium in the HFIR-irradiated material leads to earlier void nucleation and substantially larger void densities at all fluences than observed in EBR-II irradiations. however.

2. Volume Contribution of Equilibrium Bubbles

The possibility may exist that the swelling observed outside the 400-600°C range may be due to bubbles rather than voids. In order to assess this possibility, it is useful to develop an expression for the swelling expected when all the helium produced is assumed to be in equilibrium bubbles filled with either an ideal or non-ideal gas. Therefore, according to the gas law, the pressure in each bubble of volume V is

TABLE I

SWELLING AND CAVITY STATISTICS FOR HFIR-IRRADIATED DO 316

Irradiation Temperature (C°)	Fluence (E>0.1 MeV) n/m² x 10^{26}	dpa	Helium (at. ppm)	Immersion Density $(\Delta\rho/\rho_0)$,%	Cavity Volume Fraction $(\Delta V/V_0)$,%			Diameter Cavity Size (Å)		Matrix Cavity Density (cm^{-3})
					Matrix	Grain Boundary	Total	Matrix	Grain Boundary	
					20% CW 316					
285	---	7.7	390	0.04	0.43	---	0.43	120		3.6×10^{15}
375	---	8.5	380	0.0	0.12	---	0.12	27 870		3.17×10^{16} 1.9×10^{15}
380	7.0	49	3320	1.6	2.1 ± 0.4	--[a]	2.2	95 (1110)[b]	--a	$1.8 \pm 0.4 \times 10^{16}$ (4.5×10^{12})[b]
460	7.7	54	3660	0.8	20 ± 0.4	--a	2.0	170	--a	$6.6 \pm 1.6 \times 10^{15}$
550	6.2	42	2990	~0.0	14 ± 0.1	0.03 ± 0.01	1.43	210	400	$2.4 \pm 0.4 \times 10^{15}$
600[c]	8.7	60	4070	3.3	29 ± 0.5	0.4 ± 0.2	3.3	650	3500	$3.3 \pm 3.0 \times 10^{14}$
680	8.74	61	4140	16.8	60 ± 2.5	2.0 ± 1.0	8.0	1100	7100	$6.5 \pm 2.5 \times 10^{13}$
					SA 316					
480	6.1	42	2950	--	3.0 ± 1.0	--b	3.0	390	--b	$1.4 \pm 0.1 \times 10^{15}$
550	6.2	42	2990	--	3.5 ± 1.5	--b	3.5	500 (1350)[d]	--b	$4.5 \pm 1.5 \times 10^{14}$ (1.2×10^{12})[d]
575	4.2	30	2000	3.9	1.6 ± 0.3	0.1 ± 0.05	1.7	600	1400	$1.6 \pm 0.5 \times 10^{14}$
680	8.74	61	4140	14.1	4.0 ± 1.0	3.0 ± 1.5	7.0	1080	6400	$4.6 \pm 1.2 \times 10^{13}$

[a]Grain boundary precipitation of η and/or τ($M_{23}C_6$).

[b]Large Cavities attached to intragranular η phase particles.

[c]Completely recrystallized into small grains.

[d]Large cavities attached to Laves phase particles.

$$P = \frac{ZnRT}{V} \qquad (1)$$

TABLE II

COMPARISON OF SWELLING PREDICTIONS AND 00-HEAT DATA FROM HFIR

T (°C)	dpa	Total Cavity Volume, %	$-\frac{\Delta\rho}{\rho_o}$, %	PREDICTIONS* MK-8	R=2.92
285	7.7	0.43	0.04	0.0	0.0
375	8.5	0.12	0.0	0.0	0.0
380	49	2.2	1.6	0.014	0.009
460	54	2.0	0.8	4.33	4.57
550	42	1.43	0.0	5.72	4.61
600	60	3.3	3.3	12.27	11.96
680	61	8.0	16.8	0.92	3.0

*The MK-8 equation is the current breeder swelling equation;[1] the R=2.92 equation fits the data just as well but has been reformulated for later incorporation of history effects on swelling.

TABLE III

NEW SWELLING DATA FROM EBR-II IRRADIATIONS

T (°C)	$\phi t/10^{22}$	dpa	$-\Delta\rho/\rho_o$, %	$\Delta v/v_o$, %
500*	6.6	33	-0.1	-0.1
510	13.8	69	9.9	11.0
600*	6.6	33	0.3	0.3
620	15.0	75	6.4	6.8

*These data are rechecks which confirm the original density measurements reported in reference 2.

where Z is the compressibility factor, n is the number of moles of gas, R is the gas constant and T is the absolute temperature, and also

$$p = \frac{2\gamma}{r} \tag{2}$$

where γ is the surface energy and r is the bubble radius. The number of moles can also be defined as

$$n = \frac{C_{He}}{N N_o} \tag{3}$$

where C_{He} is the helium concentration in atoms/cm^3, N_o is Avogadro's number and N is the number of bubbles per cm^3. The gas constant R can also be expressed as $N_o k$, where k is the Boltzmann constant.

The void volume fraction *is* defined as

$$\frac{\Delta v}{v_f} \equiv NV = N\left(\frac{4}{3}\pi r3\right). \tag{4}$$

Combining expressions 1 through 4 leads to the following expression

$$\frac{\Delta v}{v_f} = \sqrt{\frac{3}{4\pi N}} \left(\frac{ZC_{He}kT}{2\gamma}\right)^{3/2} \tag{5}$$

If we assume γ to be 1000 ergs/cm^2 and convert C_{He} to units of appm then

$$\frac{\Delta v}{v_f} = \frac{2.20 \times 10^{-4}}{\sqrt{N}} \left(ZC_{He}^{appm} T\right)^{3/2} \tag{6}$$

Remember that this relation assumes all of the helium to be in bubbles and N is in units of bubbles/cm^3.

3. Evaluation of Swelling Data at 285°C and 7.7 dpa

If it is assumed that the cavities are bubbles and that Z=1.0, then Eqn. 6 predicts $\frac{\Delta V}{V_f} = 3.74 \times 10^{-4}$ or ~0.04% based on the data of Table 11. Therefore, these cavities are either void-like in character or an unrealistically large compressibility[6] of Z = 4.2 is required. (The disparity between the 0.04% measured by immersion density and the cavity volume measurements of 0.43% is not unusual in that a precipitate-related densification on the order of several tenths of a percent usually occurs in these steels.)

It should also be noted that the cavity density for this datum is rather low, since densities greater than 1×10^{16} cm^{-3} were observed at 375-380°C. This is but one illustration of the problems inherent in making comparisons within this data set.

4. Evaluation of Data at 375 and 380°C

At these conditions the steel exhibits bimodal cavity distributions as shown in Table I. If we assume that all helium is in the smaller bubbles at 375°C and 8.5 dpa, then for ideal gas behavior $\frac{\Delta V}{V_f}$ = 0.01% swelling, much less than the observed swelling of 0.12%. This ignores the possibility that any helium is in the large voids. Therefore, we must assume the cavities to be void-like in character.

At the higher fluence of 49 dpa, a similar calculation leads to the conclusion that the smaller bubbles would contribute only 0.5% swelling if they alone contained all of the helium under ideal gas conditions. Once again, the cavities, both large and small, must be considered to be void-like in character. These two data imply a swelling rate on the order of 0.5%/dpa.

While the current U.S. Breeder correlation predicts essentially zero swelling at these conditions, British steel M316 (a nominally similar steel) shows ten swelling values at 45 dpa ranging from 0.6-2.1% swelling at 400°C.[7]

This suggests that the low temperature swelling of AISI 316 is as variable as that at higher temperatures.

5. Evaluation of Data at 680 and 780°C

At 680°C cold-worked DO-heat was measured to have experienced 16.8% density change but only 6-8% cavity volume. (There is considerable uncertainty associated with the early density measurements however.) Equilibrium gas calculations show that 21% volume would be occupied by the gas bubbles ($Z = 1.0$) if they contained all of the gas. It therefore appears that the cavities may indeed be gas bubbles. A similar conclusion was reached for the annealed data at 780°C.

6. Summary of Swelling Data

The available HFIR data cannot be employed to definitively demonstrate a large or clearly observable role of helium in enhancement of swelling, particularly at higher fluences. Therefore, an even smaller role for helium would be expected in ETF. It appears that as long as sufficient cavities are available, the helium can easily be accommodated in the cavities. Conventional wisdom holds that void swelling is confined to some temperature range however, and the helium will eventually agglomerate into bubbles, although the bubbles need not be at equilibrium gas conditions. Therefore, some estimate must be made of the maximum swelling anticipated below 300°C in the ETF and at temperatures above 700°C in other fusion devices.

7. Recommended Nominal Swelling Correlation at all Temperatures

It is recommended that the swelling equation employed in the breeder program for the U.S. Breeder heats of AISI 316 be used at all temperatures, providing it predicts more swelling than that expressed in Equation (6). Otherwise, Equation (6) should be used as illustrated in Figure 6. To obtain a lower estimate of the cavity number density N it is recommended that breeder data

be used. Wolfer and Conn[8] have provided the following expression based on low fluence breeder data.

$$N = C \exp[Q/kT] \quad (7)$$

where $C = 4.16 \times 10^{7}$ cm^{-3}, $Q = 1.05$ eV, $k = 8.6167 \times 10^{-5}$ eV/°K and T is in °K. This expression does not incorporate any dependence on neutron fluence or helium level. It also underpredicts the number of voids observed in HFIR irradiations of 00-heat by a factor of 5-10. Since bubble swelling varies as $N^{-1/2}$ the use of this expression leads to a conservatively large estimate of swelling by a factor of 2-3. For ETF applications below 300°C, this expression predicts unrealistically large void number densities and it is recommended that N be held constant at 5×10^{16} cm^{-3}.

Wolfer has provided calculations of the compressibility factor Z for helium gas at high densities.[6] As shown in Figure 7 the compressibility can be determined from estimates of the packing fraction of the gas in the voids. The upper limit of this quantity is simply the helium atomic volume (assuming all helium to be in the cavities) over the measured cavity volume. In all cases investigated in this study the packing fraction was less than 0.1 and the compressibility factor was 1.3 or less.

8. Conclusions

The DO-heat swelling data cannot be conclusively shown to demonstrate a large role of helium on enhancing the total amount of swelling, particularly at higher fluences. Application of the current breeder equation for first core FFTF steel to fusion environments is therefore probably valid. For those temperature regimes where no swelling is predicted with that correlation, a conservative bubble swelling model has been assumed. The problems inherent in the available data require that additional analysis proceed on materials irradiated in HFIR and EBR-II.

VI. REFERENCES

1. J. F. Bates and M. K. Korenko, "The MK-8 Equation for Stress-Free Swelling of 20% Cold-Worked AISI 316 Stainless Steel," HEDL-TME 80-8 May 1980.

2. J. F. Bates and M. K. Korenko, "Empirical Development of Irradiation-Induced Swelling Design Equation," Nuclear Technology, 48 1980 p. 303.

3. 0. G. Doran, J. R. Beeler, Jr., N. D. Dudey, and M. J. Fluss, "Report of the Working Group on Displacement Models and Procedures for Damage Calculations," HEDL-TME 73-76, Hanford Engineering Development Laboratory, December 1973.

4. P. J. Maziasz, F. W. Wiffen and E. E. Bloom, "Swelling and Microstructural Changes in Type 316 Stainless Steel Irradiated Under Simulated CTR Conditions," ORNL/TM-5396.

5. M. L. Grossbeck and P. J. Maziasz, "The Swelling of 20% Cold-Worked Type 316 Stainless Steel Irradiated In HFIR to Helium Levels of 200-3700 appm," ADIP Quarterly Report DOE/ET-0058/1, August 1978 p. 82.

6. W. G. Wolfer, "High-Density Equation of State for Helium and Its Application to Bubbles in Solids," Proceedings 10th ASTM International Symposium on Effects of Radiation on Material, Savannah, GA June 1980 (in press).

7. J. I. Bramman, et. al., "Void Swelling and Microstructural Changes in Fuel Pin Cladding and Unstressed Specimens Irradiated in DFR." Proceedings of AIME Symposium on Radiation Effects In Breeder Reactor Structural Materials, June 19-23, 1977 Scottsdale, AZ, Eds. M. L. Bleiberg and J. W. Bennett, p. 479.

8. W. G. Wolfer and R. W. Conn, "New Analysis of First Wall Lifetime Considerations for Fusion Reactor," U. of Wisconsin report UWFDM-212, March 1977.

VII. FUTURE WORK

The void and bubble swelling correlations developed in this study will be revised as new data or insight become available. The effect of stress on void and bubble swelling will also be studied and stress-affected swelling correlations developed.

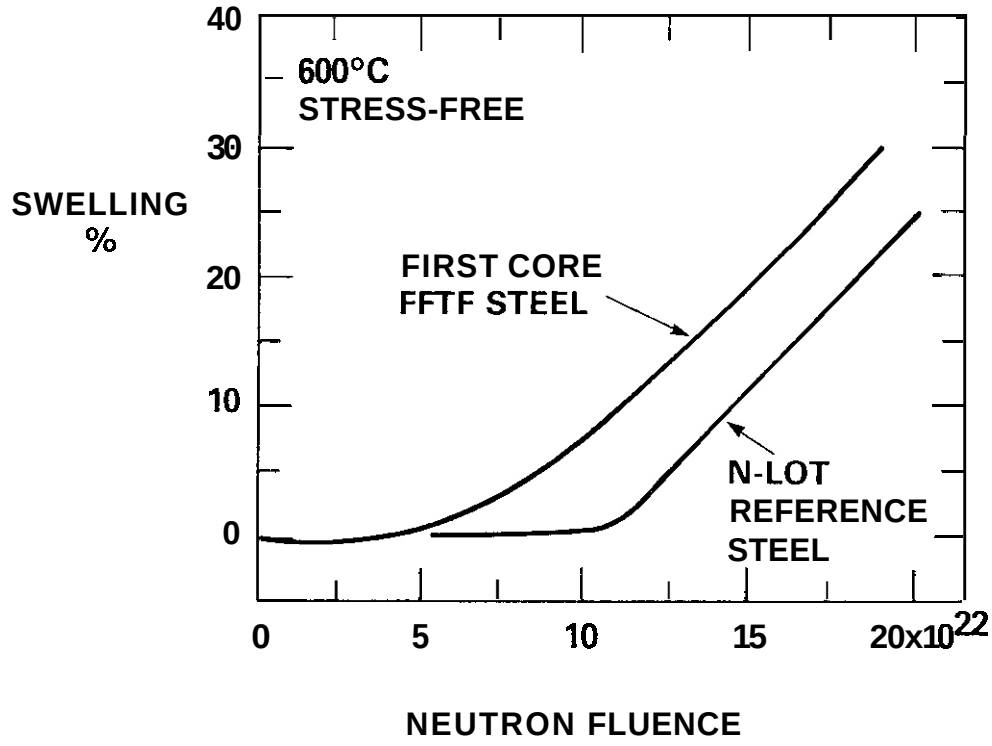

FIGURE 1. Swelling predictions for two nominally identical steels irradiated in the U.S. Breeder Reactor Program(1,2)

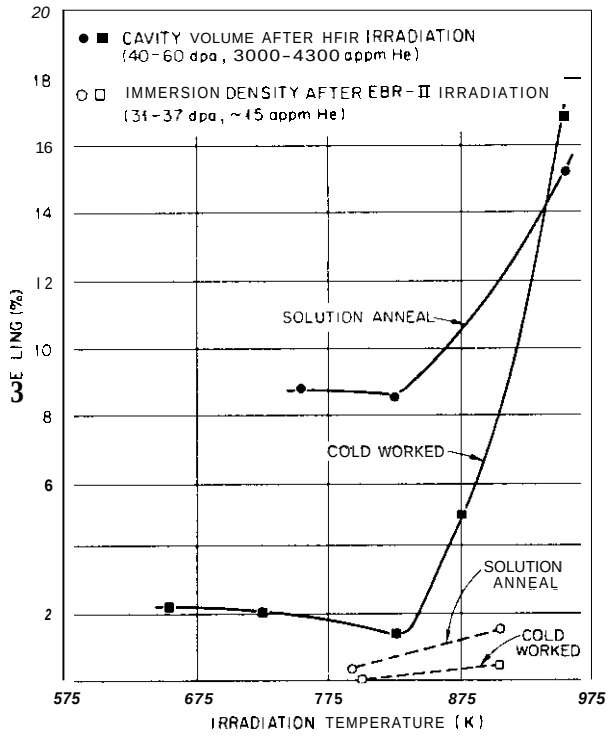

FIGURE 2. Swelling of 20% cold-worked and annealed AISI 316 (DO-heat) irradiated in HFIR and EBR-II.(4)

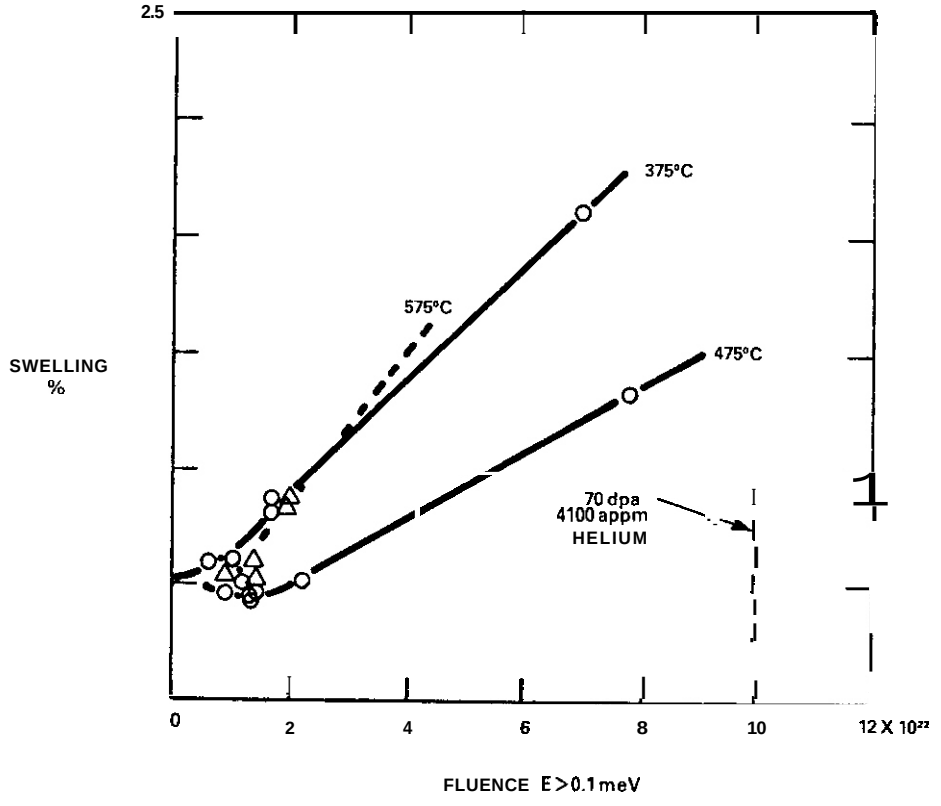

FIGURE 3. Swelling of 20% cold-worked AISI 316 (DO-heat) irradiated in HFIR.[5]

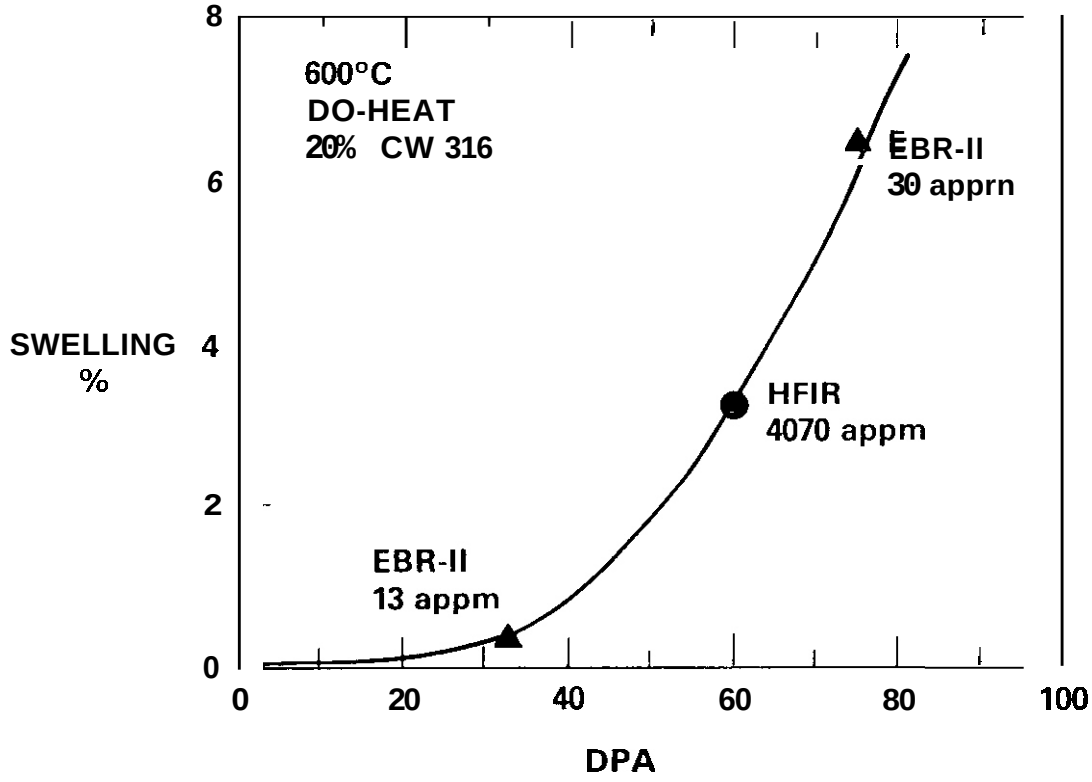

FIGURE 4. Comparison of swelling data on DO-heat at 600°C.

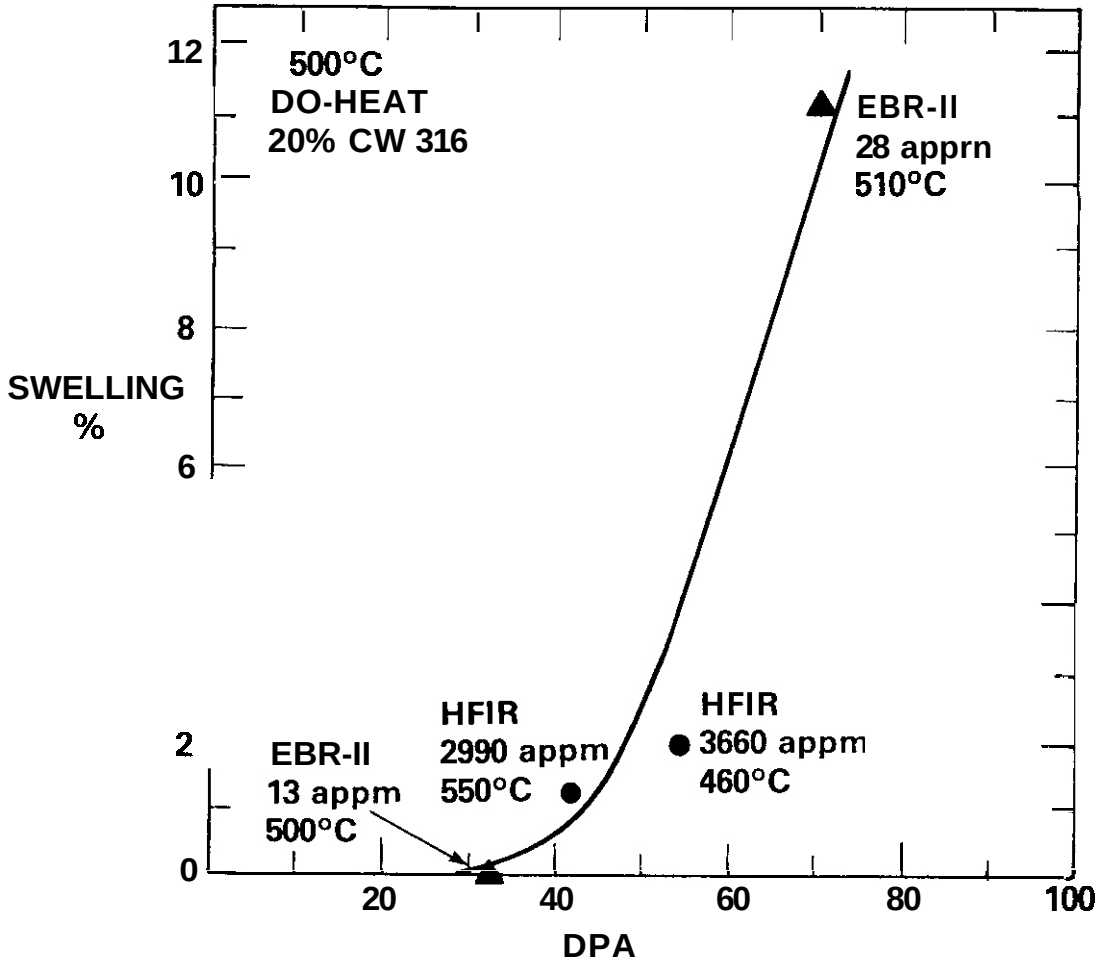

FIGURE 5. Comparison of swelling data on DO-heat at ~500°C.

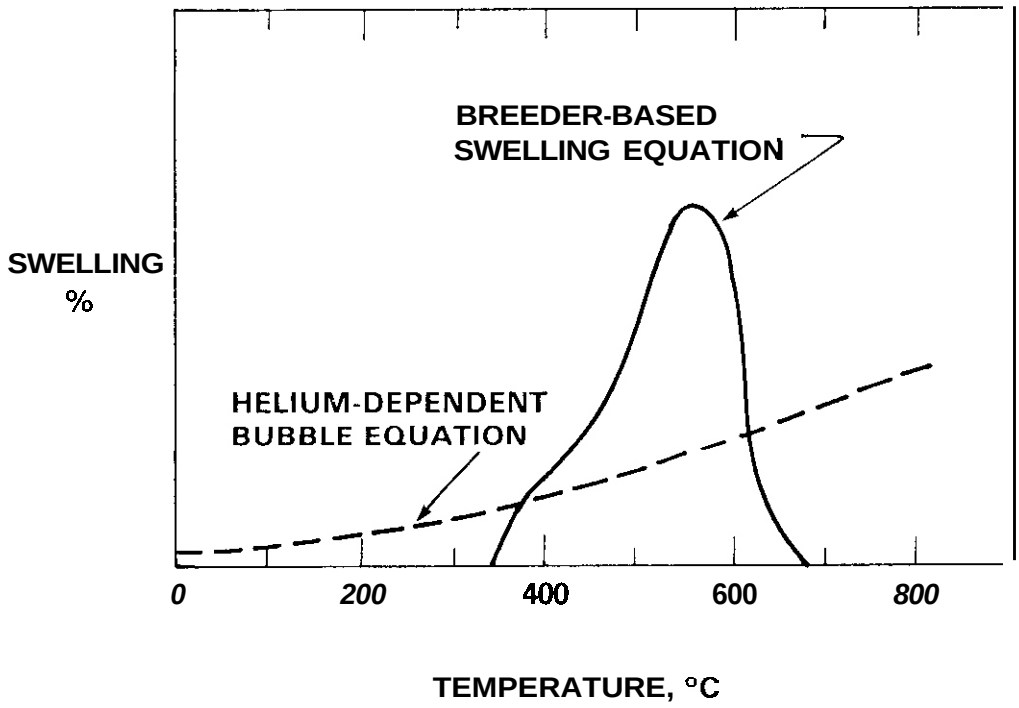

FIGURE 6. Schematic illustration of expected form of bubble and void swelling equations.

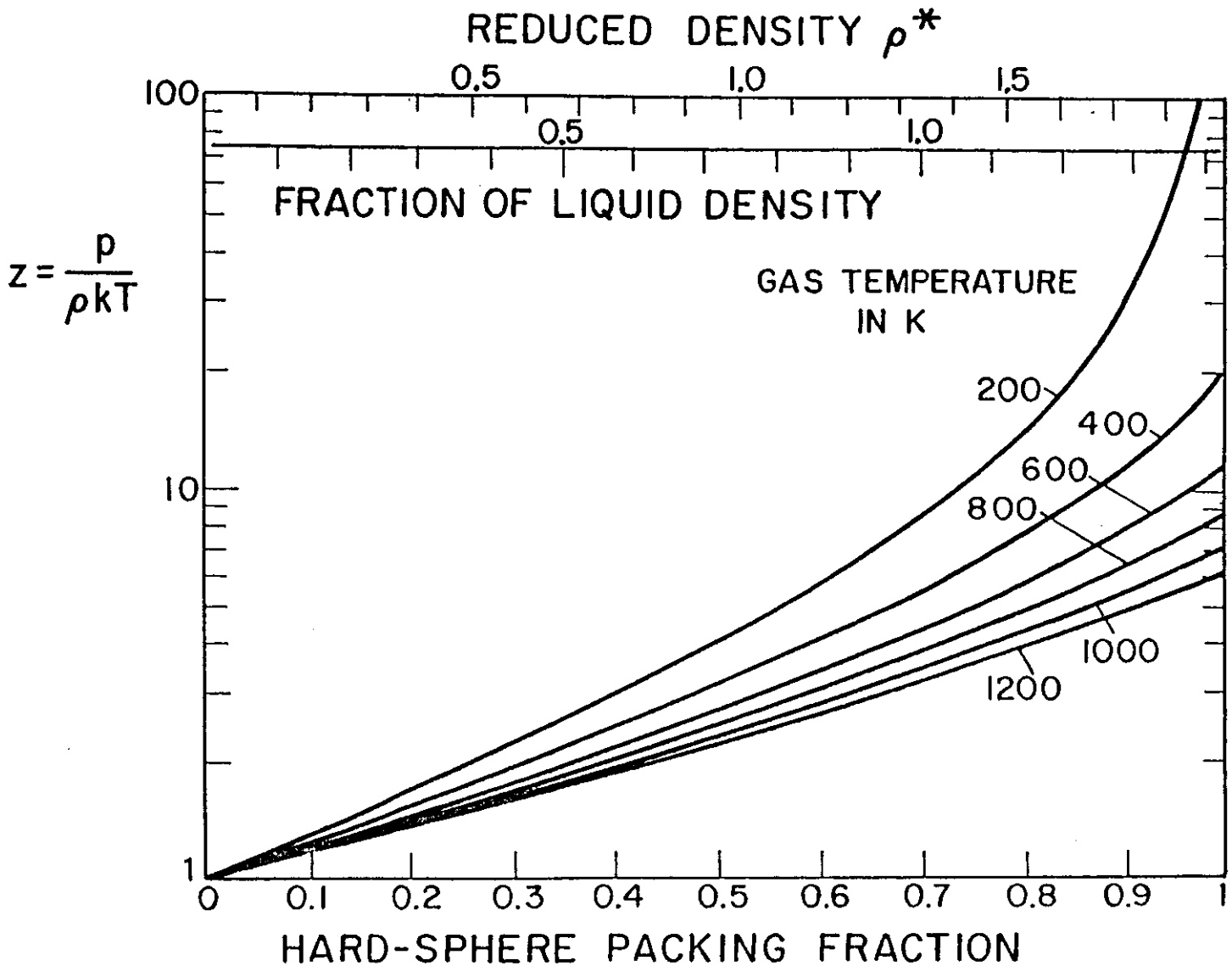

FIGURE 7 Compressibility factor for high density helium reported by Wolfer.[6]

I. PROGRAM

Title: Mechanical Properties

Princpal Investigator: R. H. Jones

Affiliation: Pacific Northwest Laboratory
Operated by Battelle Memorial Institute

II. OBJECTIVE

The purpose of this analysis was to evaluate the microstructure-flow stress relationship for T(d,n) and Be(d,n) neutron and 16 MeV proton irradiated nickel and niobium.

III. RELEVANT DAFS PROGRAM PLAN TASK/SUBTASK

SUBTASK II.C.6.1 Effects of Damage Rate and Cascade Structure on Microstructure-Charged Particle/Neutron Correlations

SUBTASK II.C.II.I
II.C.11.4 Effects of Cascades and Flux on Flow-Light particle irradiations and high energy neutron irradiations

IV. SUMMARY

The flow stress increase of T(d,n) and Be(d,n) neutron and 16 MeV proton irradiated nickel and niobium was shown to be related to the cluster density and diameter using the strong barrier model. The hardening coefficient β was determined to be 4 for both nickel and niobium. This value compares favorably with those reported in the literature for fission neutron irradiated materials, thus giving further support that fusion and fission energy neutrons induce a similar type of displacement damage at low fluences and 25°C.

V. ACCOMPLISHMENTS AND STATUS

Comparison of the flow properties of irradiated nickel and niobium reported previously[1] with more recent microstructural data has been completed. Using the following hardening model

$$\Delta\sigma = 2\mu b/\beta\bar{\ell}$$

where μ is the shear modulus, b the burgers vector, β a constant and $\bar{\ell}$ the average interparticle spacing given by

$$\bar{\ell} = (Nd)^{-1/2}$$

where N is the average cluster density and d is the average cluster diameter the values for β given in Table I were determined. The value of β is independent of irradiating particle but decreases slightly with increasing fluence. Also, values for β were equal for nickel and niobium. Values of β for niobium were determined only for fluences greater than about 1×10^{17} cm^{-2} which was in the cluster hardening regime.. At lower fluences where impurity-point defect complex hardening dominates, the simple hard barrier model does not apply.

Values for β ranging from 2 to 4 have been reported[2-4] for prismatic loop hardening of various materials. Loomis and Gerber[5] report a value of 0.46 for K_1/K_2 obtained from fission neutron irradiated niobium single crystals where

$$\frac{K_1}{K_2} = \frac{1}{\beta K_2} .$$

K_2 equates the effective and average interparticle distances and is a constant close to unity which incorporates geometrical considerations. For $K_2 = 1$, Loomis and Gerber report a $\beta = 2.2$; however, separate values

for K_1 and K_2 were not given. Tucker and Wechsler[6] reported a value of 0.65 for K_1/K_2 which corresponds to a β of 1.5 at $K_2 = 1$. Bajaj and Wechsler[7] found that K_1/K_2 of irradiated vanadium ranged from about 0.36 to 0.45 after an anneal at 100°C for vanadium containing 60 and 640 wt ppm oxygen, respectively. These values correspond to β values of 2.8 and 2.2, respectively for $K_2 = 1$. Comparison of the published values for β with those obtained for T(d,n) and Be(d,n) neutrons and 16 MeV proton irradiated nickel and niobium demonstrates that the hardening mechanism is similar in these cases.

VI. REFERENCES

1. R. H. Jones, Damage Analysis and Fundamental Studies Task Group Quarterly Report, DOE/ET-0005/6, p. 185.
22 S. M. Ohr, R. P. Tucker and M. S. Wechsler, Trans. Japan Inst. of Metals, 9, (1968) 187.
3. R. L. Fleischer, Acta Met., 10 (1962), 835.
4. A. J. E. Foreman, Phil. Mag. 17 (1968) 353.
5. B. A. Loomis and S. B. Gerber, Acta Met. 21 (1973) 165.
6. R. P. Tucker and M. S. Wechsler, Rad. Effects, 3 (1970) 73.
7. R. Bajaj and M. S. Wechsler

TABLE 1. **Microstructure-Yield Strength Comparison for T (d,n), Be (d,n) and 16 MeV Proton Irradiated Material**

MATERIAL	PARTICLE	FLUENCE cm^{-2}	β	REFERENCE
NICKEL	T (d,n)	2×10^{17}	4.0	BATTELLE
	Be (d,n)	3×10^{17}	4.2	
		6×10^{17}	3.8	
		1×10^{18}	3.2	
	16 MeV H^+	6×10^{17}	4.6	
		2×10^{18}	3.8	
NIOBIUM	T (d,n)	1×10^{17}	3.4	
	16 MeV H^+	7×10^{17}	4.2	
		2×10^{18}	3.4	
NIOBIUM	FISSION n	3×10^{19}	2.2	LOOMIS AND GERBER
NIOBIUM	FISSION n	4×10^{18}	1.5	TUCKER AND WECHSLEF
VANADIUM	FISSION n	10^{19}	2.9	BAJAJ AND WECHSLER

POLYCRYSTAL $\Delta\sigma = 2\mu b/\beta\bar{\ell}$ $\bar{\ell} = (Nd)^{-1/2}$

I. PROGRAM

Title: Irradiation Effects Analysis (AKJ)
Principal Investigator: D. G. Doran
Affiliation: Hanford Engineering Development Laboratory

II. OBJECTIVE

The purpose of this study is to obtain tensile properties data on metals and alloys irradiated with fusion neutrons for comparison with data obtained with fission neutrons. Data from microtensile specimens will be correlated with microstructural and mechanical properties data from TEM discs.

111. RELEVANT OAFS PROGRAM TASK/SUBTASK

TASK II.C.6 Effects of Rate and Cascades on Microstructures.
II.C.II Effects of Cascades and Flux on Flow.

IV. SUMMARY

Tensile tests have been completed on 316 SS microtensile speciemns irradiated at RTNS-II to a peak fluence of 1.1 x 10^{18} n/cm^2 at room temperature. Evidence was found for the onset of irradiation hardening for the two conditions of 316 SS investigated in this experiment. No change from the unirradiated tensile properties for these specimens was observed for the specimens tested which had the lowest dose (0.6 x 10^{17} n/cm^2).

V. ACCOMPLISHMENTS AND STATUS

A. Tensile Properties Data on 316 SS Irradiated at RTNS-II - R. J. Puigh and N. F. Panayotou (HEDL)

1. Introduction

Radiation damage of structural materials due to their exposure to high energy neutrons is an important consideration in the design of fusion power plants. Our current understanding of radiation damdge is

not sufficient to extrapolate our broad base of fission reactor irradiated data to the effects of high energy neutron irradiations upon structural materials. Therefore, data involving high energy neutron irradiations is required. Currently the only sources of high energy neutrons for materials testing have relatively small irradiation volumes and large flux gradients within this volume. To irradiate a statistically meaningful number of specimens in this limited volume, miniaturized specimens become necessary.

2. Experiment

Details of the specimen geometry and the miniature tensile machine used for testing have been reported previously.[1] The chemical composition of the 316 SS used in the fabrication of the specimens is given in Table 1. Specimens of 316 SS in both the 20% cold worked and annealed (975°C/15 min/AC) conditions were included in the HEDL-4 experiment which was irradiated at room temperature in RTNS-II. The specimen holder for this experiment is shown in Figure 1. Each of the three microtensile specimen holders contained 35 tensile specimens and 10 Marz grade niobium dosimetry wires. These dosimetry wires have been analyzed by LLL to determine the neutron fluence distribution within each microtensile specimen holder.

N	Al	C	Mn	P	S	Si	Ni	Cr	Mo	Nb	Ti	Cu	B	Fe
0.006	0.01	0.05	1.5	0.01	0.009	0.5	13.5	16.6	2.4	0.03	0.002	0.08	0.001	BAL.

3. Experimental Results

The results of testing the 316 SS microtensile specimens are summarized in Table 2. The average values for the tensile properties of the unirradiated specimens are given for zero fluence. The uncertainty quoted in Table 2 for these unirradiated tensile properties is the standard deviation in the average value of these properties. For the 20% cold worked 316 SS the average values for the tensile properties is based on 17 tensile tests and for the annealed 316 SS the average values for the tensile properties

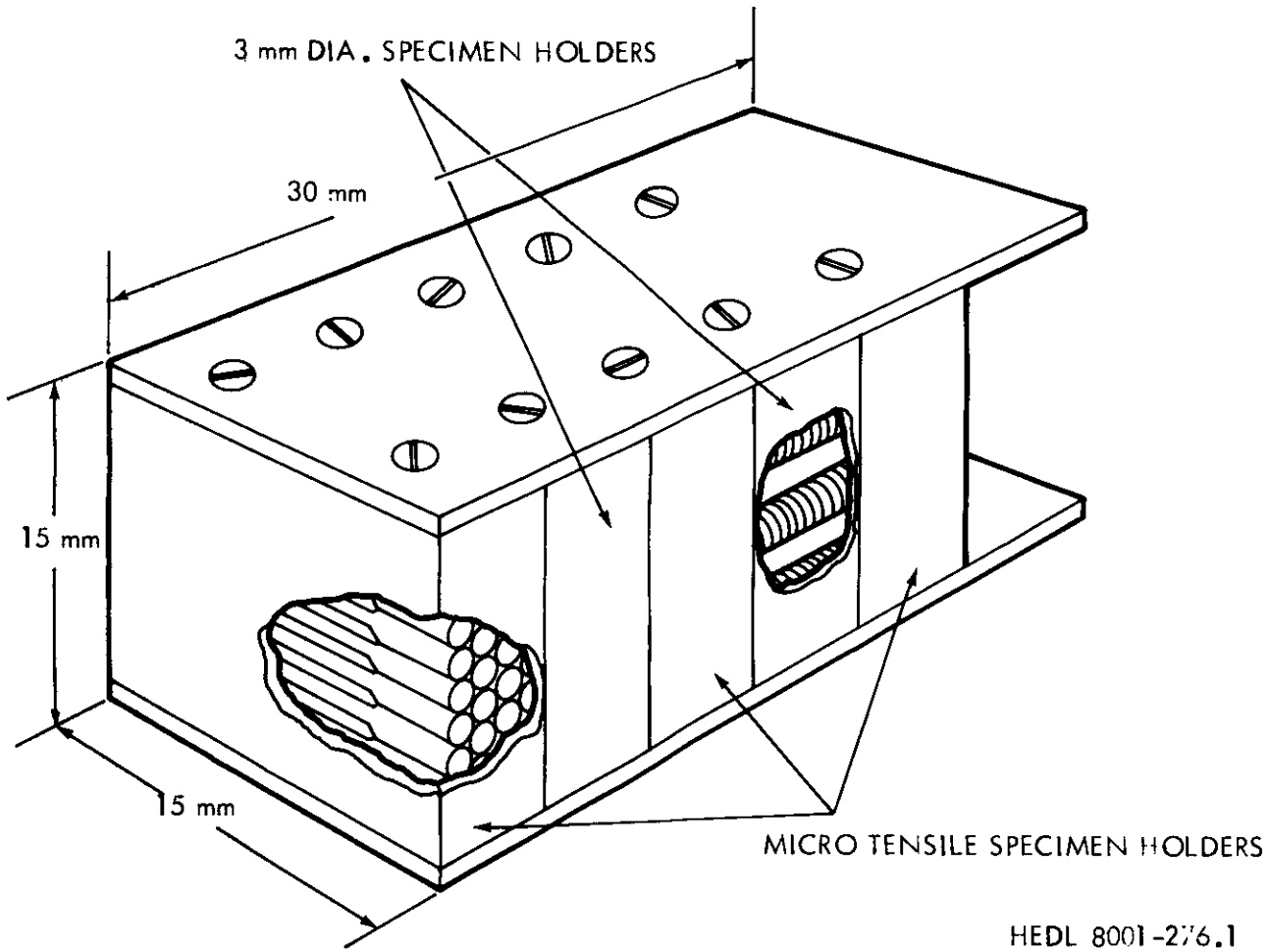

FIGURE 1. Specimen Holder for the HEDL-4 Experiment.

TABLE 2

SUMMARY OF THE TENSILE PROPERTIES OF T(d,n) IRRADIATED 316 SS

20% Cold-Work				Annealed (975°C/15 min/AC)			
Fluence ($\times 10^{17}$ n/cm^2)	0.2% YS (MPa)	UTS (MPa)	Total El. (%)	Fluence ($\times 10^{17}$ n/cm^2)	0.2% YS (MPa)	UTS (MPa)	Total El (%)
0	633 ± 19 (3%)	713 ± 12 (2%)	33 ± 8 (25%)	0	284 ± 21 (7%)	594 ± 12 (2%)	67 ± 12 (18%)
0.55	635	700	32	0.55	296	590	78
0.59	636	708	29	0.56	288	578	60
0.62	644	711	23	0.59	299	580	63
0.64	645	709	26	0.64	290	571	103
1.4	644	727	30	1.5	320	604	59
1.7	628	712	29	1.7	305	568	51
1.7	667	725	19	1.7	324	604	50
1.7	660	721	29	1.8	318	581	57
1.8	663	724	28	6.5	406	605	50
6.6	702	732	18	6.6	379	620	44
7.4	735	760	24	7.5	382	614	58
7.6	723	749	18	9.4	366	594	50
10.2	696	731	17	11.5	412	623	55

YS - Yield Stress: UTS Ultimate Strength: Total El E

is based on 25 tensile tests. The values for the tensile properties for a given, non-zero fluence are based on a single test and the uncertainty for a specific tensile property is estimated to be equivalent to the percentage uncertainty for this property which is given for zero fluence.

Figure 2 shows the change in the yield stress and ultimate tensile strength for 20% cold worked (CW) 316 SS as a function of neutron fluence. For 20% CW 316 SS the ultimate tensile strength increases slightly as a function of increasing fluence and the yield stress increases by approximately 13% at the highest fluence. At the fluence of 0.6×10^{17} n/cm^2 no change in either the ultimate tensile strength or the yield stress is observed. The yield stress and ultimate tensile strength are indicated at zero fluence on the figure.

Figure 3 shows the change in the yield stress and ultimate tensile strength for annealed 316 SS. The ultimate tensile strength increases slightly with increasing fluence and the yield stress increases by approximately 37% at the highest fluence. Again at the fluence 0.6×10^{17} n/cm^2 no change in these tensile properties is observed.

The results of measurements of total elongation are also listed in Table 2. The fractional uncertainty in these measurements is 0.25 for the cold worked and 0.18 for the solution annealed material. Because of these large uncertainties we can only say that the total elongation for both the 20% CW and the annealed 316 SS shows a general decrease in its value as a function of increasing fluence as expected.

4. Discussion

Jones et. al[2] investigated the tensile properties of annealed 316 SS irradiated with neutrons from the Be(d,n) reaction. They observe no change in the ultimate tensile strength up to the peak fluence of 1×10^{18} n/cm^2. However, the yield stress increased by 16% and the total elongation decreased by 26%. Our results are consistent with theirs for the ultimate tensile strength and total elongation. However, we observe a significantly larger increase in the yield stress, 37%.

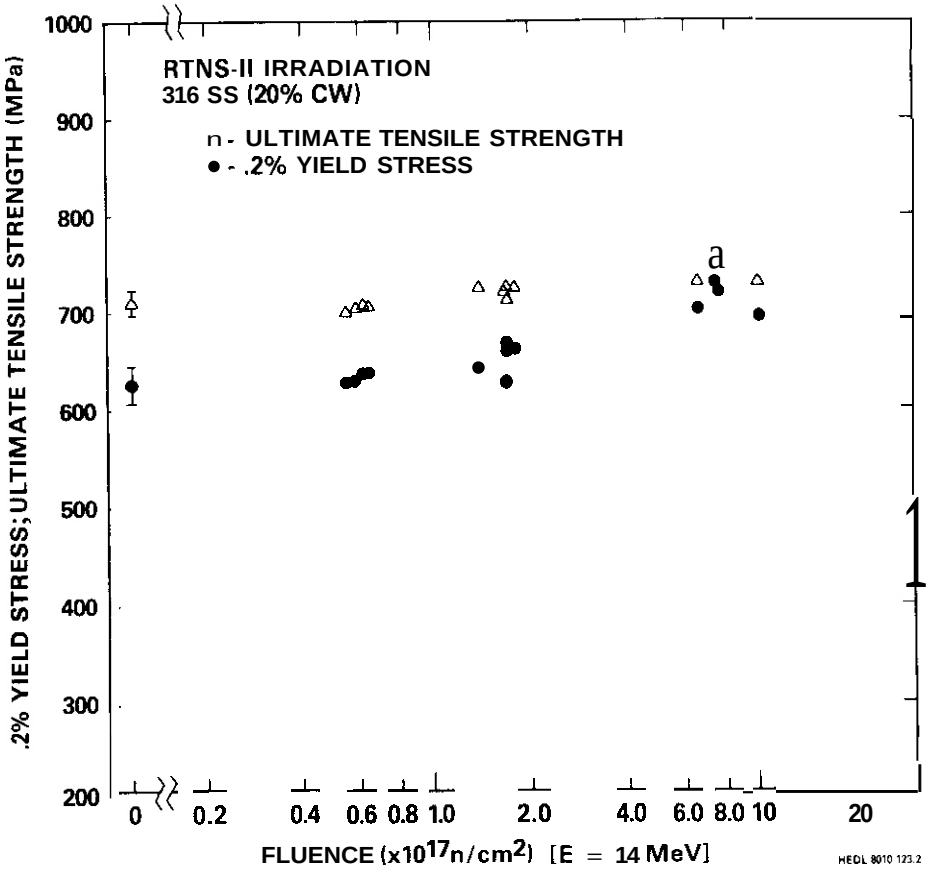

FIGURE 2. Yield Stress and Ultimate Tensile Strength as a Function of Fluence for 20% CW 316 SS.

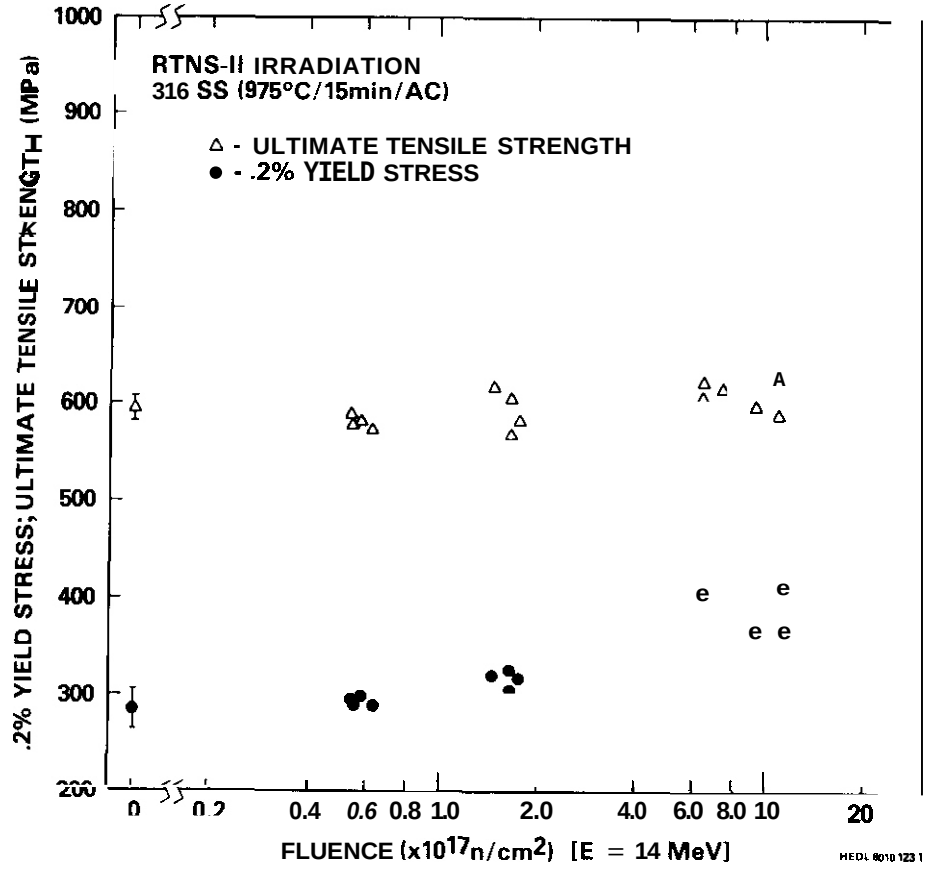

FIGURE 3. Yield Stress and Ultimate Tensile Strength as *a* Function of Fluence for Annealed 316 SS.

5. Conclusions

The onset of irradiation hardening in both the 20% CW and annealed conditions of 316 SS occurs for fluences greater than 0.6 x 10^{17} n/cm^2 for 14 MeV neutron irradiated specimens tested and irradiated at room temperature. The changes in the tensile properties produced in both conditions of 316 SS irradiated to a fluence of 10^{18} n/cm^2 are summarized below:

a. Slight increase in the ultimate tensile strength;

b. Significant increase in the yield stress ; and

c. A small decrease in the total elongation.

VI. REFERENCES

1. R. J. Puigh, R. E. Bauer, and E. K. Opperman, "Miniature Tensile Testing of 316 SS," ADIP Quarterly Progress Report, September 30, 1980.

2. R. H. Jones, D. L. Styris, E. R. Bradley, L. R. Greenwood, and R. R. Heinrich, "Microstructure and Tensile Properties of T(d,n) and Be(d,n) Neutron Irradiated Nickel, Niobium and 316 SS," J. of Nucl. Mat. 85 & 86, 889 (1979).

VII. FUTURE WORK

A determination will be made of the reduction in area for these specimens. Microhardness testing of the microtensile specimens and correlation of hardness and tensile data is also planned. The HEDL-4 experiment also contained Marz grade nickel specimens in the annealed condition; and results from their testing will be given in the next reporting period.

I. PROGRAM

Title: Irradiation Effects Analysis (AKJ)
Principal Investigator: D. G. Doran
Affiliation: Hanford Engineering Development Laboratory (HEDL)

II. OBJECTIVE

The objective of this effort is to modify irradiation creep correlations developed from fast breeder and thermal reactor data for fusion reactor applications.

III. RELEVANT OAFS PROGRAM PLAN TASK/SUBTASK

TASK II.C.2.4 Modeling
TASK II.C.2.14 Models of Flow and Fracture Under Irradiation

IV. SUMMARY

A correlation has been developed describing the anticipated irradiation creep behavior of 20% cold-worked AISI 316 in fusion environments. It incorporates low temperature fast breeder and thermal reactor data to extend the existing breeder correlation to the temperature range of the proposed Fusion Energy Device. It also includes a dependence on displacement rate not currently incorporated in the corresponding breeder correlation.

V. ACCOMPLISHMENTS AND STATUS

A. Development of an Irradiation Creep Correlation for 20% Cold-Worked AISI 316 In Fusion Environments - E. R. Gilbert and F. A. Garner (HEDL)

1. Introduction

As shown in Figure 1 the irradiation creep behavior of nominally similar steels has been observed to be quite variable. It is anticipated that the Fusion Energy Device (FED) and possibly other early fusion devices will be constructed of 20% cold-worked AISI 316 stainless steel of a composition and specification which are identical to that currently employed in the construction of Fast Flux Test Facility (FFTF) core components. It is therefore assumed that the current creep correlation for this steel can be modified and/or extrapolated to the conditions expected in such devices.

Development of a fusion-creep correlation requires that the existing breeder correlation be extended to cover the full range of anticipated temperatures and that corrections be made for the differences in both the displacement and transmutation characteristics of the breeder and fusion reactors.

2. Neutron Spectral Effects

In the development of the fusion-creep correlation it has been assumed that transmutation products other than helium do not influence the irradiation creep behavior. There is no evidence to support or refute this assumption. While there is no data yet available on the effect of helium on irradiation creep, it is anticipated that the large levels of helium generated in fusion reactor materials may be a major factor in the material response. However, no dependence of creep on helium level will be incorporated into the correlation effort until data become available from irradiation of creep tubes in mixed spectrum reactors.

The displacement characteristics of breeder and fusion reactor neutrons are expected to be different. It is assumed that these differences are adequately described by expression of the exposure dose in displacements per atom, calculated in the standard manner.[1] Therefore, 1.0×10^{23} n/cm^2 (E >0.1 meV) in EBR-II yields 50 dpa in AISI 316.

3. Extrapolation to FED Temperature Range

Whereas the data used to develop the current breeder correlation were derived at temperatures between 370 and 700°C, FED is expected to operate in the range of 50 to 300°C. As shown in Figure 2, Gilbert had earlier reported that in this temperature range irradiation creep would exhibit an inverse dependence on temperature.[2] (Use of the current correlation in this temperature range would predict no dependence on temperature.) This trend has since been confirmed by several groups on a wide variety of alloys and metals. (3.4)

The temperature dependence employed to develop the fusion-creep equation is identical to that shown in Figure 2. As shown in Figure 3 the low and high temperature portion of the equation were joined by normalizing to creep data published by Mosedale[5] on the creep of cold-worked M316 in the DFR fast reactor at 250°C.

4. Flux-Dependence of Creep

Lewthwaite and Mosedale[6.7] have published creep data on 300 series stainless steels and other alloys which demonstrate a strong dependence on displacement rate in the DFR fast reactor at temperatures below 400°C. As shown in Figure 4 the steady-state creep rate increases with decreasing displacement rate. This dependence has been incorporated into the fusion-creep correlation. The equation appears to also adequately describe the creep behavior of several austenitic and other steels irradiated in thermal reactors at very low displacement rates. In this case Foster and Boltax[8] saw flux-related enhancements of roughly a factor of 2.5, while the equation predicts a factor of 3.2.

Based on conclusions reached by Gurol and Garner,[9] no dependence has been included on the flux pulsing anticipated to be characteristic of fusion devices.

5. Equation Description

The recommended equation is:

$$\bar{\varepsilon} = A_i(1 - e^{-F/2})\,\bar{\sigma} + B_o F\,\bar{\sigma} G(T)\,H(\dot{F}) + C_1(F/\dot{F})^{0.5}\,\bar{\sigma}^{4.5}$$

$$+ C_2\,\{\sinh(\frac{\bar{\sigma}}{\sigma_1 H})\}^3\,(F/\dot{F})^3 + \frac{B_1}{B_2}\,\Omega^2\,\ell n\,(\cosh(H(\dot{F})\,F/\Omega))\bar{\sigma}$$

where

$\bar{\varepsilon}$ = effective strain, %

$\bar{\sigma}$ = effective stress (MPa)

F = displacement level in dpa

T = temperature, °K

$A_1 = 2 \times 10^{-4}$ %/MPa for biaxial loading (i = 1)

$A_2 = 4 \times 10^{-4}$ %/MPa for bending (i = 2)

$B_o = 1.5 \times 10^{-4}$

$G(T) = EXP\,(2 - 0.003\,T)$

$H(\dot{F}) = EXP\,[a - b(\dot{F}/(6 \times 10^{-7}))]$

$\dot{F}$ = displacement rate in dpa/s

a = 1.22

b = 1.46

$C_1 = \exp(-5.5 - 24000/T)$

$C_2 = \exp(52.25 - 95000/T)$

$B_1 = \exp(1.0 - 8052/T)$

$B_2 = 1 + \exp(45 - 40{,}266/T)$

Ω = 45 dpa

$H = 1 + (F/5)^{0.5}$

σ_1 = 47.76 MPa

With the exception of the H(F) and G(T) terms, this equation is similar in form to the breeder equation and includes terms for the primary transient, steady state creep (and its eventual acceleration) and thermal creep. Due to the substantial uncertainties involved in the development of this equation, no realistic uncertainty limits have yet been established.

Figures 5 and 6 demonstrate the predicted behavior of this alloys as a function of temperature, fluence and neutron flux. Figure 5 describes the anticipated behavior with displacement level and closely resembles the predictions of the breeder correlation at breeder-relevant displacement rates. Figure 6 illustrates a potential problem at high temperatures (>450°C) however. Our current understanding of flux effects would not lead to the prediction that the magnitude of creep at intermediate temperatures would be quite so sensitive to temperature. It is anticipated that the form of the flux dependency will have to be changed. This alteration will be formulated and reported in the next reporting period.

VI. REFERENCES

1. D. G. Doran, J. R. Beeler, Jr., J. D. Dudey, and M. J. Fluss, "Report of the Working Group on Displacement Models and Procedures for Damage Calculations," HEDL-TME-73-76, Hanford Engineering Development Laboratory, December 1973.

2. E. R. Gilbert, "Reactor Technology," 14(3), 253 (1971).

3. R. A. Wolfe and B. Z. Hyatt, J. Nucl. Mat. 45 (1972/1973) 181-194.

4. A. R. Causey, G. J. C. Carpenter and S. R. MacEwen, J. Nucl. Mat. 90 (1980) 216-223.

5. D. Mosedale, 0. R. Harries, J. A. Hudson, G. W. Lewthwaite, and R. J. McElroy, "Irradiation Creep in Fast Reactor Structural Materials," Radiation Effects in Breeder Reactor Structural Materials, AIME, Eds. M. L. Bleiberg and J. W. Bennett, 209 (1977).

6. G. W. Lewthwaite and D. Mosedale, "The Effects of Temperature and Dose Rate Variations on the Creep of Austenitic Stainless Steels in the Dounreay Fast Reactor," J. Nucl. Matls. 90, (1980), 205.

7. G. W. Lewthwaite and D. Mosedale, "Irradiation Creep of Nimonic PE16 Alloy in the Dounreay Fast Reactor," Proceedings, Irradiation Behavior of Metallic Materials for Fast Reactor Core Components, Ajaccio, Corsica (June 1979).

8. J. P. Foster and A. Boltax, J. Nucl. Mat. 89 (1980) 331-337.

9. H. Gurol and F. A. Garner, "Effect of Irradiation Pulsing on the SIPA Creep Mechanism," this report.

VII. FUTURE WORK

This equation will be reformulated and improved as additional information or insight becomes available.

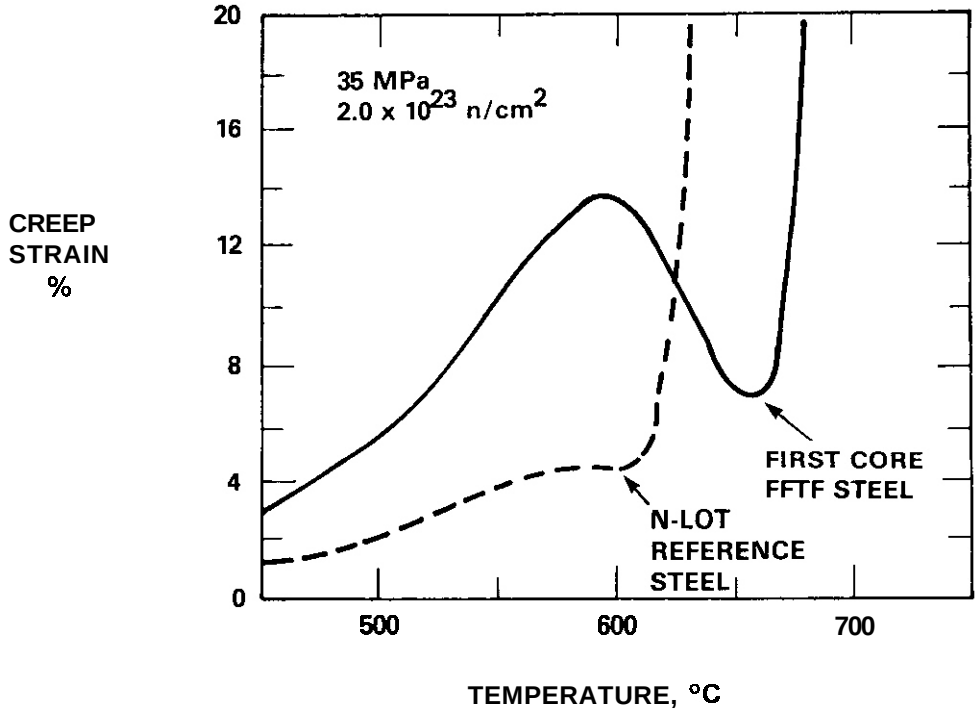

FIGURE 1. Predictions of creep correlations for two heats of steel of essentially identical composition irradiated in the EBR-II reactor.

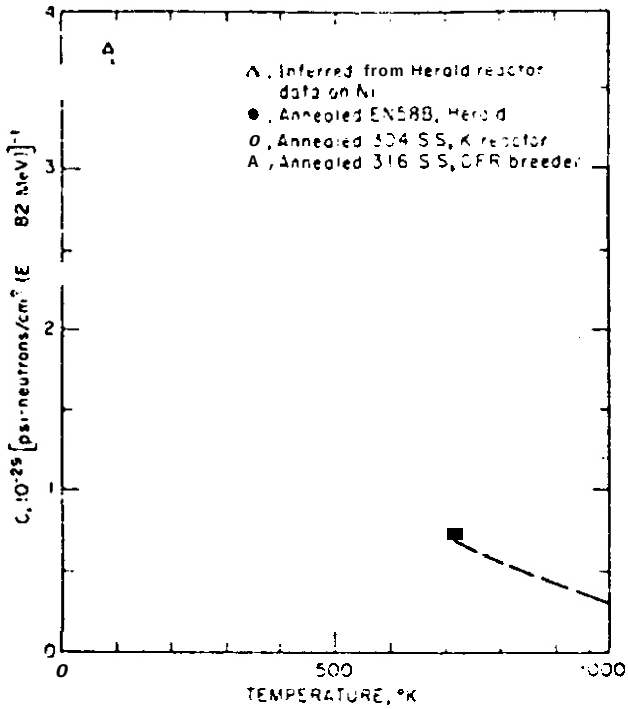

FIGURE 2. Temperature dependence reported by Gilbert[▼▼] of the coefficient describing the irradiation creep rate. This curve combines data from both thermal and fast reactor data for a variety of metals. The trend observed here has since been observed in other alloys and reactors however.

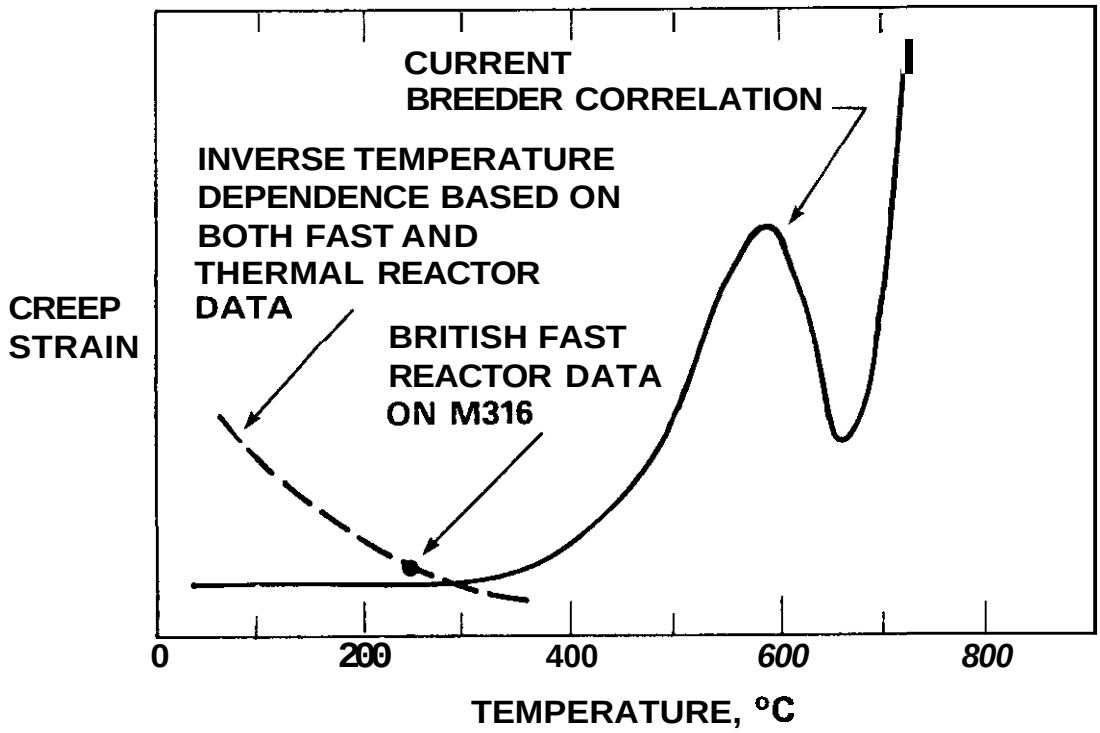

FIGURE 3. Schematic representation of procedure used to mate low temperature and high temperature correlations.

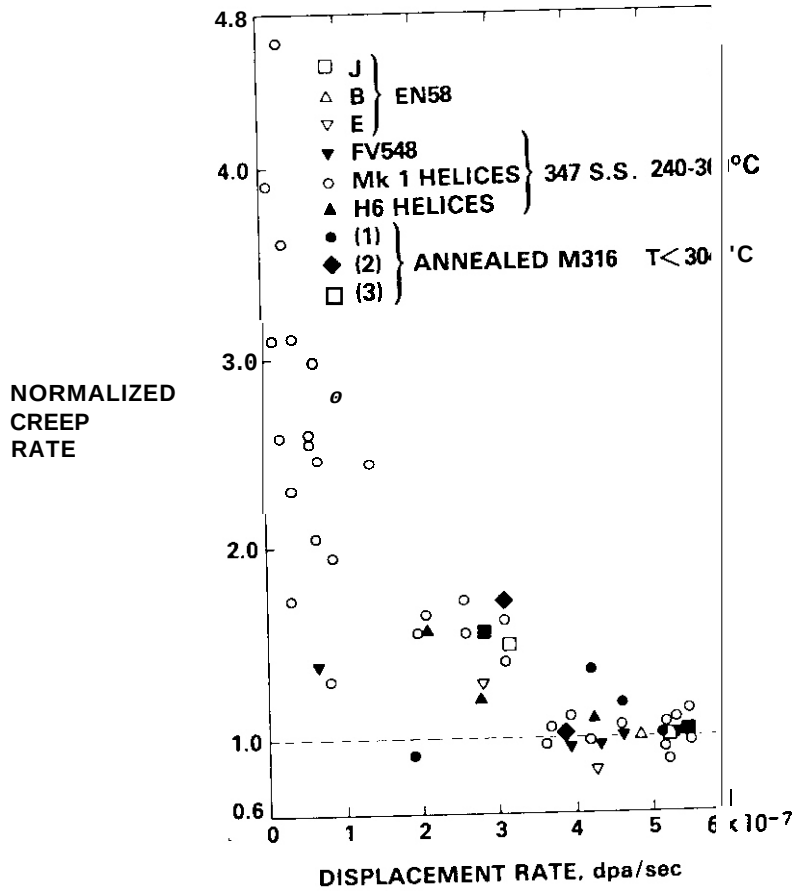

FIGURE 4. Dependence of irradiation creep on displacement rate observed in the Dounreay Fast Reactor by Lewthwaite and Mosedale.(6)

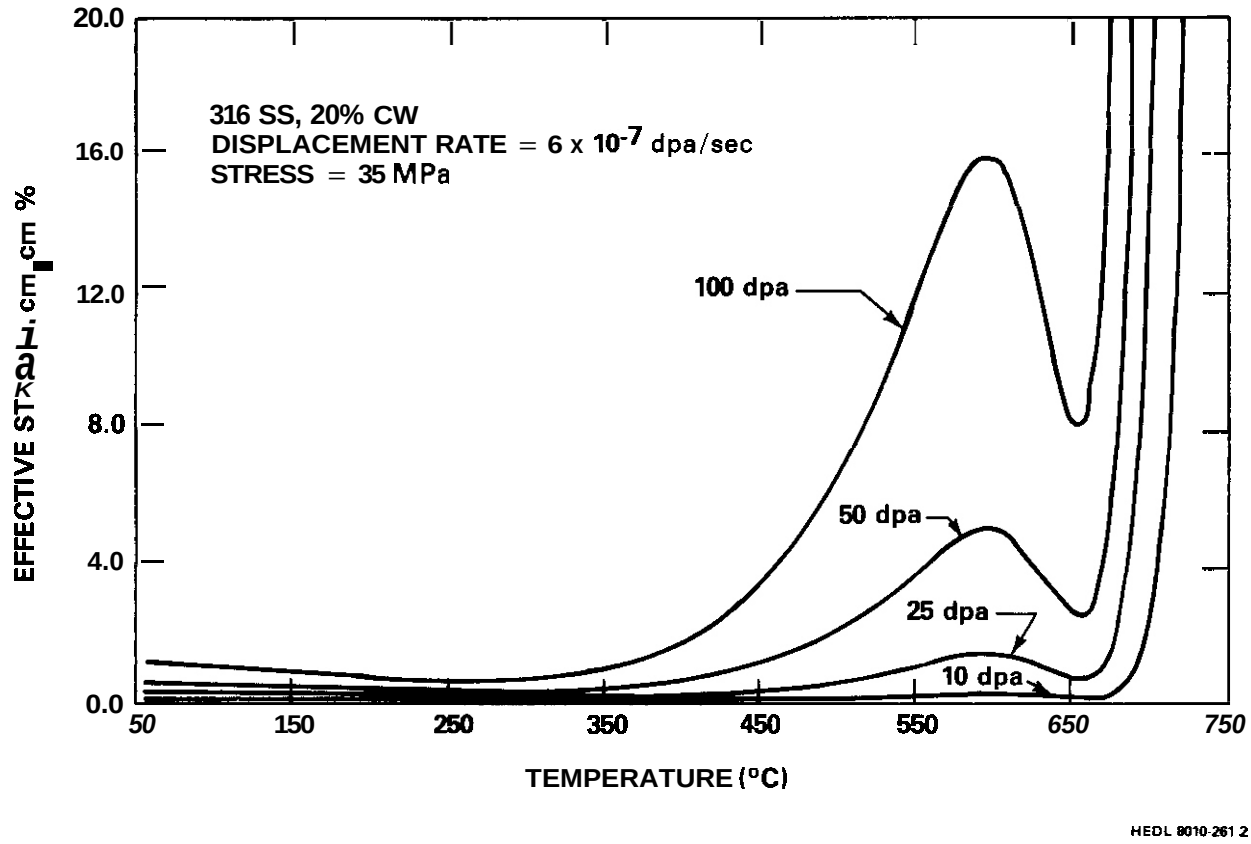

FIGURE 5. Predictions of creep correlation as a function of displacement level.

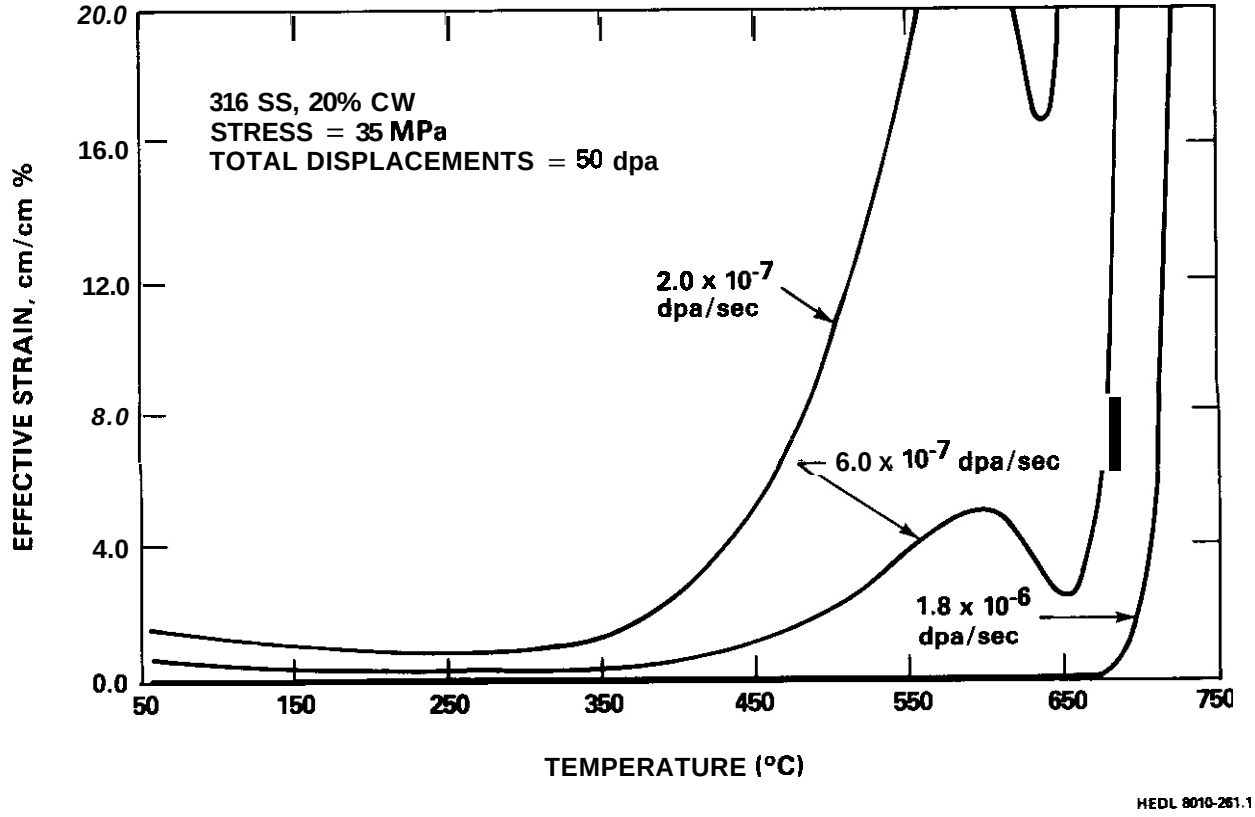

FIGURE 6. Predictions of creep correlation as a function of displacement rate.

DISTRIBUTION

uc-20 (117)

UC-20c (79)

DOE/RRT-HQ (7)
Mail Stop B-107
Washington, DC 20545

Asst Director, Materials Tech
NA Davies
JF Decker
PB Hemmig
KG Moses
RE Price
FT Scott

DOE/RL (3)
Richland, WA 99352

HA House
GM Chenevert
LA Pasquini

Argonne National Laboratory (4)
9700 South Cass Avenue
Argonne, IL 60439

LR Greenwood
A Taylor
APL Turner
H Wiedersich

Brookhaven National Laboratory
Associated Universities
Upton, NY 11973

Chairman, Nuclear Energy Dept

Columbia University
Plasma Physics Laboratory
New York, NY 10027

RA Gross

General Atomics Company (2)
P.O. Box 81608
San Diego, CA 92138

GR Hopkins
D Stevenson

Lawrence Livermore Laboratory (2)
University of California
P.O. Box 808
Livermore, CA 94550

MW Guinan
CM Logan

Los Alamos Scientific Laboratory (3)
University of California
P.O. Box 1663
Los Alamos, NM 87544

DJ Oudziak
CR Emigh
W Green

Massachusetts Institute of Technology (3)
Cambridge, MA 02139

L Lidsky
I- W Chen
NJ Grant

McDonnell-Douglas Astronautics
P.O. Box 516
St. Louis, MO 63166

D Kummer

Mound Laboratory
P.O. Box 32
Miamisburg, OH 45342

Manager, Tech Appl and Development

National Bureau of Standards
Gaithersburg, MD 20760

CD Bowman

Naval Research Laboratory (2)
Metallurgy Division, Code 6390
Washington, DC 20375

I Manning
JA Sprague

North Carolina State University
Department of Nuclear Engineering
Raieigh, NC 26707

JR Beeler, Jr.

Oak Ridge National Laboratory (7)
P.O. Box X
Oak Ridge, TN 37830

Director, Thermonuclear Div,
(Bldg 9201-2)
RJ Colchin, Bldg 9201-2
FG Perey
M Roberts, Bldg 9204-1
JO Stiegler
C Weisbin
FW Wiffen

Pacific Northwest Laboratory (4)
P.O. Box 999
Richland, WA 99352

JL Brimhall
T Chikalla
AB Johnson
LC Schmid

Princeton University (2)
Plasma Physics Laboratory
Forrestal" Campus
P.O. Box 451
Princeton, NJ 08540

C Osgood
K Wakefield

HEDL (36)

HR Brager	W/A-64	GD Johnson	W/A-65	FH Ruddy	W/A-4
WL Bunch	W/C-47	NE Kenny	W/C-115	FA Schmittroth	W/A-4
LL Carter	W/C-47	FM Mann	W/A-5	WF Sheely	W/C-62
DG Doran (2)	W/A-57	WN McElroy	W/C-39	RL Simons	W/A-57
EA Evans	W/JAD-6	RE Nygren	W/A-58	AL Trego	W/E-15
FA Garner	W/A-57	EK Opperman	W/A-58	GL Wire	W/A-58
DS Gelles	W/A-64	NF Panayotou	W/A-53	HH Yoshikawa	W/A-44
R Gold	W/C-39	EF Parker	W/E-17	Central Files (5)	WIC-110
HL Heinisch	W/A-57	RW Powell	W/A-64	Publ Services (2)	W/C-115
DL Johnson	W/A-4	RJ Puigh	W/A-58	Doc Management	W/C-115

Rockwell International Energy Systems
8900 DeSoto Avenue
Canoga Park, CA 91304

D Kramer

Sandia Laboratories (2)
Albuquerque, NM 87115

FL Vook (2)

Sandia Laboratories
Livermore, CA 94550

WD Wilson

University of Michigan
Nuclear Enaineerina Department
Ann Arbor,-MI 48165

T Kammash

University of Virginia
Charlottesville. VA 22901

WA Jesser

University of Wisconsin
1500 W. Johnson Drive
Madison, WI 53706

WG Wolfer

Westinghouse R&D Center (2)
Beulah Road
Pittsburgh, PA 15234

S Wood
JA Spitznagel

* GPO 796 - 855 1980